Title

Stable isotope fractionation and trace element partitioning in marine, terrestrial, and laboratory-synthesized carbonates

Author

Mitnick, Elizabeth Horner

Publication Date

2018

Stable isotope fractionation and trace element partitioning in marine, terrestrial, and laboratory-synthesized carbonates

by

Elizabeth H. Mitnick

A dissertation submitted in partial satisfaction of the
requirements for the degree of
Doctor of Philosophy
in
Earth and Planetary Science
in the
Graduate Division
of the
University of California, Berkeley

Committee in charge:

Professor Donald J. DePaolo, Chair
Professor Laura Lammers
Professor Michael Manga

Fall 2018

Stable isotope fractionation and trace element partitioning in marine, terrestrial, and laboratory-synthesized carbonates

by

Elizabeth H. Mitnick

Abstract

Stable isotope fractionation and trace element partitioning in marine, terrestrial, and laboratory-synthesized carbonates

By

Elizabeth H. Mitnick

Doctor of Philosophy in Earth and Planetary Science

University of California, Berkeley

Professor Donald J. DePaolo, Chair

This dissertation is about trace element and isotope fractionation in natural and laboratory-synthesized calcite and aragonite. Quantifying various isotope (δ^{13}C and δ^{44}Ca) and trace element (Sr/Ca and Mg/Ca) ratios in carbonates allows us to probe the kinetics of various reactions at the mineral-fluid interface. Understanding the way in which these signals depend on various parameters (e.g., precipitation rate, temperature, fluid composition) elucidates molecular-scale fundamentals of crystal growth. Similarly, this framework allows us to use these isotopic and trace element probes as proxies for interpreting natural carbonates, and in many cases, understand ancient environments. Furthermore, by identifying the nature of carbonate growth in solutions of varying chemistry and temperature, we can best harness the ability of these minerals to sequester CO_2 and fluid contaminants in response to anthropogenic pollution and climate change.

In Chapter 2, I use the Ca and Sr concentrations of marine sedimentary pore fluids to estimate rates of authigenic carbonate precipitation in modern sediments. Using the extensive Ocean Drilling Program database, these rates of authigenic carbonate production can be compared to coeval rates of organic carbon and biomineralized carbonate deposition, thereby quantifying relative fractions of each contributing carbon flux. While there are many sedimentary environments in which the relative authigenic carbonate fraction is significant in comparison to the organic and biomineralized fractions, the δ^{13}C of these carbonates is almost identical to the biomineralized fraction in nearly all cases. Within the context of a carbon isotope mass balance framework, I demonstrate that the biomineralized and authigenic carbonate fractions can be suitably accounted for via a single inorganic carbonate pool. This finding has implications for interpreting the geologic record, indicating that some of the fluctuations in δ^{13}C over the course of Earth history cannot be explained by the ongoing and extensive production of authigenic carbonate. I explore the few marine sedimentary environments that do produce authigenic carbonate with δ^{13}C distinct from that of the biomineralized fraction, and thereby could be possible exceptions to the main finding of this work. The processes

responsible for creating this isotopically anomalous authigenic carbonate are not thought to be steady-state phenomena throughout most of Earth history. The production of authigenic carbonate in these environments therefore suggests that $\delta^{13}C$ variations in the sedimentary record could not have been the *result* of authigenic carbonate formation. Rather, the formation of authigenic carbonate with a $\delta^{13}C$ composition distinct from that of biomineralized carbonate would be a consequence of a non-steady state perturbation to the carbon cycle. Consequently, these exceptional environments do not change the finding that a single inorganic carbon reservoir can be used to encapsulate the ongoing biomineralized and authigenic fluxes in marine sediments from an isotopic mass balance standpoint.

In Chapter 3, I study the formation of calcite and aragonite from the travertine-precipitating hot springs of Bridgeport, California. These travertines form as an elongate fissure ridge of intergrown calcite and aragonite, precipitating along the edges of a thin fluid conduit with systematically changing fluid pH, temperature, and CO_2 degassing. The ability to readily measure modern precipitates from predictably evolving ambient fluids makes this system a unique natural laboratory in which to probe kinetics of carbonate growth in a high-temperature (>60°C) system. While travertines around the world have been the subject of a substantial body of literature, only one other study has reported the Ca isotope fractionation that occurs between travertine carbonates and fluid. In this work, $\delta^{13}C$, $\delta^{44}Ca$, Sr/Ca and Mg/Ca ratios in bulk carbonates and fluids are measured. Although the Sr/Ca ratios in the bulk solid are much higher than expected based on experimental studies, I argue that they may not be anomalous for thermogene travertines. The spatially evolving $\delta^{13}C$ and Sr/Ca composition of the fluid and solid indicates decreasing aragonite content down-conduit, suggesting that the Ca isotope fractionation will reflect the relative change in calcite and aragonite fractions. Although aragonite is expected to produce a larger magnitude fractionation than calcite, we do not observe any trend with distance from the inlet corresponding to the systematically changing mineral fractions. This observation can be explained by ongoing recrystallization of carbonate in the porous conduit walls, demonstrating the complex nature of multi-mineral travertine deposits and the impact of diagenetic alteration on Ca isotope systems in nature.

Finally, in Chapter 4, I probe calcite growth at the smallest spatial and temporal scales studied in this dissertation. I present results from an experimental study in which calcite was precipitated from solutions of varying Mg/Ca ratios with a constant saturation index (SI) under controlled conditions. The aim of this project was to determine the effect of Mg on calcite growth as reflected in the Ca isotope fractionation between solid and solution. Mg is thought to primarily inhibit calcite precipitation via a kink blocking mechanism. However, the change in Ca isotope fractionation with increasing Mg/Ca and decreasing precipitation rate at constant SI demonstrates that in addition to kink blocking, Mg also impedes growth via incorporation inhibition. This additional mechanism alters the relative Ca attachment and detachment fluxes at the crystal surface, resulting in the observed fractionation. This finding has important implications for the interpretation of Ca isotope fractionation in both marine inorganic and biomineralized calcite precipitating from Mg-bearing seawater and sedimentary pore fluids.

Courage does not always roar –
Sometimes courage is the small voice at the end of the day that says,
“I will try again tomorrow.”

Mary Anne Radmacher

Contents

3 Ca isotope and trace metal incorporation in intergrown calcite and aragonite: insights from a thermogene travertine deposit.............................32

4 Probing effects of Mg on Ca isotope fractionation in calcite: results from seeded growth experiments in a chemostat reactor...74

Acknowledgements

I am very thankful to my advisor, Don DePaolo, who generously supported my work over the past years, who challenged me, and helped guide my growth as a scientist. I am also very thankful for Don's patience during times when I struggled personally, and for the freedom he gave me in my research. Early on in the program, I was a driver for one of Don's introductory geology field trips in Arizona. One day we hiked up a gigantic cinder cone, and as I climbed one foot up only to slide two back down, I remember looking at Don gracefully summit. I told myself that I would not fail to climb this horrible slope made of unconsolidated, scratchy cinders, especially in front of my new advisor. I also convinced myself that if I could get to the top, I could get my PhD with Don. I was not wrong. Climbing a cinder cone from hell is not a bad metaphor for getting a PhD in Earth Science. The trip up is gnarly, but the view and satisfaction of making it to the summit is certainly worth it.

I am incredibly thankful to Laura Lammers, who kindly welcomed me into her research group and who served as my unofficial advisor. Laura, you are a gem of a person as well as scientist. I am grateful for how much you taught me about geochemistry as well as your overall support during my time here. And, to the whole Lammers group, thank you for including me in your cohort, and for being such supportive labmates. In particular, I want to express thanks to Holly Barnhart, whose skilled assistance and positive attitude was absolutely key to my success. It has been wonderful to both mentor and learn from you, and I am thrilled you have found your passion in geochemistry.

I also want to express thanks to Michael Manga, who served on both my qualifying exam and dissertation committees. I had the pleasure of attending Michael's group meetings as well as serving as a graduate student instructor while he taught EPS 50. Michael's commitment to science and science education at all levels is admirable. I also appreciate his frank communication and humor.

I cannot thank Shaun Brown enough. Shaun trained me and taught me everything I know about isotope sample preparation and TIMS. Shaun, thank you for your accessibility, patience, help whenever it was needed, for venting in the lab, for being a sounding board, and for sharing your unfiltered opinion.

To my mom and dad, Denise and Stephen Mitnick – it feels wildly insufficient to thank you in just a few words. I hope you know that the life you supported me in building is as beautiful as I could have ever dreamed it, and I owe every accomplishment, including this one, to you both. Thank you for believing in me and loving me so fiercely through everything. To my sister, Emily – thank you for being a supportive friend and

kind listener, and for always having my back. I couldn't be happier that you and Mike and I are neighbors by the Bay, and even more so that we are friends.

To my grandparents, Nanny and Poppy, Bubbe and Earl, and Pop-Pop and Maxine – your collective values in family, education, and exploration are what allowed me to follow my love of science all the way here. Thank you for cheering me on emphatically and lovingly. I am blessed to be a member of this crazy tribe.

To the rest of my family, and the friends who have become my family – thank you for your endless love, encouragement, phone calls, letters, visits, and hugs. Thank you for your patience as I learned how to explain what I do to the layperson, and for reminding me that there is a whole world outside of academia that does not care about carbonates. Some days, I am especially grateful for that.

To Ryan Bear – thank you for believing in me, reminding me of my strength, and for unwaveringly showing your support and love in tangible and meaningful ways. You are a tremendous partner. I still cannot believe you came to Oakland to meet a woman with two cats and no real income, but I'm so glad every day that you did.

Alex Bryk – you got me through my very own hell and I am forever grateful. Thank you for your hugs and for teaching me how much there is in the world to laugh at. I am also so thankful for the rest of my cohorts in EPS (past and present) and friends not previously mentioned, including Chelsea Willett, Tom Smart, Kristen Fauria, Hannah Bourne, Nick Knezek, Josh Tollefson, Daniella Rempe, and many others. Nobody understands like you do. Thank you for the hugs, smiles, coffees, beers, and laughs that helped propel me to the finish line.

I want to express gratitude for my fluffs, B and P, whose playfulness, purrs, and fuzziness have provided me laughter and comfort when I really needed it. I also want to acknowledge the profoundly positive influence of my Cyclebar family on my general existence. I would look and feel dramatically different without you.

Finally, I am tremendously grateful to Dr. Kaila Compton and Dr. Ariel Trost, who helped me through my worst times, taught me to hone my anxiety management skills, and whose kindness inspired me to love myself regardless of externalities.

I learned far more over the past few years than what is reflected here. I am endlessly grateful for those mentioned (and those I may have missed) who, in both big and in small ways, have helped me get to today. It has been a very long journey, and I am quite glad I did it. I am also thrilled I do not have to do it a second time. It takes perseverance, passion, a lot of love, and as is now apparent, a village. To my entire village, thank you.

Chapter 1

Introduction

1.1 Why carbonates?

Carbonate minerals are of interest from a fundamental science standpoint, for those interested in the geologic past, as well as within more applied contexts such as engineering and climate science. Carbonates are an integral part of the global carbon cycle, responsible for regulating climate over geologic timescales. As concern over anthropogenic climate change grows, understanding how carbonate reservoirs will evolve in response to a warming and changing globe becomes increasingly important. Carbonates are also receiving increased attention from scientists and engineers, who are developing methods to accelerate natural carbon sequestration with carbonate minerals via the injection of supercritical carbon dioxide, CO_2, into subsurface sandstone reservoirs.

In addition to their role in the geologic carbon cycle and relationship to climate, carbonates are of particular interest in the geosciences because they are ubiquitous in nature, both in the modern era and throughout much of the geologic record. The isotope and trace element compositions of carbonate minerals are dictated by rates of precipitation and dissolution, as well as specifics of the ambient growth environment, such as fluid chemistry (bulk and isotopic) or temperature. Consequently, scientists have been able to use a plethora of isotopic and trace elemental proxies measured in carbonate minerals to understand phenomena spanning incredible spatiotemporal scales, ranging from the geochemical evolution of Earth's atmosphere and oceans over geologic time, to the nature of ion attachment and detachment on the surface of a growing calcite crystal.

With trace element and isotope proxies such as $\delta^{13}C$, $\delta^{18}O$, $^{87}Sr/^{86}Sr$, Mg/Ca, and $\delta^{44}Ca$, researchers use carbonate minerals to identify large-scale geologic processes including glaciation, mass extinction, global oxygenation, supercontinent formation/breakup, ocean paleotemperatures, rates of continental weathering and associated global element fluxes. On the other end of the spatiotemporal spectrum, scientists are devoted to understanding carbonate growth at the molecular scale, using isotope and trace metal incorporation to illuminate what dictates ion attachment and detachment at the crystal surface. Understanding processes of this nature, especially kinetic controls on precipitation and dissolution, is vital for accurate models of geologic carbon sequestration, remediation of soils and sediments, and global element cycles. In addition to its broader applications, understanding controls on carbonate formation at the molecular scale also can yield fruitful insights into the fundamental nature of di-ionic crystal growth.

1.2 Probing nanoscale controls on carbonate formation

From a basic science standpoint, calcite is an ideal mineral to use in studying fundamental molecular and nanoscale interactions during crystal nucleation and growth because of its di-ionic or 'AB' composition, its simple structure, and the feasibility of growing it on reasonable timescales. The abundance of various trace elements (e.g., Mg/Ca, Sr/Ca, etc.) and different isotopic ratios (e.g., δ^{44}Ca, ^{87}Sr/^{86}Sr, δ^{13}C, δ^{18}O, δ^{26}Mg, etc.) can be measured in calcite to elucidate aspects of calcite growth that are otherwise difficult to observe. These trace and isotopic systems, used alone and in combination with one another, can be used to determine growth conditions such as precipitation rate, ambient fluid chemistry, pH, or temperature, as well as to probe the behavior of various molecules at the crystal-fluid interface.

Laboratory and natural systems have been utilized extensively to probe various aspects of both biomineralized and inorganic carbonate growth. Experimental studies starting in the early 2000's (e.g., LeMarchand et al., 2004; Tang et al., 2008; Tang et al., 2012) focused on precipitating inorganic calcite and aragonite under controlled conditions, then measuring the mass-dependent Ca isotope fractionation between precipitated solids and the surrounding fluids. The differential partitioning of heavy and light isotopes of Ca between fluid and solid phases, denoted $\Delta^{44/40}$Ca, reflects the dynamics of various interacting aqueous species at and near the crystal surface, and consequently the process and rates of crystal growth. Thus, studies of stable isotope fractionation during growth can serve as molecular "probes" that inform our basic understanding of crystal growth.

With experimental and modeling studies we can advance our mechanistic understanding of interfacial processes and growth dynamics. This deeper understanding allows for predictive models that can then be applied at larger scales (i.e., field scale or larger) and expanded to other materials and minerals in order to more effectively remediate contaminated systems, sequester CO_2 in carbonate minerals to combat anthropogenic climate warming, and interpret the geologic record.

1.3 Carbonates in proxy work and marine diagenesis

In marine settings, there are three dominant types of carbonates: calcite and aragonite, two polymorphs of $CaCO_3$, and dolomite, $CaMg(CO_3)_2$. Since the proliferation of calcifying organisms, the vast majority of marine calcite and aragonite has been biogenic in origin. Yet, most of the carbonate found in marine sediments has been altered in some way by various physical and biogeochemical reactions that occur in these reactive, porous, high surface area settings. Consequently, sediments just a few meters below the seafloor are often markedly different than the original deposit, having undergone a multitude of diagenetic reactions over hundreds of thousands to millions of years. Carbonate that is initially deposited from the water column can dissolve partially or fully, followed by re-precipitation in a process termed "recrystallization". Additionally, carbonate can precipitate *in situ* from pore fluids that are supersaturated with respect to a given carbonate phase. In this way, making a distinction between what is biogenic carbonate and what is abiogenic becomes complicated – yet often necessary.

A great deal of work in the geosciences has relied on the ability of calcifying organisms in the water column to truthfully preserve characteristics of the surrounding marine environment, be it temperature, pH, geochemical or isotopic composition of the ambient waters. However, the utility and accuracy of the many proxies developed are dependent on (arguably) two variables. One variable is the extent to which we can understand and account for organism vital effects, or the way in which an organism's unique biology can influence the nature of specific chemical reactions. The second variable is the extent to which the original material has been diagenetically altered between the time the organism captured the geochemical signal in the water column and the time it is measured. Most sediments are not only composed of carbonate minerals, but can host a variety of other mineral phases as well as organic material, dissolved gases, volcanic ash and glass, gas hydrates, mesofauna, macrofauna, and microbial communities with site-specific metabolisms. The complexity of the diagenetic history of a given carbonate sediment sample can generally not be overstated.

1.4 Summary

For robust interpretation of geochemical signals recorded in carbonates, as well as to predict rates of formation for purposes such as geologic CO_2 sequestration, it is essential to understand relationships between growth rates, ambient conditions, and bulk and isotopic composition of the precipitate. If we can better understand the diagenetic reactions that occur in marine sediments in conjunction with a more advanced understanding of the nanoscale controls on carbonate formation, it is possible to use carbonates to understand Earth's past and even, perhaps, engineer a better Earth for the future.

In the following chapters, I use the isotopic ($\delta^{13}C$ and $\delta^{44/40}Ca$) and trace element (Mg/Ca and Sr/Ca) composition of natural and synthetic materials to understand controls on what is commonly referred to as "inorganic" carbonate formation in marine, terrestrial, and laboratory settings. The systems studied here range from laboratory-scale to global, and may appear to be quite disparate. However, carbonates in million-year-old marine sediments across the globe are products of the same fundamental reactions that occur on the laboratory benchtop and on molecular scales. Studying carbonates on both ends of the spatiotemporal spectrum can be an informative means of teasing apart primary and diagenetic compositional signatures in natural samples, as well as motivating specific experimental studies.

Chapter 2, *Authigenic carbonate formation rates in marine sediments and implications for the* $\delta^{13}C$ *record,* addresses authigenic carbonate in marine sediments: controls on its formation, and its trace element and isotopic composition. In this chapter, I estimate rates of authigenic carbonate formation in marine sediments using Ca and Sr concentrations in sedimentary pore fluids as well as carbon isotopes in carbonate and pore fluids to understand the role of diagenetic carbonate in the global carbon cycle with implications for interpreting the marine $\delta^{13}C$ record.

Chapter 3, *Ca isotope and trace metal incorporation in intergrown calcite and aragonite: insights from a thermogene travertine deposit*, presents results from a trace element and isotopic study of intergrown calcite and aragonite from an active travertine fissure ridge from the eastern Sierra Nevada. In this work, Ca isotope fractionation and estimates of Sr partition coefficients between solids and fluids allow us to propose controls on precipitation rate as well as speak to the role of post-depositional reactions in controlling the composition of semi-porous thermogene travertine deposits.

Chapter 4, *Probing effects of Mg on Ca isotope fractionation in calcite: results from seeded growth experiments in a chemostat reactor*, reports findings from an experimental study in which calcite was grown (seeded) in a chemostat reactor at constant saturation index (SI) under varying Mg/Ca fluid ratios. Here we use Ca isotope measurements within the context of previously established surface kinetic models to demonstrate the effect of Mg on the relative rates of Ca attachment and detachment at the calcite surface, with implications for understanding the mechanism(s) of growth inhibition by Mg.

Chapter 2

Authigenic carbonate formation rates in marine sediments and implications for the $\delta^{13}C$ record

This chapter was previously published in Mitnick, E.H., Lammers, L.N., Zhang, S., Zaretskiy, Y., and DePaolo, D.J., *Earth and Planetary Science Letters* **495**, 135-145 (2018). doi:10.1016/j.epsl.2018.05.018

Abstract

Carbon isotope ($\delta^{13}C$) variations measured in carbonates have been attributed to large-scale phenomena throughout Earth history, such as changes in atmospheric oxygen or global glaciations. These interpretations follow from a model wherein the $\delta^{13}C$ of marine dissolved inorganic carbon (DIC) is controlled by the relative sedimentary burial rates of biogenic carbonate (BC) and organic carbon (OC). A new model proposes authigenic carbonate (AC) as a third major sedimentary C pool, implying that $\delta^{13}C$ anomalies are not necessarily indicative of extreme changes in the global carbon cycle and/or atmospheric oxygen. Two conditions are required for AC formation to significantly alter bulk carbonate $\delta^{13}C$: the AC isotopic composition must be at least ~3‰ different from that of BC and the AC/BC ratio must be >0.1. We use pore fluid Ca and Sr concentrations to estimate rates of AC formation in Late Cenozoic marine sediments, then calculate relative fractions of AC, OC, and BC. Today AC is not expected to constitute a significant fraction of total sedimentary carbon (AC+OC+BC) globally; however, there are modern sites where local conditions promote elevated AC/BC and anaerobic metabolisms can alter the $\delta^{13}C$ of pore fluids. We investigate these sites to determine what conditions might enable AC to alter $\delta^{13}C$ of marine DIC. We find there is very little net addition of AC relative to BC, but large quantities of AC form today across many settings via recrystallization. In settings where remineralization of organic matter causes recrystallized carbonate to form with modified $\delta^{13}C$, AC/BC is generally too low for this recrystallization to significantly shift the $\delta^{13}C$ of the bulk carbonate. However, exceptions are found in sites with very low BC and extensive methane oxidation, suggesting that this environment type would need to be globally extensive in the past in order for AC formation to change the $\delta^{13}C$ of marine DIC.

1. Introduction

1.1 Overview

A longstanding problem in the study of paleoclimate lies in explaining carbon isotope ($\delta^{13}C$) variation in the geologic record, thought to reflect changes in the $\delta^{13}C$ of marine dissolved inorganic carbon (M-DIC) through Earth history (Fig 1). In this record, there are both long-term (>10^7 yr) and transient variations (± 3‰ or larger) that persist for periods extending beyond the 0.1 My residence time of M-DIC (e.g., Halverson et al., 2005; Kump and Arthur, 1999; Payne et al., 2004; Saltzman 2005; Saltzman and Thomas, 2012; Sephton et al., 2002; Shields and Veizer, 2002). The traditional interpretation of the $\delta^{13}C_{M\text{-}DIC}$ record is based on a steady-state mass balance between carbon inputs ($\delta^{13}C_{in}$) to the M-DIC reservoir and the relative sedimentary burial rates of carbonate carbon and organic carbon (e.g., Arthur et al., 1988; Canfield and Kump, 2013), written as:

$$\delta^{13}C_{in} = \delta^{13}C_{out} = (1 - f_{org})\delta^{13}C_{carb} + f_{org}\delta^{13}C_{org} \qquad [1]$$

where *f* represents the fraction of total sedimentary carbon that is either carbonate (*carb*) or organic carbon (*org*). Organic carbon has a much lower $\delta^{13}C$ relative to that of M-DIC due to fractionation during photosynthesis and other carbon fixation pathways. The $\delta^{13}C_{M\text{-}DIC}$ is assumed to be roughly equal to $\delta^{13}C_{carb}$, as there is only a small fractionation between M-DIC and carbonate. There are spatial variations in $\delta^{13}C_{M\text{-}DIC}$ (up to ~3‰) due to temperature-dependent circulation effects as well as biological productivity, fluxes of organic matter to the deep ocean, and remineralization rates (e.g., Raven and Falkowski, 1999), although deep water values average 0‰, with modern mean $\delta^{13}C_{M\text{-}DIC}$ equal to 0±1 (Saltzman and Thomas, 2012).

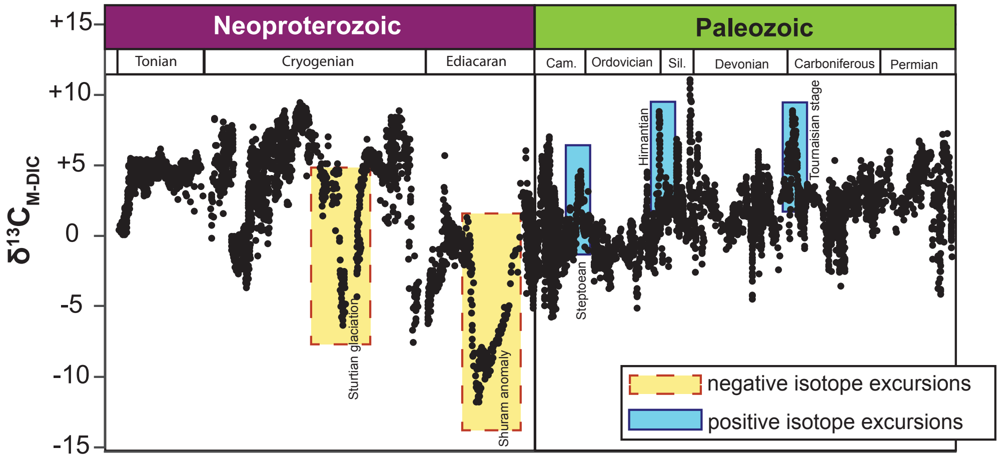

Figure 1. Neoproterozoic and Paleozoic marine carbon isotope record. Some examples of isotope excursions highlighted in yellow with dashed line (negative excursions) and blue

with solid line (positive excursions). Data from Halverson et al., 2010 and Saltzman and Thomas, 2012.

1.2 Use of the δ^{13}C record as a paleoproxy for oxygenation state

The δ^{13}C record has been used in the context of equation 1 as a proxy for atmospheric oxygen production and removal due to burial or consumption of organic carbon. This proxy is based on the relationship between organic carbon and oxygen during aerobic respiration (Eq. 2; Berner and Canfield 1989; Berner and Maasch 1996) according to the reaction,

$$CH_2O + O_2(g) \leftrightarrow CO_2(g) + H_2O \qquad [2]$$

Following this relationship, if f_{org}, the organic carbon burial fraction, increases for an extended period of time, atmospheric oxygen is expected to build up. Similarly, atmospheric oxygen levels should decrease if the organic carbon burial rate decreases for an extended period of time (e.g., Berner and Petsch 1998).

There exists a substantial body of work that attempts to constrain atmospheric oxygen levels in the past, based on evidence including distribution of redox-sensitive elements such as molybdenum, uranium, and iron, as well as sulfur isotopes and phylogenetic clues (Berner and Canfield, 1989; Canfield and Teske, 1996; Farquar et al., 2001; Lowenstein et al., 2014 and references therein). However, there are places in the record, some of which are summarized by Schrag et al. (2013), where the O_2-interpretation of the δ^{13}C signal is at odds with other proxies and observations, lacks independent evidence, or implies much larger changes than are likely. Consequently, other explanations for patterns in δ^{13}C have been proposed.

An altered oxygenation state of the Earth's atmosphere and oceans is not the only interpretation of the $\delta^{13}C_{M\text{-}DIC}$ record, although many proposed interpretations are at least indirectly tied to an altered global redox environment. There are large magnitude excursions associated with glaciations (e.g., Marshall et al., 1997), mass extinctions (e.g., Sephton et al., 2002), ocean anoxic events (e.g., Arthur et al., 1988), consequences of emplacement of large igneous provinces (e.g., Retallack and Jahren, 2008), as well as inferred events such as the catastrophic release of methane clathrates (e.g., Dickens et al., 1995). However, there are isotope excursions in the record, such as those identified by Schrag et al. (2013), that do not have other geochemical or stratigraphic indicators of global change, specifically changes in oxygenation state, and these excursions therefore cannot be interpreted with any degree of confidence.

1.3 Considering authigenic carbonate in the carbon isotope mass balance

Motivated by inconsistencies between the δ^{13}C record and evidence from other proxy records, alternative models have been proposed that would serve to decouple atmospheric O_2 from seawater δ^{13}C. One of these models posits that carbonate formed within marine sediments, called authigenic carbonate (AC), could take on values of δ^{13}C and form at high enough rates relative to the organic C and biogenic carbonate burial fluxes, such that $\delta^{13}C_{M\text{-}DIC}$ could shift without requiring a large change in atmospheric oxygen (Schrag et al., 2013). This mechanism could then cause variations in $\delta^{13}C_{M\text{-}DIC}$ that are no longer directly tied to the CO_2-O_2 balance. In the marine environment, AC forms within sediments, either by (a) "recrystallization", which is dissolution of biogenic carbonates ("BC"; i.e., detrital tests of forminifers or coccoliths) followed by reprecipitation as nonbiogenic carbonate, or (b) net precipitation from pore fluids due to an increase in carbonate alkalinity caused by microbial respiration of organic carbon or methane (Morse et al., 2007), or alternatively due to deepening of the carbonate compensation depth (CCD) to well below the sediment-water interface.

The steady-state $\delta^{13}C$ mass balance described by Eq. 1 has been rewritten by Schrag et al. (2013) to include AC in addition to the original sedimentary C sinks, biogenic carbonate (BC) and organic carbon (OC):

$$\delta^{13}C_{in} = f_{BC}\,(\delta^{13}C_{M-DIC} + \varepsilon_{BC}) + f_{AC}\,(\delta^{13}C_{M-DIC} + \varepsilon_{AC}) + f_{OC}\,(\delta^{13}C_{M-DIC} + \varepsilon_{OC}) \quad [3]$$

$$\delta^{13}C_{M-DIC} = \delta^{13}C_{in} - f_{BC}\,\varepsilon_{BC} - f_{AC}\,\varepsilon_{AC} - f_{OC}\,\varepsilon_{OC} \quad [4]$$

where ε indicates the fractionation factor between M-DIC and the sedimentary carbon pool (e.g., if ε_{OC} = -25, $\delta^{13}C_{OC} = \delta^{13}C_{M\text{-}DIC}$ -25). According to these formulae, two conditions must be met for AC to be important to the overall isotopic mass balance and to cause changes to $\delta^{13}C_{M\text{-}DIC}$. First, f_{AC} must be similar in magnitude to f_{BC} and f_{OC}. Second, ε_{AC} must be different from ε_{BC}, or Eq. 3 reduces to Eq. 1. As written in Eq. 4, the value of $\delta^{13}C_{M\text{-}DIC}$ depends on the sedimentary fractions and fractionation factors for AC, OC, and BC, as well as the isotopic inputs to the M-DIC pool.

For the AC term to be significant in equation 4, not only must f_{AC} be sufficiently large, but the AC isotopic composition must also be significantly different from that of BC. Herein we define AC that is isotopically different from BC ≥ |3‰| as AC*, and f_{AC^*} is the corresponding sedimentary carbon fraction. Where the isotopic composition of AC does not deviate from that of BC, or in cases where authigenic carbonate is discussed independently of its isotopic composition, 'AC' is used.

The long-term average value of f_{OC} is estimated as ~0.2 (Schidlowski et al., 1975; Derry, 2014), and this value is associated with a relatively stable amount of atmospheric O_2 during the Phanerozoic. If we want to determine how great an effect AC could have while maintaining our modern atmospheric oxygen level, we set the constraint of f_{OC} = 0.2, which results in:

$$\delta^{13}C_{M-DIC} = -\,f_{AC}\,\varepsilon_{AC} \quad [5]$$

Steady state conditions of f_{AC} = 0 and f_{OC} = 0.2 result in our modern $\delta^{13}C_{M\text{-}DIC}$ value of ~0 (following Eq. 4). If we assume that f_{OC} scales with production/removal of O_2, then to evaluate what is required to have $\delta^{13}C_{M\text{-}DIC}$ vary without changing pO_2, we hold f_{OC} constant in equation 4. To generate $|\delta^{13}C_{M\text{-}DIC}| > 3$ due to AC formation without changing the burial fraction of OC (and consequently, atmospheric O_2), the fractions of BC and AC must sum to 0.8, with less AC required when ε_{AC} is large, and more AC required when ε_{AC} is small.

1.4 Aims and approach of present study

There has been increasing interest over the past years to understand the role and nature of authigenic carbonate in both modern and ancient sediments (Canfield and Kump 2013; Schrag et al., 2013; Sun and Turchyn 2014). However, sedimentary carbon fluxes from AC precipitation have not been evaluated in the context of coeval biogenic carbonate and organic carbon fluxes, nor have the AC fluxes been considered in an isotopic context. This contextual assessment of authigenic carbonate is crucial if we are to understand how the burial dynamics of marine carbonate play into the carbon cycle and affect the steady-state isotopic composition of the ocean. Schrag et al. (2013) and numerous other studies also raise the question of whether or not the $\delta^{13}C$ record is recording global versus local marine signals, and we explore this in our discussion as well.

In this study, we quantify modern-day carbon isotope fluxes due to AC formation in a variety of different marine sedimentary environments. Although globally, it is not expected that AC is a significant fraction of total sedimentary carbon today, there are a wide variety of sedimentary environments represented by cores collected through the International Ocean Discovery Program (IODP), including sites known or thought to have considerable AC production locally. Sites with significant f_{AC}* might provide insight into global sedimentary conditions that could have shifted $\delta^{13}C_{M\text{-}DIC}$ in the past. We then estimate the range of isotopic values of AC based on known mechanisms supported by pore fluid profiles of $\delta^{13}C_{PF\text{-}DIC}$ and $\delta^{13}C$ of bulk carbonates. We discuss possible controls on authigenic carbonate formation in marine sediments and implications of our results for understanding the role of authigenic carbonate in the $\delta^{13}C$ record, and interpreting $\delta^{13}C$ as a record of global phenomena.

2. Methods

2.1 Overview

Reactions within marine sediments are reflected in pore fluid concentrations of $\mathrm{Ca^{2+}, Mg^{2+}, Sr^{2+}, HCO_3^-, SO_4^{2-}}$ as well as pH and other variables. Our objective is to use pore fluid chemistry to estimate rates of authigenic carbonate formation. This is accomplished using depth-variant pore fluid Ca and Sr concentrations within a one-dimensional diffusion-advection-reaction model. The marine sediment cores in our study were selected from the International Ocean Discovery Program as well as sites from preceding ocean drilling initiatives (Deep Sea Drilling Project (1966-1983), Ocean Drilling Program (1983-2003), and Integrated Ocean Drilling Program (2003-2013), summarized in Table 1. Site data is sourced from the online repository (link in Supplemental Material) as well as from individual site reports (see Supplemental Material for references by site). This approach is useful to determine how AC formation rate varies with sedimentation conditions, and will allow us to learn about what conditions could represent times in Earth history with globally high AC production. The limitation on the number of sites (N = 37) is due to data availability and the fineness of the spatial resolution of measurements.

DSDP/ ODP/ IODP Leg		**Water Depth (m)**	**Expedition**	**Description**
42	381	1728	Black Sea	anoxic bottom waters
96	618	2412	Orca Basin	anoxic bottom waters
112	681	150.5	Peru Continental Margin	continental shelf
112	688	3827	Peru Continental Margin	continental margin
113	693	2359	Weddell Sea, Antarctica	continental margin
117	725	311.5	Oman Margin	oxygen minimum zone
130	803	3410	Ontong Java Plateau	deep-sea
130	805	3189	Ontong Java Plateau	deep-sea
130	806	2520	Ontong Java Plateau	deep-sea
130	807	2804	Ontong Java Plateau	deep-sea
133	819	565	Northeast Australian Margin	continental slope
139	855	2445	Middle Valley, Juan de Fuca Ridge	deep-sea
141	860	2148	Chile Triple Junction	continental margin
141	863	2564	Chile Triple Junction	continental margin
146	892	675	Cascadia Margin	continental margin
157	950	5437	Gran Canaria and Madeira Abyssal Plain	deep-sea
157	951	5437	Gran Canaria and Madeira Abyssal Plain	deep-sea
162	984	1649	North Atlantic-Arctic Gateways II	deep-sea
165	998	3180	Caribbean Ocean History	continental margin
165	999	2828	Caribbean Ocean History	continental margin
166	1003	481.4	Bahamas Transect	carbonate platform
169S	1033	203	Saanich Inlet	anoxic fjord
169S	1034	226	Saanich Inlet	anoxic fjord
175	1082	1279	Benguela Current	upwelling zone
175	1084	1992	Benguela Current	upwelling zone
177	1088	2082	Southern Ocean Paleoceanorgraphy	deep-sea
177	1092	1974	Southern Ocean Paleoceanorgraphy	deep-sea
181	1119	393	Southwest Pacific Gateways	continental slope
181	1120	543	Southwest Pacific Gateways	continental margin
189	1169	3568	Tasmanian Gateway	deep-sea
194	1194	368	Marion Plateau, Northeast Australia	carbonate platform

202	1232	4072	Southeast Pacific Paleoceanographic Transects	continental margin
202	1234	1015	Southeast Pacific Paleoceanographic Transects	continental slope
204	1245	870	Cascadia Continental Margin	continental margin
313	M0027	32	New Jersey Shallow Shelf	continental shelf
347	M0059	37	Baltic Sea Basin	shallow basin
308	U1319	1430	Brazos-Trinity Basin IV (Gulf of Mexico)	continental slope

Table 1. Summary of sites included in this study.

2.2 Modeling approach

2.2.1 Site categorization and estimation of absolute AC formation rates

The term "authigenic" means "formed in place" and hence strictly speaking, refers to any carbonate formed within the sediment after deposition. Recognizing that authigenic carbonate (*sensu lato*) encompasses the net addition of carbonate to sediments (or the sediment-water interface) via remineralization of organic matter as well as the replacement of primary sedimentary carbonate (dominantly biogenic in the modern era), we have used two different approaches to estimating precipitation rates for these end-member types of AC formation.

Many sediment cores have a net decrease in porewater calcium with depth (Fig 2). This feature generally corresponds to sites with <65 wt% carbonate and high pore fluid alkalinity, as well as high ratios of OC to carbonate (Table 2). These 'Type I' sites often show complete net sulfate removal from modern seawater levels of ~28 mM (Walter et al., 1993), suggesting high rates of sulfate reduction within the upper tens of meters. High sulfate reduction rates coupled to the oxidation of a light-δ^{13}C source, indicates that these sites will have low-δ^{13}C pore fluids. The extent of organic matter remineralization can often be inferred from alkalinity profiles as well, because the anaerobic oxidation of organic matter generates carbonate alkalinity. The pore fluid geochemistry at these sites – specifically the net removal of Ca coupled to the depletion of sulfate – makes them excellent candidates to calculate net precipitation of AC directly from Ca concentrations.

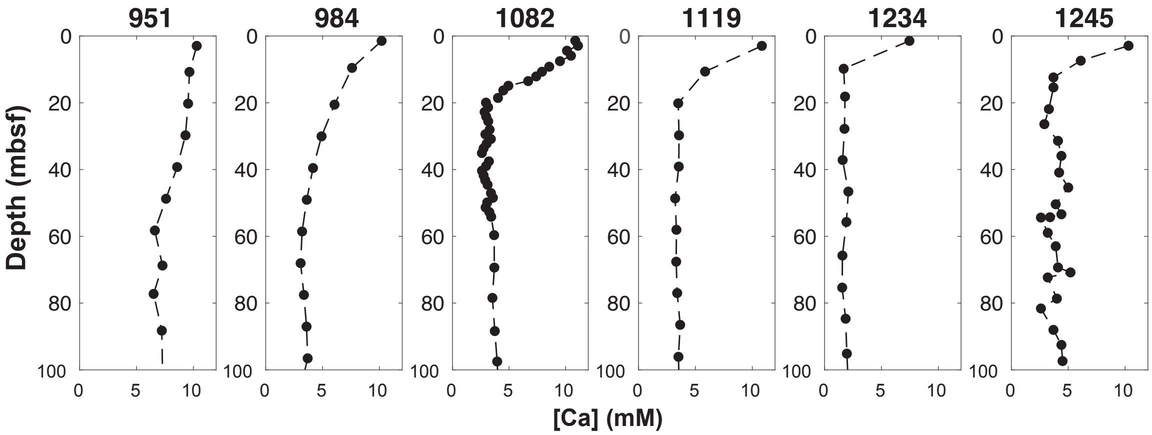

Figure 2. Pore fluid calcium concentrations (mM) for examples of Type I sites (< 65 wt% carbonate and OC/(AC+BC) > 0.1.

'Type II' sediments are composed of high percentages (>65 wt%) of carbonate and generally have much lower ratios of OC to carbonate than Type I sites (Table 2) as well as minimal (<10%) reduction in sulfate. Because of the limited extent of net sulfate reduction, low pore fluid alkalinity, and pore fluid [Ca] that increase with depth, we infer that essentially all AC at Type II sites is generated from recrystallization of primary sedimentary carbonate, rather than net precipitation via remineralization of organic matter. Without a mechanism to offset the δ^{13}C of the pore fluid ($\delta^{13}C_{PF\text{-}DIC}$), the recrystallized carbonate is indistinguishable from primary carbonate in terms of its δ^{13}C signature.

Leg	**Site**	**TA (mM)** ***low***	**TA (mM)** ***high***	**Xcarb**	**Xoc**	**Xoc / Xcarb (%)**	**Type**
165	998	2.96	4.73	0.72	0	0	II
130	805	2.9	5.36	0.91	0.001	0.11	II
177	1088	2.76	3.89	0.91	0.001	0.11	II
130	807	3.51	4.68	0.92	0.001	0.13	II
181	1120	2.74	4.6	0.95	0.002	0.19	II
177	1092	2.51	3.69	0.8	0.002	0.2	II
130	803	3.23	3.76	0.89	0.002	0.2	II
130	806	3.73	5.8	0.91	0.002	0.23	II
165	999	3.57	5.15	0.5	0.001	0.26	*
189	1169	3.98	5.84	0.85	0.003	0.39	II
194	1194	1.92	2.94	0.79	0.004	0.46	II
133	819	2.80	4.4	0.52	0.004	0.73	*
166	1003	2.17	26.03	0.94	0.008	0.88	II
117	725	3.67	17.31	0.54	0.007	1.28	I
157	951	3.26	4.96	0.49	0.008	1.67	I
157	950	4.1	6.2	0.58	0.01	1.72	I

162	984	3.98	14.18	0.16	0.003	1.79	I
202	1234	10.95	72.84	0.4	0.013	3.15	I
181	1119	2.18	27.73	0.09	0.003	3.78	I
308	U1319	2.95	19.45	0.15	0.008	5.07	I
42	381	4.64	18.1	0.17	0.01	5.88	I
113	693	3.49	3.9	0.02	0.002	7.5	I
139	855	2.03	10.36	0.06	0.005	7.67	I
204	1245	8.26	67.83	0.1	0.009	8.9	I
202	1232	23.44	36.45	0.02	0.002	9	I
175	1082	2.02	74.32	0.48	0.051	10.53	I
96	618	6.46	21.54	0.08	0.01	12.5	I
347	M0059	4.2	206.1	0.17	0.034	20.26	I
313	M0027	1.07	4.02	0.02	0.004	21.39	I
175	1084	4.07	171.67	0.36	0.084	23.31	I
112	688	28.44	189.27	0.11	0.029	26.4	I
141	860	16.7	46.98	0.02	0.006	28.08	I
146	892	14.71	20.48	0.04	0.015	37.5	I
141	863	3.65	20.79	0.01	0.004	39.83	I
112	681	13.99	21.82	0.04	0.023	57.5	I
169S	1033	3.75	89.1	0.02	0.013	64.36	I
169S	1034	3.79	115	0.01	0.015	150.5	I

Table 2. Sites included in this study categorized as Type I or Type II sites. Exceptions denoted with '*' and discussed in section SI.6 of Supplemental Material. Range of total alkalinity (TA) measured in pore fluids over the top ~80 meters of sediment. Xcarb = kg carbonate/kg sediment and Xoc = kg organic carbon/kg sediment averaged over the top ~80m.

Rates of AC formation in deep-sea sediments have been estimated using Sr concentration and ^{87}Sr/^{86}Sr values (Fantle and DePaolo, 2006; Richter and DePaolo, 1987,1988). Others have used Ca and Sr concentrations, and ^{44}Ca/^{40}Ca ratios (Fantle and DePaolo, 2007; Sun and Turchyn, 2014; Turchyn and DePaolo 2011). For Type II sites we use porewater Sr concentration data (Fig 3) to estimate the formation rate of secondary (authigenic) carbonate. As shown by Fantle and DePaolo (2006, 2007), Sr concentrations give a reasonably good estimate of average recrystallization rates in the uppermost 80 meters of most carbonate rich sections, although these estimates can be refined somewhat with use of Sr isotopes and Ca isotopes. For our purposes, we use only Sr concentration data because these data are available for a much larger number of sites. Our modeling approach for Type II sites involves an analytical solution to an advection-diffusion-reaction equation, yielding a single average value for the AC formation rate over a reaction length that is generally between 45 and 226 meters.

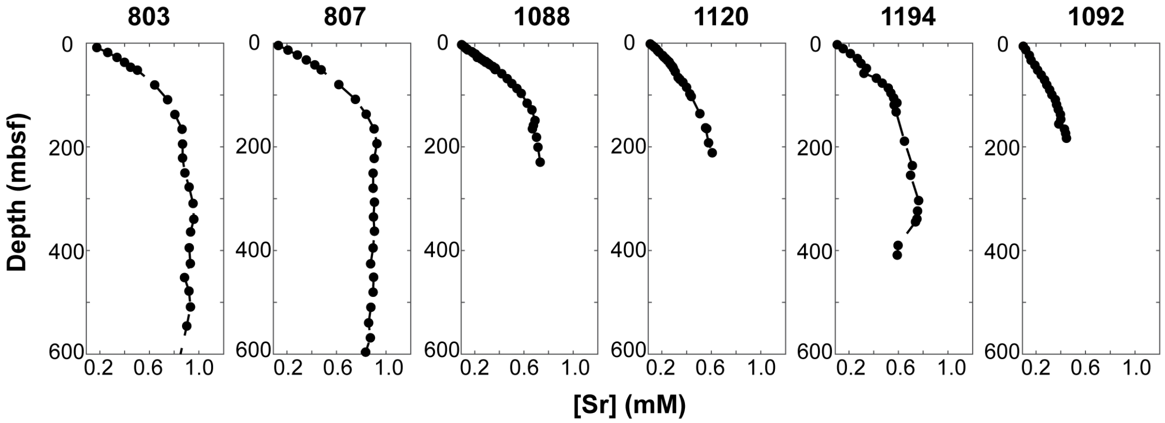

Figure 3. Pore fluid strontium concentrations (mM) for examples of Type II sites.

For Type I sites, Sr concentration and isotopic data are much more complicated to interpret (e.g. Turchyn and DePaolo, 2011) because of Sr sourcing to pore waters via alteration of volcanic ash and detrital non-carbonate minerals (Hawkesworth and Elderfield, 1978). For Type I sites with available Sr pore fluid data, only two sites (618 and 892) have Sr pore fluid profiles which plateau at depth and therefore allow for the calculation of a reaction length. Because we expect net additions of AC from Type I sites due to the higher pore fluid alkalinity, an appropriate means of estimating this component is by using pore fluid Ca concentrations. Although Ca is involved in other reactions, changes in calcium should be mainly due to the formation and dissolution of carbonates. Consequently, we use a similar advection-diffusion-reaction model utilizing porewater calcium concentrations, wherein we calculate advection and diffusion terms numerically from calcium concentrations, then invert for AC formation rate as a function of depth. We calculate fluxes from rates via integration to 80 meters below the seafloor (mbsf). This captures the depth range of AC production that is likely to affect the global value of $\delta^{13}C_{M\text{-}DIC}$, taking into account that the characteristic diffusion time of DIC in porefluids over an 80m depth interval is roughly equal to the seawater residence time of M-DIC (ca. 10^5 years). More details and discussion of the models used are provided in the Supplemental Material.

2.2.2 Relative carbon burial fluxes

We compare the total rate of AC formation per unit area of seafloor to the overall burial rates of carbonate and OC at each site. The rate of AC formation per unit area of seafloor is obtained by integrating the rate per unit volume of sediment over depth from the seafloor to a prescribed depth in the sediment column. For Type II sites, BC is partially converted to AC, but there is (virtually) no carbonate added to the section during this process. For Type I sites, all of the AC formation calculated using our porefluid Ca concentration approach is added to the section during burial.

The total carbonate burial flux for each site is given by:

$$\text{Total Carbonate Flux (mol m}^{-2}\text{ yr}^{-1}) = \frac{X_{carb}\,\rho_{sed} S\,(1-\phi)}{FW_{carb}} \qquad [6]$$

where S is sedimentation rate (m/yr), ϕ is average porosity, X_{carb} is mass fraction of carbonate, ρ_{sed} is assumed to be 2700 kg/m^3 and FW_{carb} is the molar mass of $CaCO_3(s)$. The burial flux of organic carbon is calculated similarly:

$$\text{Organic Carbon Flux (mol m}^{-2}\text{ yr}^{-1}) = \frac{X_{org}\,\rho_{sed} S\,(1-\phi)}{FW_{C}} \qquad [7]$$

where X_{org} is the volume fraction of organic carbon and FW_C is the molar mass of elemental carbon. We calculate ϕ, X_{carb} and X_{org} over an 80m averaging interval. Although these parameters can change considerably over this length scale, it is the depth-integrated flux, not the depth-specific rate that we need to estimate. The authigenic carbonate flux is the difference between the total carbonate flux and the biogenic carbonate flux. The sum of the three individual fluxes is equal to the total C burial flux (mol m^{-2} yr^{-1}) (Tables SI.2.1-1 and SI.2.2-1). The fractions in Fig. 6 are computed as follows:

$$f_{OC} = \text{organic carbon flux/total C flux} \qquad [8]$$
$$f_{BC} = \text{biogenic carbonate flux/total C flux} \qquad [9]$$
$$f_{AC} = \text{authigenic carbonate flux/total C flux} \qquad [10]$$

2.3 Carbon isotope measurements

Carbon isotope compositions of bulk carbonates for sites 807 and 1082 were measured at the Center for Stable Isotope Biogeochemistry Laboratory at the University of California, Berkeley. Measurements were made on a GV IsoPrime mass spectrometer with Dual Inlet MultiCarb system using 10-100µg powdered samples, reported using the Vienna Pee Dee Belemnite standard (V-PDB). Long-term precision is ±0.05‰ (1 s.d.).

3. Results & discussion

3.1 Sedimentary fractions of authigenic carbonate (f_{AC})

For reference, a typical sedimentation rate at many high-carbonate sites is roughly 20 m Myr^{-1}, which corresponds to 350 mmol C m^{-2} yr^{-1} assuming porosity is 0.7 and X_{carb} = 0.9. In contrast, net rates of AC formation for Type I sites generally range from 0 to 55.4 mmol m^{-3} yr^{-1} (Fig 4), corresponding to median and maximum fluxes of 0.3 and 25.4 mmol m^{-2} yr^{-1}, respectively (Table S-1), or 10-10^3 times smaller than a typical carbonate depositional flux. The larger Type I AC fluxes are found in sites located closer to shelf and slope areas and correspond to higher rates of sedimentation and sulfate reduction (Canfield, 1991). A key characteristic of the Type I sites is that even for those sites with higher AC fluxes (Table S-1) the f_{AC} values are very small (Fig 5). For example, site

1082 has one of the highest AC fluxes of 2.4 mmol m^{-2} yr^{-1}, but an f_{AC} value of only 0.004 because of the high sedimentation rate, including sedimentation of both OC and BC. Similarly, site 618, with a maximum flux roughly two orders of magnitude higher than the median, has the highest f_{AC} value, which is still only 0.014. These AC fluxes and f_{AC} values are on average much smaller than the fluxes calculated for carbonate-rich sections.

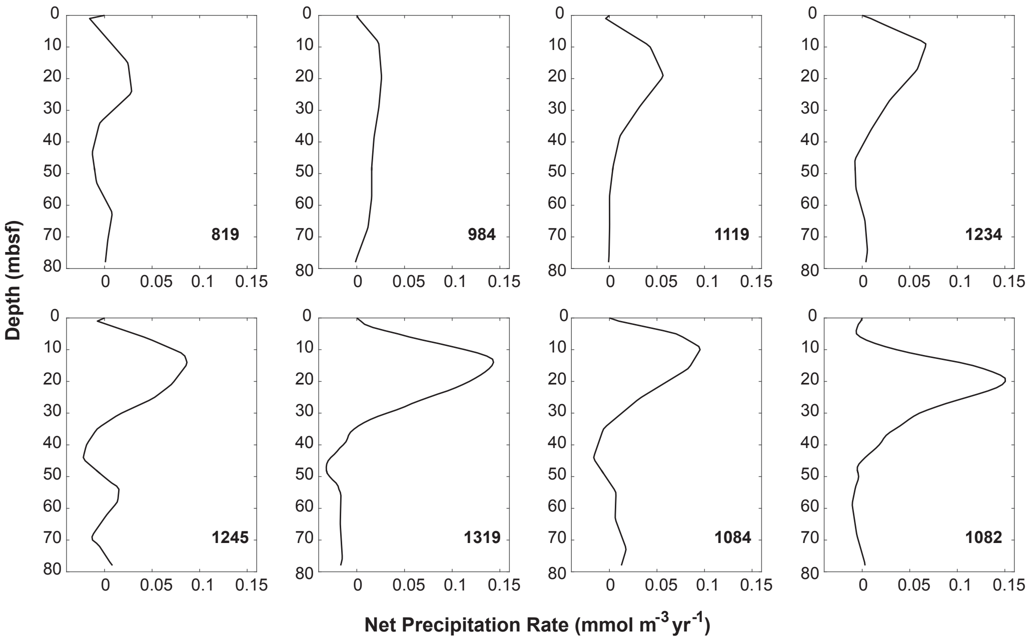

Figure 4. Type I sites with high net precipitation rates of authigenic carbonate and typical depths of maximum rates (~10-20 mbsf).

For Type II sites, the calculated reaction length (L), sedimentation rate (S), percent calcite, percent organic carbon, and model AC formation rates (“recrystallization rates,” R) are listed in (Table S-2). The recrystallization rates are all smaller than 0.2 Myr^{-1}. The fitting of Sr concentration for all sites is shown in Supplementary Figure S-1. A key characteristic of Type II sites is that the rate of AC formation can be quite high (up to 126 mmol m^{-2} yr^{-1}), which is a substantial fraction of the typical total carbonate burial rate, and corresponds to f_{AC} values of up to 0.72

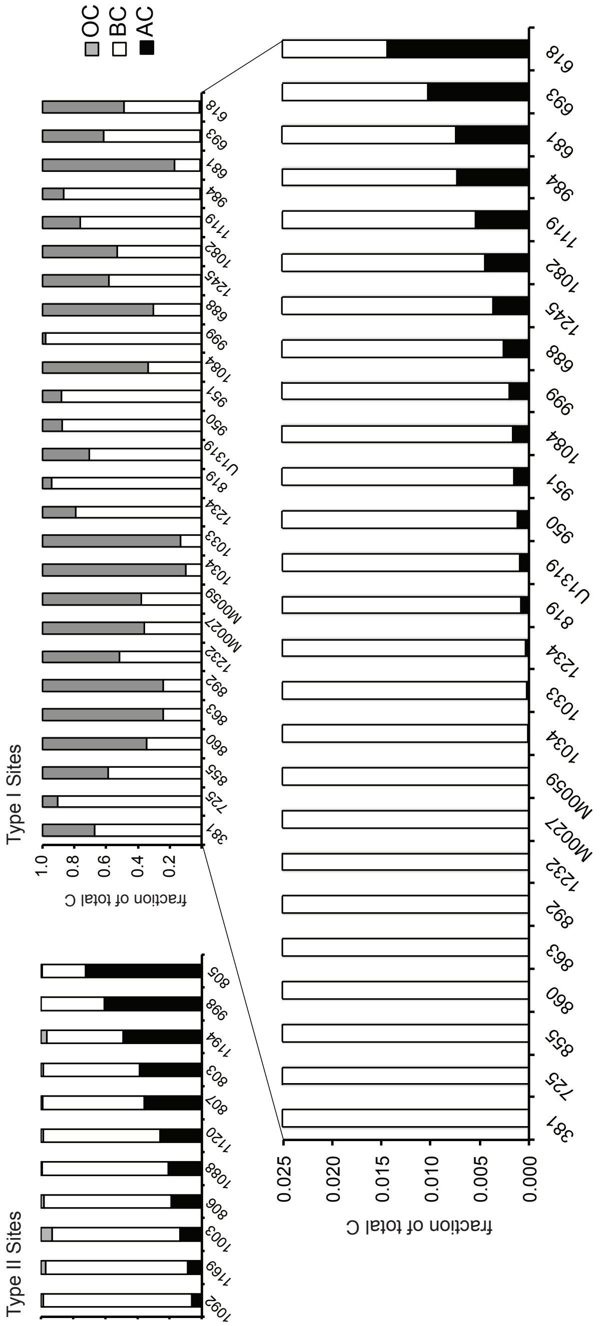

Figure 5. Stacked bars showing sedimentary carbon fractions (AC = authigenic carbonate (black), BC = biogenic carbonate (white), OC = organic carbon (grey)) for each site, separated by site type. Note the lower panel is inset of Type I plot showing fractions 0 to 0.025 which cannot be seen on coarser scale diagram.

The relative authigenic, organic and biogenic carbon burial fractions for the sites analyzed are summarized in Figure 6. Depth-dependent rates for Type I sites with highest AC precipitation rates are shown in Figure 4 for all but site 618, which is discussed in Section 3.2.3.1. These sites all share similar depths of maximum AC production, roughly 10-20 meters below the seafloor. For Type I sites, the relative burial fractions of biogenic carbonate and organic carbon vary over a large range (Fig 6) but the corresponding burial fraction of AC is small (Fig 5); in all cases less than about 0.02 and in most cases less than 0.01. Reimers et al. (1996), in their study of uppermost sediments in the Santa Barbara Basin, also found that in spite of significant increases in pH and carbonate alkalinity, the increase in authigenic calcite in sediments only increased the sedimentary carbonate content by 0.1%.

For Type II sites, because of the small extent of organic carbon oxidation inferred from pore fluid profiles, we expect the PF-DIC and therefore AC to have virtually the same δ^{13}C as BC (i.e., $f_{AC}* = 0$) unless there are other means of resetting the $\delta^{13}C_{PF\text{-}DIC}$, which we explore in section 3.2. Overall, our initial analysis leads to the conclusion that AC formation in late Cenozoic marine sediments has a negligible impact on the global δ^{13}C balance, regardless of depositional environment.

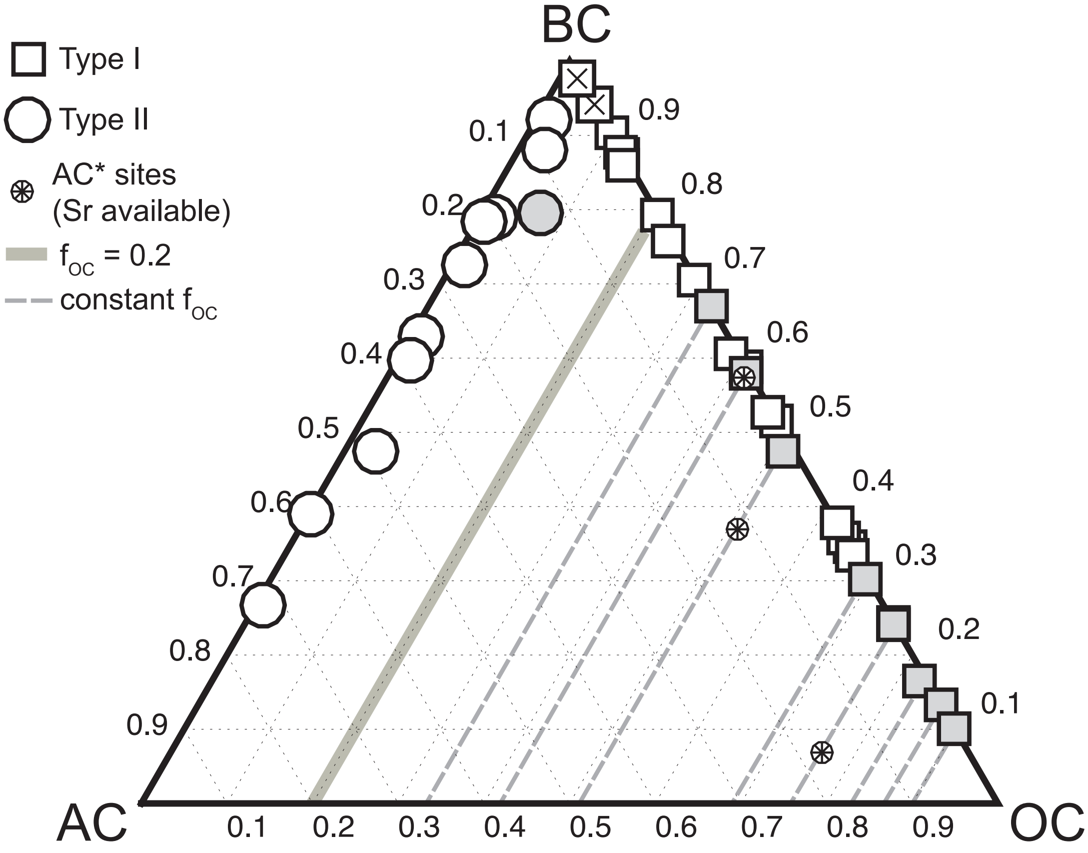

Figure 6. Ternary plot showing relative sedimentary carbon fractions (f) of authigenic carbonate (AC), biogenic carbonate (BC), and organic (OC) carbon for Type I sites (squares) and Type II (circles). Grey shading indicates sites representing localized environments discussed in section 3.2.3. Squares with 'X' indicate sites 819 and 999, which have < 65wt% carbonate and OC/(AC+BC) ratios < 0.1 and therefore do not fit

quarely into Type I/II classification. Small circles with '*' show sedimentary carbon fractions for sites 618, 892, 1245, where estimates of AC* due to recrystallization can be calculated (Sr data available and Sr changes with depth indicative of recrystallization). Solid grey line denotes constant f_{OC} of 0.2 (estimate of modern value). Dashed grey lines denote constant f_{OC} values corresponding to sites discussed in section 3.2.3, indicating the theoretical range of f_{AC} and f_{BC} values as a function of extent of recrystallization.

3.2 Evidence from $\delta^{13}C$

3.2.1 Type I approach

As a check on our results, we compare $\delta^{13}C_{PF\text{-}DIC}$ and carbonate $\delta^{13}C$ values at sites where data are available to evaluate AC*/BC. At site 1082, complete sulfate reduction coincides with the depth of minimum $\delta^{13}C_{PF\text{-}DIC}$ (Fig 7) demonstrating that the porefluid $\delta^{13}C$ approaches that of oxidized organic matter. Porefluid calcium approaches a plateau at ~20 mbsf, indicating no net precipitation below this depth.

If we assume that all AC at site 1082 precipitates with the $\delta^{13}C_{PF\text{-}DIC}$ composition of -20, the small average isotopic shift from M-DIC values in the bulk carbonate, which averages -0.35 (Fig 7), requires that f_{AC} be small, close to the value of 0.004 over the top 80 meters calculated from our approach. The low $\delta^{13}C$ of PF-DIC (Fig 7) also confirms the inferences of Teichert et al. (2009), based on similar sections from Leg 204, and Turchyn and DePaolo (2011), based on Sites 984 and 1082, that dissolution rates are exceptionally low in the parts of sections undergoing maximum sulfate reduction and secondary carbonate precipitation. In spite of isotopically depleted pore fluids of site 1082, we do not see a significant shift in the carbonate $\delta^{13}C$ because of such low AC/BC.

3.2.2 Type II approach

Site 807, a Type II site, exhibits a <2 mM decrease in porewater sulfate relative to modern seawater values (28 mM) over an interval of 100 meters (Kroenke et al., 1991). Although sulfate is not the only terminal electron acceptor that can be utilized in the remineralization of organic matter, we would expect an increase in pore fluid alkalinity to reflect other anaerobic oxidation pathways as well, which is not observed (Fig 7). Although pore fluid $\delta^{13}C$ are not available for site 807, the bulk carbonate isotopic composition that we measure (Fig 7) can also provide insight into the carbon isotopic composition of the pore fluid. Our modeling suggests that the AC fraction at site 807 is ~0.36. If f_{AC}* were significant, the bulk carbonate isotopes should be noticeably offset from $\delta^{13}C_{M\text{-}DIC}$, which is not the case (Fig 7). If we assume the biogenic carbonate is ±0.3‰, then the value of Δ_{AC} is at most ±2.2‰. Other sites with minimal alkalinity production in the pore fluids and elevated sulfate concentrations throughout likely also have negligible f_{AC}.

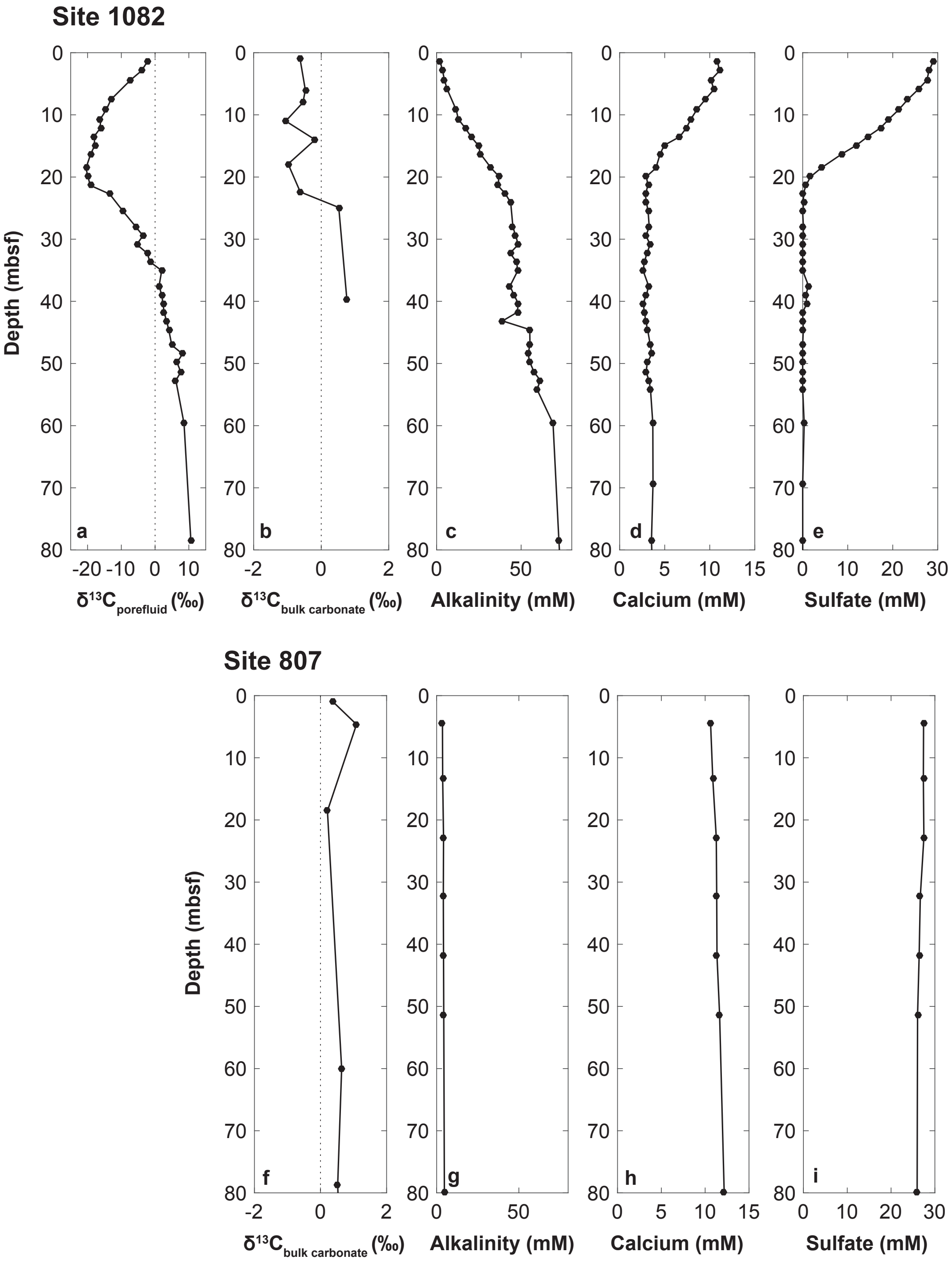

Figure 7. Pore fluid bulk carbonate chemistry of Type I and Type II sites 1082 and 807, respectively. (a) Site 1082 pore fluid carbon isotopes from Moore et al. (2004); (b) Isotopic composition of bulk carbonates from site 1082 (this study); (c), (d) and (e) Site 1082 pore fluid data from Wefer et al. (1998); (f) Isotopic composition of bulk carbonates from Site 807 (this study); (g), (h) and (i) Site 807 pore fluid data from Kroenke et al. (1991).

3.2.3 Localized environments

In the following discussion we evaluate whether a high AC*/BC ratio is possible in modern marine sediments, and if so, what specific conditions allow for it. Although not globally representative, we look at sites in more extreme localized environments than those of sites 1082 and 807 that may be representative of different paleoenvironments. We focus on carbonate-dominant site 1003 (Bahamas Transect) as well as lower-carbonate sites with high pore fluid alkalinity thought to be producing AC today. These sites include those in close proximity to gas hydrates and/or methane seeps (Sites 681 and 688, Peru Continental Margin; Sites 892 and 1245, Cascadia Margin) and sites located in anoxic bottom waters (Sites 1033 and 1034, Saanich Inlet; Site 618, Orca Basin in Gulf of Mexico; Site 381, Black Sea).

3.2.3.1 Anoxic bottom water

Site 618 is located beneath 200 meters of hypersaline brine in anoxic bottom waters of the Orca Basin (Bouma et al. 1986). Because of high and variable porewater salinity, our methodology is not necessarily appropriate for estimating AC formation rates. By correcting Ca to Cl concentrations (where $M^{corr} = M(z)/(Cl(z)/Cl(o))$), it is evident there is not a significant net change in Ca independent of the salinity gradient. However, Sr^{corr} reaches a plateau at ~50 meters (Fig S-3). If this trend reflects recrystallization, then f_{AC} would be 0.12, with $f_{BC} = 0.37$ (Fig 6). In this section, hydrates and gas pockets with up to 98% methane (Bouma et al., 1986) provide low-$\delta^{13}C$ carbon, with CH_4 gas samples averaging -73.5‰. Anaerobic oxidation of methane (AOM) in these sediments could very well promote high AC*/BC. It is noteworthy that this site also has $f_{OC} = 0.51$, and therefore production of low-$\delta^{13}C$ carbonate is still associated with burial conditions that would be expected to produce increasing atmospheric O_2 if applied globally.

Sites 1033 and 1034 are found in anoxic bottom waters of the Saanich Inlet, with alkalinity reaching ~80 and 100 mM, respectively, by 50 mbsf (Fig S-8). Our calculations reveal that there is no net AC formation in these sections when averaged over the top 80 meters, due to dissolution over the 50-80 meter interval. These sites are another example of where the AC*/BC ratio may be significant. As with Site 681, these sites also have $f_{OC} \approx 0.90$ (Fig 6) and hence the low-$\delta^{13}C$ AC would be associated with high rates of OC burial.

3.2.3.2 Carbonate platforms and periplatform sediments

Carbonate platforms are of particular interest because they may represent the modern sedimentary environment that most closely matches those in the geologic record prior to the Jurassic (Saltzman and Thomas, 2012). Site 1003 of the Bahamas resembles other Type II sites in its low ratio of OC to total carbonate (Table 2), relatively low deposition rate, and is roughly 94% carbonate by mass (however, >50% is aragonite). As highlighted by Swart and Eberli (2005) and Eberli et al. (1997), platform and periplatform carbonate sediments differ from pelagic sediments in key ways. One is that the dominant mineralogy of the primary carbonate is aragonite rather than calcite, and the other is that seawater flows through the system horizontally so that it is not possible to fully capture the pore-fluid interaction with the solid using a one-dimensional model. Bulk carbonates measure +1 to +5‰ (Swart and Eberli, 2005), but interpreting the $\delta^{13}C$ of solids at this site is complicated, as it is not clear the extent to which this signal is from banktop-sourced material or *in situ* alteration. Downcore changes in mineralogy suggest a substantial amount of recrystallization. This section may represent one model for high AC*/BC, but also constitutes an environment where f_{OC} is much lower than 0.2 (Fig 6).

3.2.3.3 Continental margin sites

Many continental margin sites, including the Peru and Cascadian margins, have been studied for their authigenic carbonate production. These sites occupy regions of gas hydrate formation-dissociation and produce AC that can have both low and high $\delta^{13}C$. Meister et al. (2007) report "soft sediment" solid $\delta^{13}C$ values from the Peru Margin ranging from -17.01 to +4.83 in core 681 (reoccupied during Leg 201 as core 1229), with dolomite samples from this core ranging from -13.6 to +6.09. Site 688, also on the Peru margin, shows porefluid Ca and Mg behavior indicative of net precipitation of low-Mg calcite or aragonite followed by dolomitization at depth. As of 1988, Site 688 had the highest alkalinity ever recorded in the Ocean Drilling Program (Suess et al., 1988). Increasingly lower chlorinity with depth as evidence of gas hydrate dissociation suggests this alkalinity increase is the result of CH_4 oxidation. Although carbonate $\delta^{13}C$ data are not available to the best of the authors' knowledge, the incorporation of methane-derived $\delta^{13}C$ into the dolomicrite found at this site would likely promote high f_{AC}*.

Site 1245 on the Cascadian margin shows a range of $\delta^{13}C$ in the PF-DIC, of ~-20 to ~+1 within the top 100m (Tréhu et al., 2003), with the isotopic minimum coeval with sulfate depletion (Fig S-9), similar to site 1082. Pore fluid alkalinity also reaches ~70 mM by 100 m, concurrent with a spike in dissolved HPO_4^-, suggesting that organic matter remineralization rather than AOM is the main contributor to the depleted fluid composition. Strontium concentrations change very little with depth, indicating that recrystallization is not an important process in forming authigenic calcite at this site. Net formation of authigenic calcite comprises less than 1% of the total sedimentary carbonate at the site according to our calculations. Near-complete sulfate removal (from 24.7 mM to 0.4 mM) occurs with a concurrent drawdown in Ca from 10.3mM to 3.7mM over the top ~12 meters, after which both sulfate and calcium remain constant with depth (Fig S-9). Tréhu et al. (2003) note AC forming in clay-rich layers as discrete Mg-calcite nodules (likely high-Mg calcite) in the upper ~45 meters of sediment. Neither mineralogical analyses nor pore fluid chemistry suggest dolomite precipitation as a dominant authigenic phase at site 1245. Similar pore fluid chemistry and fractions of total carbonate to that of site 1082 (Table S-1 and Fig 7) suggests the overall effect of organic carbon remineralization on the $\delta^{13}C$ of total carbonate is small.

ODP site 892, located on Hydrate Ridge of the Cascadian Margin, has both aragonite layers and high Mg-calcite cement inter-grown with gas hydrates (Bohrmann et al., 1998). In contrast to site 1245, the Ca concentrations at site 892 increase with depth as Mg concentrations decrease (Fig S-6). Along with increasing Sr concentrations with depth, these geochemical trends suggest the replacement of aragonite (into which Sr preferentially partitions) with high-Mg calcite. This interpretation is consistent with carbon and oxygen isotope data from Bohrmann et al. (1998), linking formation of the high Mg-calcite with the dissociation of the methane hydrates. There may be no net addition of AC at this site, but if we apply our Sr method to estimate recrystallization, our calculations yield f_{AC} of 0.165 (Fig 6), over two times the amount of biogenic or primary carbonate present. With $\delta^{13}C$ of carbonates in the range -40.6 to -54.2 (Bohrmann et al., 1998), this site is an example of high AC*/BC.

3.3 Conditions of AC* production

We have explored sediment cores that represent many different depositional environments, some of which are thought to have been more prevalent in the past. We acknowledge that our findings are limited by the extent to which sedimentary processes today may have been active in various paleoenvironments, and that the geologic record is incomplete. Despite this uncertainty, there are specific observations that help elucidate the role of AC in the global carbon isotope balance through geologic time. The sites discussed in the preceding sections allow us to identify where and how authigenic carbonate could make up an isotopically significant fraction of total sedimentary carbon.

Today, it appears as though large f_{AC}* can be generated via AOM at or near sites of gas hydrate dissociation, as shown in sites 681 and 688 of the Peru Margin, site 892 of the Cascadian Margin, and site 618 of the anoxic Orca Basin. Sites 1082 or 1245, in which there is evidence of organic matter remineralization but not AOM, have a very small shift in the bulk carbonate solid $\delta^{13}C$ composition in spite of isotopically depleted pore fluids. High rates of organic matter remineralization and AC production at sites such as these are countered in their isotopic effect by high biogenic carbonate (or primary sedimentary carbonate) fractions with $\delta^{13}C$ very close to that of M-DIC.

Carbonate platforms and periplatform sediments may be a key, and somewhat complicated, aspect of the authigenic carbonate story. It is not clear in our analysis that a significant amount AC* is produced *in situ* at site 1003, in spite of carbonate platforms showing extensive diagenesis (Eberli et al., 1997). The mixing of banktop sediment with pelagic calcifiers causes an overall diluting of isotopically offset signals. If the source of the high porefluid alkalinity in periplatform sediments is a mixture of recrystallizing banktop and biogenic sediment as well as from the remineralization of organic matter, arguably the high $\delta^{13}C$ signature in the bulk carbonate will be slowly shifted towards low $\delta^{13}C$ values. Given how difficult it is to offset the bulk carbonate $\delta^{13}C$ in a site like 1082, which has much lower overall carbonate than site 1003, it seems unlikely that these periplatform sediments can remineralize enough organic matter to create high AC*/BC. However, fractionation of DIC during aragonite precipitation and distillation effects during photosynthesis (Swart and Eberli, 2005) suggest that the banktop itself could be an important locus of AC precipitation.

3.4 AC* formation in Earth history

During past times of ocean anoxia, seafloor carbonate precipitates are thought to be widespread (Grotzinger and Knoll, 1995; Higgins et al., 2009; Pruss et al., 2006). If past seafloor carbonates formed in similar environments to the gas hydrate continental margins seen today, they may have affected $\delta^{13}C_{M\text{-}DIC}$ even if they weren't widespread. If oceans were anoxic, then supersaturated bottom waters could have promoted the expansion of these carbonates beyond the amount proportional to initial alkalinity generated via CH_4-oxidation. It is possible that following production of carbonate from CH_4-oxidation, $\delta^{13}C$ of the precipitates would shortly evolve back to $\delta^{13}C_{M\text{-}DIC}$. Therefore, it is unclear whether extensive seafloor precipitation of carbonates could perturb $\delta^{13}C_{M\text{-}DIC}$, even during anoxic intervals. It is expected that on short timescales (10^4-10^5 years), biogenic carbonate production would diminish when waters were anoxic (Pruss et al., 2006), shifting the AC/BC ratio higher.

Total size of the DIC pool is expected to be an important factor in determining the effect of AC precipitation on $\delta^{13}C_{M\text{-}DIC}$. The M-DIC reservoir has become smaller since the Proterozoic, and so has the magnitude of variations in $\delta^{13}C_{M\text{-}DIC}$ (Bartley and Kah, 2004). Bartley and Kah (2004) argue that coupling of organic matter and biogenic carbonate production with the proliferation of calcifying nannoplankton created isotopic buffering against changes to $\delta^{13}C_{M\text{-}DIC}$. This link suggests perturbations to $\delta^{13}C_{M\text{-}DIC}$ due to AC were more likely in the Precambrian and intervals in the Phanerozoic (e.g., early Cambrian) when calcifying organisms were not as prolific as they are in modern oceans.

3.5 Global versus local $\delta^{13}C$

The use of $\delta^{13}C$ to interpret global paleoenvironment hinges on the assumption that what is recorded represents a global $\delta^{13}C_{M\text{-}DIC}$ value. The pre-Jurassic record is generally sourced from shallow-water sediments, which in the modern ocean show atypical high AC*/BC. Hence, it is possible that pre-Jurassic $\delta^{13}C$ might be reflecting an integrated signal of local conditions in the water column and/or AC production with $\delta^{13}C_{M\text{-}DIC}$, and therefore would not necessarily appear geochemically or petrologically distinct from carbonates reflecting global marine conditions aside from their $\delta^{13}C$ composition.

4. Conclusions

In this study, we sought to use the abundant and systematic pore fluid chemical data available from the deep sea drilling archive to evaluate the potential role of authigenic carbonate formation in marine sediments in affecting the carbon isotopic composition of marine DIC. Our specific approach is to evaluate the *relative* rates of formation/burial of biogenic (or primary sedimentary), organic, and authigenic carbon (BC:OC:AC) in an array of late Cenozoic marine sedimentary environments chosen to encompass a range of sediment compositions, sedimentation rates, oxygenation conditions, and water depths. The goal was to estimate the likely range of modern proportions of different carbon burial rates, and to determine what site characteristics, if any, would be most favorable to making AC a major factor in the $\delta^{13}C$ budget. Such site characteristics might be rare in the modern oceans but could have been more prevalent in Mesozoic, Paleozoic, or Precambrian oceans.

In analyzing modern sites and considering possible differences between modern sedimentary environments and those of the past, we find only a few characteristics that can change in a way that would promote the needed formation of AC* (AC that is isotopically distinct from BC). One possibility is to have an OC/BC ratio substantially higher than the long-term average of 0.2 with an AC/BC ratio of at least 0.1. This, however, does not change the idea that high $\delta^{13}C_{M\text{-}DIC}$ values correspond to excess organic carbon burial, which is already accounted for in the isotope model with only BC and OC.

An environment that might be expected to have significant AC* production, but does not, is site 1082, a continental margin site in the South Atlantic. This site might be expected to have a high AC*/BC burial ratio, because of its location in an upwelling zone, high pore fluid alkalinity, complete sulfate removal, and high X_{oc}/X_{carb} ratio. However, our analysis shows that AC*/BC is two orders of magnitude too small to be significant at this site. The high carbonate site 807 (Ontong-Java Plateau), in contrast, is an example of where there is high AC/BC, but no means of creating AC*. These two site types have been widespread since the Jurassic, and so for this span of time, authigenic carbonate likely has had no material effect on the $\delta^{13}C$ of the ocean. Prior to this, understanding the role of AC is more difficult because the record is derived mainly from shallow marine environments, for which diagenetic processes are typically different in comparison to deep sea environments, and which can record $\delta^{13}C$ values that deviate from the global ocean (Saltzman and Thomas, 2012). Our difficulty in finding example environments that would be favorable for making AC* a significant component of the global $\delta^{13}C$ balance leads us to conclude that such environments may not exist.

We explored sites in the ODP database that, although highly localized today, perhaps hosted extreme enough conditions to have high AC*/BC. The most convincing locus of high AC*/BC is in continental margins where dolomitization and other carbonate recrystallization occurs with gas hydrate formation-dissociation and where anaerobic methane oxidation is dominant. Restricted or semi-restricted basins with anoxic bottom waters could also be sites of high AC*/BC, but it is likely that methane, rather than organic matter, needs to be the main source of isotopically light $\delta^{13}C$ for AC* production. Finally, carbonate platforms and periplatform sediments may be settings of high AC*/BC production, but the interpretation of bulk carbonate $\delta^{13}C$ requires a different model that accounts for additional factors.

On long timescales (order 10 My), if more extreme environments like those explored above were globally extensive, it is possible that AC production could influence the $\delta^{13}C$ budget. However, if pelagic calcifying organisms comprise significant fractions of total sedimentary carbon, as is thought to be the case for much of the Phanerozoic, it is unlikely that these high AC*/BC conditions were sufficiently widespread. Prior to the proliferation of calcifying organisms, and specifically in the Precambrian, these environments could have been more likely given the decreased isotopic buffering effect provided by biogenic carbonate.

It is not clear that a steady state approximation is appropriate for interpreting isotope excursions. It is possible that if isotope excursions are reflecting authigenic carbonate, they are a local signal, such as those observed today in carbonate platforms and AOM-dominant environments with low BC. Extensive AC formation on timescales of observed excursions is possible only with equally transient phenomena such as global methane hydrate release, as is thought to have occurred at the Paleocene-Eocene boundary (Dickens et al., 1995). This possibility, however, implies that any isotopic effect of authigenic carbonate production is secondary to the impact of an environmental perturbation on the $\delta^{13}C$ of the ocean and therefore may not require inclusion in an isotopic mass balance model.

Acknowledgements

The authors thank David Fike, Galen Halverson, and John Higgins, whose insightful comments helped improve the manuscript considerably. The authors also thank Wenbo Yang for measuring carbon isotopes of bulk carbonate samples and Holly Barnhart for helping to compile carbon isotope data for Figure 1. This research was supported by the U.S. Department of Energy, Office of Science, Office of Basic Energy Sciences, Chemical Sciences, Geosciences, and Biosciences Division, under Award Number DE-AC02-05CH11231.

References

Arthur, M.A., Dean, W.E. and Pratt, L.M., 1988. Geochemical and climatic effects of increased marine organic carbon burial at the Cenomanian/Turonian boundary. *Nature*, *335*(6192), pp.714-717.

Bartley, J.K. and Kah, L.C., 2004. Marine carbon reservoir, Corg-Ccarb coupling, and the evolution of the Proterozoic carbon cycle. *Geology, 32*(2), pp.129-132.

Berner, R.A. and Canfield, D.E., 1989. A new model for atmospheric oxygen over Phanerozoic time. *American Journal of Science*, *289*(4), pp.333-361.

Berner, R.A. and Maasch, K.A., 1996. Chemical weathering and controls on atmospheric O2 and CO2: fundamental principles were enunciated by JJ Ebelmen in 1845. *Geochimica et Cosmochimica Acta*, *60*(9), pp.1633-1637.

Berner, R.A. and Petsch, S.T., 1998. The sulfur cycle and atmospheric oxygen. *Science*, *282*(5393), pp.1426-1427.

Bohrmann, G., Greinert, J., Suess, E. and Torres, M., 1998. Authigenic carbonates from the Cascadia subduction zone and their relation to gas hydrate stability. *Geology*, *26*(7), pp.647-650.

Bouma, A. H., Coleman, J. M., Meyer, A. W., et al., 1986. Initial Reports. Deep Sea Drilling Program, 96: Washington (U.S. Govt. Printing Office).

Canfield, D.E., 1991. Sulfate reduction in deep-sea sediments. *American Journal of Science*, *291*(2), pp.177-188.

Canfield, D.E. and Kump, L.R., 2013. Carbon cycle makeover. *Science*, *339*(6119), pp.533-534.

Canfield, D.E. and Teske, A., 1996. Late Proterozoic rise in atmospheric oxygen concentration inferred from phylogenetic and sulphur-isotope studies. *Nature*, *382*(6587), pp.127-132.

Derry, L.A., 2014. Organic carbon cycling and the lithosphere. In *Treatise on Geochemistry: Second Edition*. Elsevier Inc.

Dickens, G.R., O'Neil, J.R., Rea, D.K. and Owen, R.M., 1995. Dissociation of oceanic methane hydrate as a cause of the carbon isotope excursion at the end of the Paleocene. *Paleoceanography*, *10*(6), pp.965-971.

Eberli, G.P., Swart, P.K., Malone, M.J., et al., 1997. Proceedings of the Ocean Drilling Program, Initial Reports, Vol. 166.

Fantle, M.S. and DePaolo, D.J., 2006. Sr isotopes and pore fluid chemistry in carbonate sediment of the Ontong Java Plateau: Calcite recrystallization rates and evidence for a rapid rise in seawater Mg over the last 10 million years. *Geochimica et Cosmochimica Acta, 70*(15), pp.3883-3904.

Fantle, M.S. and DePaolo, D.J., 2007. Ca isotopes in carbonate sediment and pore fluid from ODP Site 807A: The Ca2+(aq)–calcite equilibrium fractionation factor and calcite recrystallization rates in Pleistocene sediments. *Geochimica et Cosmochimica Acta, 71*(10), pp.2524–2546.

Farquhar, J., Savarino, J., Airieau, S. and Thiemens, M.H., 2001. Observation of wavelength-sensitive mass-independent sulfur isotope effects during SO2 photolysis: Implications for the early atmosphere. *Journal of Geophysical Research: Planets*, *106*(E12), pp.32829-32839.

Grotzinger, J.P. and Knoll, A.H., 1995. Anomalous carbonate precipitates: is the Precambrian the key to the Permian? *Palaios*, pp.578-596.

Halverson, G.P., Hoffman, P.F., Schrag, D.P., Maloof, A.C. and Rice, A.H.N., 2005. Toward a Neoproterozoic composite carbon-isotope record. *Geological Society of America Bulletin, 117(*9-10), pp.1181-1207.

Hawkesworth, C.J. and Elderfield, H., 1978. The strontium isotopic composition of interstitial waters from Sites 245 and 336 of the Deep Sea Drilling Project. *Earth and Planetary Science Letters, 40*(3), pp.423-432.

Higgins, J.A., Fischer, W.W. and Schrag, D.P., 2009. Oxygenation of the ocean and sediments: consequences for the seafloor carbonate factory. *Earth and Planetary Science Letters, 284*(1), pp.25-33.

Kroenke, L.W., Berger, W.H. and Janecek, T.R., 1991. Proceedings of the Ocean Drilling Program, Initial Reports, Vol. 130.

Kump, L. R. and Arthur, M.A., 1999. Interpreting carbon-isotope excursions: carbonates and organic matter. *Chemical Geology, 161*(1), pp.181-198.

Lowenstein, T.K., Kendall, B. and Anbar, A.D., 2014. The geologic history of seawater. In *Treatise on Geochemistry: Second Edition*. Elsevier Inc.

Marshall, J.D., Brenchley, P.J., Mason, P., Wolff, G.A., Astini, R.A., Hints, L. and Meidla, T., 1997. Global carbon isotopic events associated with mass extinction and glaciation in the late Ordovician. *Palaeogeography, Palaeoclimatology, Palaeoecology*, *132*(1-4), pp.195-210.

Meister, P., Mckenzie, J.A., Vasconcelos, C., Bernasconi, S., Frank, M., Gutjahr, M. and Schrag, D.P., 2007. Dolomite formation in the dynamic deep biosphere: results from the Peru Margin. *Sedimentology, 54*(5), pp.1007-1032.

Moore, T.S., Murray, R.W., Kurtz, A.C. and Schrag, D.P., 2004. Anaerobic methane oxidation and the formation of dolomite. *Earth and Planetary Science Letters, 229*(1), pp.141-154.

Morse, J.W., Arvidson, R.S. and Lüttge, A., 2007. Calcium carbonate formation and dissolution. *Chemical reviews*, *107*(2), pp.342-381.

Payne, J.L., Lehrmann, D.J., Wei, J.Y., Orchard, M.J., Schrag, D.P. and Knoll, A.H., 2004. Large perturbations of the carbon cycle during recovery from the end-Permian extinction. *Science, 305*(683), pp.506-509.

Pruss, S.B., Bottjer, D.J., Corsetti, F.A. and Baud, A., 2006. A global marine sedimentary response to the end-Permian mass extinction: Examples from southern Turkey and the western United States. *Earth-Science Reviews, 78*(3), pp.193-206.

Raven, J.A., Falkowski, P.G., 1999. Oceanic sinks for atmospheric CO_2. Plant, Cell and Environment 22 6, 741-755.

Reimers, C.E., Ruttenberg, K.C., Canfield, D.E., Christiansen, M.B. and Martin, J.B., 1996. Porewater pH and authigenic phases formed in the uppermost sediments of the Santa Barbara Basin. *Geochimica et Cosmochimica Acta, 60*(21), pp.4037-4057.

Retallack, G.J. and Jahren, A.H., 2008. Methane release from igneous intrusion of coal during Late Permian extinction events. *The Journal of Geology*, *116*(1), pp.1-20.

Richter, F.M. and DePaolo, D.J., 1987. Numerical models for diagenesis and the Neogene Sr isotopic evolution of seawater from DSDP Site 590B. *Earth and Planetary Science Letters, 83*(1), pp.27-38.
Richter, F.M. and DePaolo, D.J., 1988. Diagenesis and Sr isotopic evolution of seawater using data from DSDP 590B and 575. *Earth and Planetary Science Letters, 90*(4), pp.382-394.

Saltzman, M.R., 2005. Phosphorus, nitrogen, and the redox evolution of the Paleozoic oceans. *Geology, 33*(7), pp.573-576.

Saltzman, M.R. and Thomas, E., 2012. Carbon isotope stratigraphy. *The geologic time scale, 1*, pp.207-232.

Schidlowski, M., Eichmann, R. and Junge, C.E., 1975. Precambrian sedimentary carbonates: carbon and oxygen isotope geochemistry and implications for the terrestrial oxygen budget. *Precambrian Research*, *2*(1), pp.1-69.

Schrag, D.P., Higgins, J.A., Macdonald, F.A. and Johnston, D.T., 2013. Authigenic carbonate and the history of the global carbon cycle. *Science, 339*(6119), pp.540-543

Sephton, M.A., Looy, C.V., Veefkind, R.J., Brinkhuis, H., De Leeuw, J.W. and Visscher, H., 2002. Synchronous record of $\delta^{13}C$ shifts in the oceans and atmosphere at the end of the Permian. *Geol. Soc. Am. Spec. Pap, 356*, pp.455-462.

Shields, G. and Veizer, J., 2002. Precambrian marine carbonate isotope data- base: Version 1.1. *Geochemistry, Geophysics, Geosystems, 3*(6).

Sun, X. and Turchyn, A.V., 2014. Significant contribution of authigenic carbonate to marine carbon burial. *Nature Geoscience, 7*(3), p.201.

Swart, P.K. and Eberli, G., 2005. The nature of the δ^{13}C of periplatform sediments: Implications for stratigraphy and the global carbon cycle. *Sedimentary Geology*, 175, pp.115-129.

Teichert, B.M.A., Gussone, N. and Torres, M.E., 2009. Controls on calcium isotope fractionation in sedimentary porewaters. *Earth and Planetary Science Letters, 279*(3), pp.373–382.

Tréhu, A.M, Bohrmann, G., Rack, F.R., Torres, M.E., et al., 2003. *Proc. ODP, Init. Repts.,* 204: College Station, TX (Ocean Drilling Program). doi:10.2973/odp.proc.ir.204.2003

Turchyn, A.V. and DePaolo, D.J., 2011. Calcium isotope evidence for suppression of carbonate dissolution in carbonate-bearing organic-rich sediments. *Geochimica et Cosmochimica Acta, 75*(22), pp.7081-7098.

Walter, L.M., Bischof, S.A., Patterson, W.P., Lyons, T.W., O'Nions, R.K., Gruszczynski, M., Sellwood, B.W. and Coleman, M.L., 1993. Dissolution and recrystallization in modern shelf carbonates: evidence from pore water and solid phase chemistry. *Philosophical Transactions: Physical Sciences and Engineering*, pp.27-36.

Chapter 3

Ca isotope and trace metal incorporation in intergrown calcite and aragonite: insights from a thermogene travertine deposit

Abstract

This work presents results from isotopic and trace element analyses of solids and fluids from an active thermogene travertine ridge in the eastern Sierra of northern California. We sought to use this system to understand kinetic controls on trace element and isotopic partitioning behavior in terrestrial carbonates at above-ambient temperatures. This deposit forms via the emergence of hot (62-71°C), CO_2-rich fluids sourced from the dissolution of subsurface carbonates. As the source fluid equilibrates with atmospheric conditions, CO_2 degasses, promoting the formation of aragonite and calcite along a conduit with steadily changing temperature and pH. We find that partition coefficients of Sr in bulk carbonate ($K_{Sr} = (Sr/Ca)_{solid}/(Sr/Ca)_{fluid}$) are much greater (~50% higher) than expected based on experimental studies performed in the same temperature range, with values ranging from 0.5 to 1.25. However, these high partition coefficients may not be anomalous for travertine systems with high aragonite content and fast precipitation rates. In contrast, the Mg partition coefficients found in the travertines are anomalously high, even for travertines, but can potentially be explained by high rates of incorporation during very fast initial growth. Bulk solid Sr/Ca ratios and $\delta^{13}C$ measurements reveal a decreasing aragonite fraction in solids with distance from the source fluid, which is qualitatively consistent with results from X-ray diffraction data. Although the Sr/Ca and solid $\delta^{13}C$ data show marked differences as expected for decreasing aragonite fractions, Ca isotope fractionation ($\Delta^{44/40}Ca = \delta^{44/40}Ca_{solid} - \delta^{44/40}Ca_{fluid}$) between fluids and bulk solids shows little variation with proportion of aragonite. The roughly constant fractionation can be explained by relatively fast recrystallization of aragonite to calcite in the conduit walls. This work demonstrates the potential for applying Ca isotopes to understand mixed-polymorph carbonate systems, and is the first of its kind to report Ca isotope and trace element incorporation in thermogene travertines at these temperatures.

1. Introduction

Trace element (e.g., Sr, Mg, Mn) and metal isotope (e.g., δ^{44}Ca, δ^{26}Mg) incorporation into growing carbonates varies depending on the specifics of the surrounding growth environments. Their relative distribution between fluid and solid phases can fluctuate with growth rate, temperature, and salinity, among numerous other parameters. Because of their sensitivity to specific variables, these trace elements and isotopes can be used to probe surface exchange processes during crystal growth, as well as applied as proxies to interpret past growth conditions in geological materials. The fractionation of calcium isotopes between inorganic calcite and growth solution has been shown to have a relatively robust rate dependence (Tang et al., 2008a; Tang et al., 2012; AlKhatib and Eisenhauer, 2017a), which appears to be relatively invariant with Mg/Ca ratios less than one (cf. Chapter 4 of this dissertation) as well as with increased ionic strength (Tang et al., 2012). While there are few data on Ca isotope fractionation in inorganic aragonite (and none that are conclusive), some studies have shown that aragonite generally has a larger magnitude fractionation than calcite by approximately 0.6‰ (Gussone et al., 2005; AlKhatib and Eisenhauer, 2017b). In terms of trace element composition, partitioning of Sr into calcite is a rate-controlled phenomenon, analogous to Ca isotope fractionation (DePaolo, 2011). On the other hand, Sr and Mg in aragonite appear to be strongly controlled by temperature (Gaetani and Cohen, 2006; Kinsman and Holland, 1969) with little to no effect from growth rate. Mg partitioning into calcite, although generally increasing with temperature (Katz, 1973; Oomori et al., 1987, Lopez et al., 2009), is also seen to depend on solution composition (Mucci and Morse, 1983) and possibly also precipitation rate (Mavromatis et al., 2013).

While experimental studies are fundamental for isolating specific effects of solution conditions on carbonate growth, they fail to replicate the complexities of natural environments. Furthermore, laboratory experiments on carbonate growth are generally performed at much faster rates than occur in many natural systems (cf. Fantle and DePaolo, 2007). Perhaps unsurprisingly, the great majority of carbonate field studies focused on Ca isotope fractionation have focused on marine carbonates (e.g., Zhou and Mcdougall, 1998; Nägler et al., 2000; Gussone et al., 2004; Böhm et al., 2006; Fantle and DePaolo, 2007; Farkaš et al., 2007; Payne et al., 2010), with terrestrial Ca isotope studies falling far behind in number (e.g., Nielsen and DePaolo, 2013; Oehlerich et al., 2015). In order to bridge the divide between observations in slowly forming carbonate systems of the marine realm, for instance, and those in the laboratory, we have elected to study Ca isotope and trace metal incorporation in travertine-depositing hot springs. To date, there have been only two studies measuring Ca isotopes in travertine deposits (Tipper et al., 2006; Yan et al., 2016), and neither of these studies characterized Ca isotope fractionation in high-temperature (>60°C) travertine systems.

Travertines are composed of different carbonate minerals (Pentecost, 2005 and references therein), the great majority being calcite (e.g., Barnes, 1965; Usdowski et al., 1979; Herman et al., 1988; Jones and Renaut, 2008) and/or aragonite (e.g., Friedman, 1970), with less abundant occurrences of siderite (Amundson and Kelly, 1987) and in some cases, dolomite (Folk, 1994; Renaut and Jones, 1997). Unlike most marine carbonates, travertines are readily accessible, making them excellent candidates for field studies. Furthermore, they generally form much faster than the ultra-slow rates seen in some marine sedimentary environments (e.g., Fantle and DePaolo, 2007). There are many types of travertines, and consequently different mechanisms driving deposition, as summarized in Pentecost (2005). Degassing of CO_2 from carbonate-sourced groundwaters is the dominant driving mechanism of carbonate precipitation in thermogene travertines. CO_2 degassing increases fluid pH, driving fluids to become supersaturated with respect to various carbonate minerals. Travertine fissure ridges produced via this mechanism form in tectonically active areas across the globe (Pentecost, 2005), where local fracturing allows hot, CO_2-rich subsurface water to emerge.

In this study we characterize an active travertine fissure mound in the Eastern Sierra Nevada in Bridgeport, California. Because of predictable changes in pH and temperature down-conduit, this “field laboratory” allows us to isolate specific controls on trace element and isotope behavior during carbonate precipitation. Our aims are (1) to determine the magnitude of and controls on Ca isotope fractionation and trace element partitioning in thermogene travertines, (2) to use trace elements Sr and Mg, as well as C and Ca isotopes to probe the depositional and post-depositional reactions in terrestrial carbonates, and (3) to address complexities of understanding Ca isotope fractionation in multi-mineral carbonate deposits.

2. Methods

2.1 Sampling location and description

There are several travertine deposits located in Bridgeport, California (Travertine Hot Springs; 38°14’46.5” N, 119°12’17.8” W), some of which are actively precipitating from thermal CO_2-rich fluids. A NE-SW oriented fissure mound (Photo 1) is the focus of the current study. An active flow conduit measuring only centimeters in both depth and width (Photo 2) spans over 16 meters from inlet to the edge of the ridge, where the fluid terminates into several pools at the SW edge of the ridge. Although the flow conduit is relatively narrow and shallow, the section of active ridge is ~2.5 meters in height.

2.2 Flow path measurements

Rough estimates of the flow rate along the channel were obtained by floating a small (~1 cm diameter) piece of cork along overlapping sections of channel and recording time elapsed between beginning and end of the sections. Measurements from the inlet (0 meters) to ~2 meters could not be collected because of pebbles impeding the path of the cork. It was not possible to get timed trials along the entire conduit as pebbles impeded the path of the cork, and there were various eddies and turbulent patches causing the cork to get stuck on the side of the conduit. Flow rate estimates are averages of five trials from each section measured, multiplied by a correction factor of 0.65 (Govan, 1983). Channel depth and width were measured to nearest 0.25 cm. Channel depth was taken from the center of the conduit. Channel width was measured across the section of the conduit submerged in flowing water.

2.3 Fluid and solid collection

Both fluid and solid samples were collected beginning at the inlet (0 meters) at a spacing of 2 meters up to the terminus of the mound. Fluids for cation, anion, and alkalinity measurements were collected via syringe filtration through 0.2 μm Whatman filters. Samples collected for cation measurements were acidified with ~20 μL concentrated nitric acid. Fluids for $\delta^{13}C$ and dissolved inorganic carbon (DIC) analyses were collected with special attention paid to avoid interaction with atmosphere. These fluids were collected separately via filtration into syringes then transferred with needles into pre-evacuated serum bottles sealed with clamped rubber stoppers. Small (~10 cm^3) pieces of solid were chiseled from the edge of the flow conduit where there appeared to be the most recently precipitated carbonate.

2.4 Fluid analyses

Cation concentrations were determined using inductively coupled plasma optical emission spectroscopy (ICP-OES; Perkin Elmer 5300 DV optical emission ICP with auto sampler) for Ca, Mg, and Sr at the University of California Berkeley. Anion concentrations were determined using a Dionex ICS-2100 Ion Chromatography (IC) system (Thermo Scientific, USA) at Lawrence Berkeley National Laboratory. Total alkalinity was determined via Gran Titration. pH and temperature were measured in the field using a portable probe. $\delta^{13}C$ of DIC were measured with an Gilson auto-sampler connected to a Micromass JA Series Isoprime mass spectrometer at Lawrence Berkeley National Laboratory, reported relative to Vienna Pee Dee Belemnite (V-PDB) standard and fluid $\delta^{18}O$ measured using a Thermo Gas Bench II interfaced to a Thermo Delta V Plus mass spectrometer at the Center for Stable Isotope Biogeochemistry at the University of California Berkeley. Geochemical speciation calculations were performed using the computer program PhreeqC (Parkhurst and Appelo, 1999).

2.5 Geochemical, mineralogical, morphological characterization of solids

X-ray diffraction (XRD) measurements were collected using a PANalytical X'Pert Pro diffractometer with Co X-ray. Solid samples were rinsed with MilliQ water, dried, then digested with trace metal grade nitric acid and measured via ICP-OES (Perkin Elmer 5300 DV optical emission ICP with auto sampler). Carbon and oxygen isotopes in solids were measured with a GV IsoPrime mass spectrometer at the Center for Stable Isotope Biogeochemistry (University of California, Berkeley). Calcium isotope measurements ($\delta^{44/40}$Ca) were performed on a Thermo-Finnigan Triton Thermal Ionization Mass Spectrometer (TIMS) at the University of California Berkeley. Values of $\delta^{44/40}$Ca are reported in delta notation ($\delta_{sample} = 1000\times\left(\frac{R_{sample}}{R_{standard}} - 1\right)$; where R = ^{44}Ca/^{40}Ca) relative to bulk silicate Earth (BSE; ^{44}Ca/^{40}Ca = 0.0212035; Nielsen and DePaolo, 2013). Replicate measurements of the SRM 915A standard (^{44}Ca/^{40}Ca = 0.02118336) yielded a mean value of -1.05±0.05 (2 s.e., n = 20), with an average 2σ = 0.11. Details of sample preparation and measurement procedures can be found in the appendix of this dissertation. Ca isotope fractionation between solid and fluid phases is given by $\Delta^{44/40} = \delta^{44/40}\text{Ca}_{\text{solid}} - \delta^{44/40}\text{Ca}_{\text{fluid}}$.

Element maps (Ca, Mg, Sr, Mn) of solid samples were collected using electron probe microanalysis (EPMA) on a Cameca SX-100 electron microprobe at the University of California Davis. Samples were mounted under vacuum in 1-inch rounds of Epo-Tek 301-2 epoxy, then polished and coated with 25 nm of carbon. Maps were collected with wavelength-dispersive spectrometers (WDS) under 15kV beam voltage, raster length of 0.5μm/pixel with 750 ms dwell time. Singular quantitative point measurements were collected with 15kV beam voltage and 1μm beam diameter.

Glass slides (1 inch rounds) were left in the flowpath for 12-24 hours to precipitate fresh material and were subsequently imaged via scanning electron microscopy (SEM) at the University of California, Berkeley.

3. Results

The part of the fissure ridge at the Bridgeport travertines that is actively forming extends northeast-southwest, measuring roughly 18 meters in length and 2.5 meters high (Photo 1). From the inlet, hot fluid flows towards the southwest along a shallow crestal conduit with average dimensions of 4.5 cm across (Photo 2) by 3.5 cm deep. Flow rates are approximately 12-37 cm/s with variations associated with changes in conduit width, corresponding to discharge rates of approximately 29±20 L/min. New travertine forms a mm- to cm-scale lip-like overhang along the fluid-air interface of the conduit (Photo 2). White salts (likely carbonates and sulfates) can be observed on the slopes of the ridge, forming as a result of intermittent overflow perpendicular to the flow direction followed by evaporation. What appear to be green algae coat some subaqueous parts of the conduit, and red staining/coating can also be observed, predominantly on the floor of the conduit, with some staining also seen on the ridgetop (Photo 2).

Photo 1. Bridgeport fissure ridge. Arrow indicates southwest flow direction. Scale bar is approximately 2 meters.

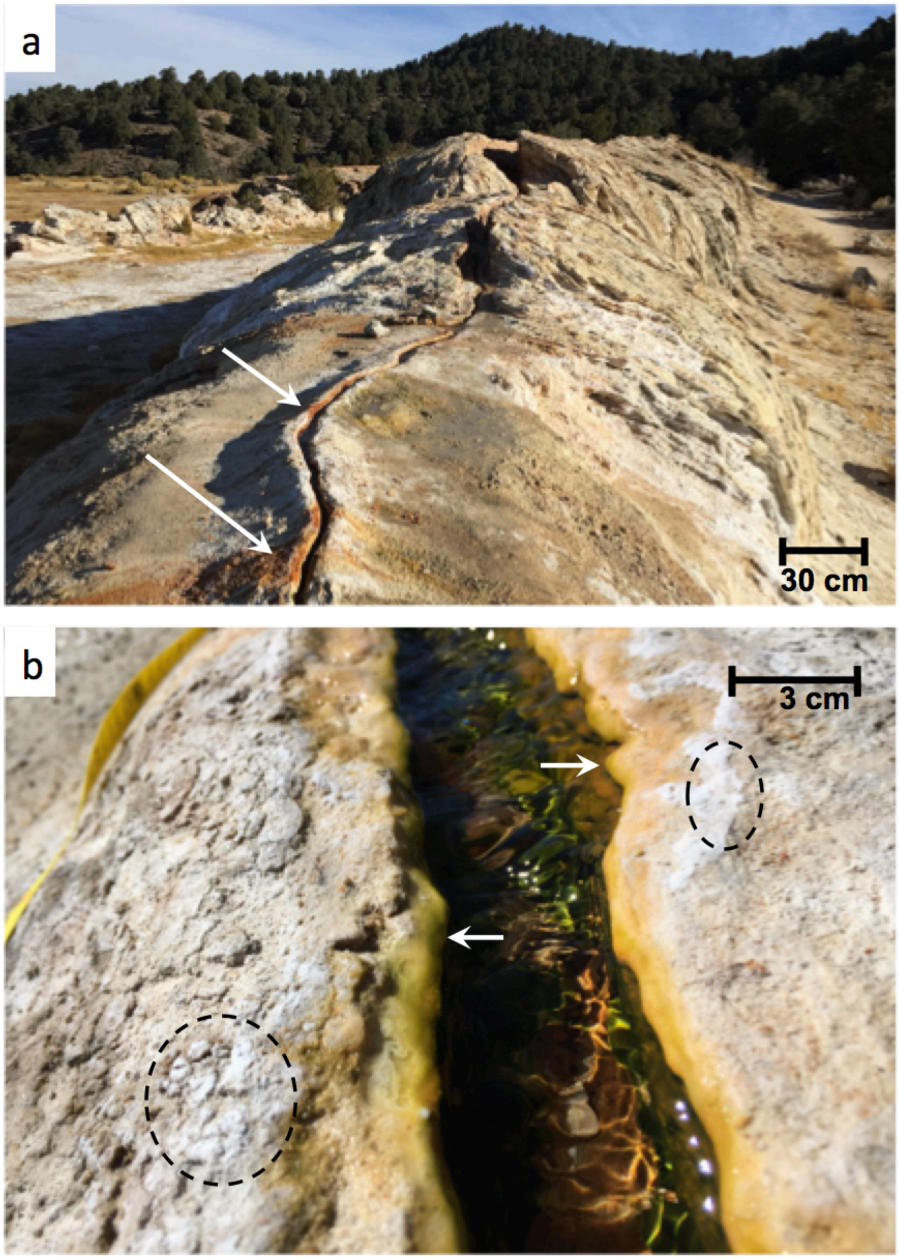

Photo 2. Bridgeport fissure ridge. (a) View looking up-conduit towards northeast, where active part of ridge connects with dormant sector. Large arrows indicate oxide staining on ridgetop. (b) Close-up view of crestal conduit. Small arrows in flowpath indicate lip-like overhang of newly precipitated carbonates. Circled regions denote salt residues. Red staining and green algae can be observed predominantly on floor of conduit.

Temperatures decrease monotonically from 71°C at the inlet to 62°C with a corresponding pH increase from 6.7 to 7.3 (Table 1). There are very minor and non-systematic fluctuations in most major element chemistry (Ca, Mg, Na, Cl) with distance from the inlet, and minimal decreases in Sr and DIC (Table 2). These observations are consistent with high flow rates overprinting indicators of carbonate precipitation, as well indicating little evaporation. Ca/CO_3 activity ratios decrease down-conduit (Table 1) by more than a factor of four, driven by an increase in pH. Calculated degrees of supersaturation of fluids with respect to calcite and aragonite (given as $\Omega = IAP/K_{sp}$; IAP = product of Ca and CO_3 activities and K_{sp} = solubility product of either calcite or aragonite) are given in Figure 1, both roughly tripling in magnitude over the length of the ridge.

Distance from inlet (m)	pH	T [(b)]	Depth [(c)]	width [(c)]	Ca/CO_3 [(d)]
0	6.70	71	4.5	8.0	38.3
2	6.76	70	3.0	3.0	32.5
4	6.85	69	3.5	6.5	27.6
6	6.91	68	4.0	3.0	20.4
8	6.95	66	3.0	2.5	23.2
10	7.01	66	3.5	4.0	22.6
12	7.05	66	4.0	4.5	20.0
14	7.15	65	5.0	6.5	14.3
16	7.29	62	2.0	2.5	8.6

Table 1. Fluid pH, temperature, channel dimensions, Ca/CO_3 activity ratio.
(b) Temperature ±1°C; (c) channel depth and width given in cm; (d) Ca/CO_3 activity ratios calculated using PHREEQC - LLNL database.

Distance from inlet (m)	Ca [(b)]	Mg [(c)]	Sr [(d)]	Na [(e)]	DIC [(f)]	SO_4[(g)]	Cl [(h)]
0	1.64	0.83	68.0	46.9	48.7	10.0	5.6
2	1.62	0.83	73.4	46.6	47.9	10.1	5.7
4	1.66	0.80	66.5	46.6	45.7	10.0	5.7
6	1.65	0.80	65.7	47.7	51.5	9.9	5.6
8	1.65	0.79	63.2	46.7	42.9	10.1	5.6
10	1.91	0.80	65.0	47.9	43.2	10.0	5.7
12	1.63	0.82	65.7	47.8	38	10.1	5.7
14	1.68	0.81	64.1	47.7	41.9	10.0	5.6
16	1.61	0.80	63.7	48.7	46.8	10.0	5.6

Table 2. Fluid chemistry: concentrations of major aqueous species.

(b) mM, 2σ ≤ 3%; (c) mM, 2σ ≤ 5.4%; (d) μM, 2σ ≤ 5%; (e) mM, 2σ ≤ 7.1%; (f) DIC = total dissolved inorganic carbon, mM, 2σ ≤ 5%; (g) mM, 2σ ≤ 4.9%; (h) mM, 2σ ≤ 5%.

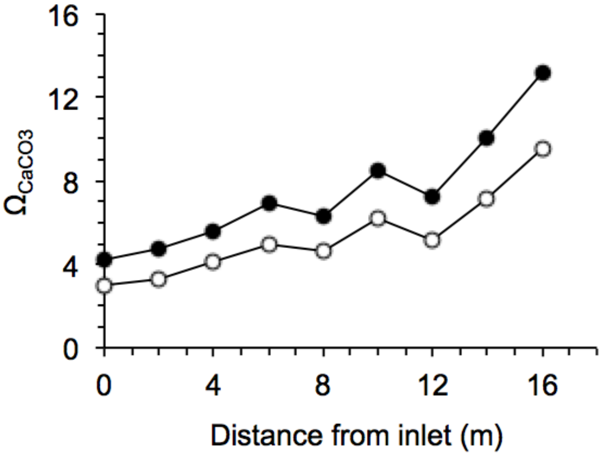

Figure 1. Fluid saturation state (Ω) with respect to calcite (filled circles) and aragonite (open circles).

Semi-quantitative XRD data (shown in Appendix) show both calcite and aragonite forming along the conduit in varying proportions. Aragonite dominates at the inlet, with increasing calcite fractions at increasing distance down-conduit. Peak shifts in XRD patterns from pure calcite indicate an increase in the mole fraction of $MgCO_3$ in calcite from ~6 mol% at the inlet to ~10 mol% at the end of the ridge.

Measurements of the bulk solid show decreasing ratios of Sr/Ca down-conduit (Table 3), consistent with a decreasing aragonite content with distance from the inlet. Aragonite and calcite are the only mineral phases detectable with XRD as well as the only phases observed during microprobe imaging, based on crystal morphology. Electron microprobe images (Fig. 2) show inter-grown calcite and aragonite with great morphological variability. Morphology of these minerals varies among growth layers, although no systematic changes could be detected. Aragonite is found as single acicular needles ranging in length from 5-250 μm as well as in radiating or dendritic clusters, with one observed occurrence of pseudohexagonal crystals, roughly 5-10 μm in diameter, in one sample collected 10 meters from the inlet. Calcite morphology is similarly diverse, including massive, euhedral, blocky, prismatic and feathery mineral habits. Individual calcite crystals also fall into a size range of ~5-250 μm.

Distance from inlet (m)	**Bulk solid Mg/Ca(a)**	**Bulk solid Sr/Ca (b)**	**Fluid Mg/Ca (c)**	**Fluid Sr/Ca (d)**	**Bulk K_{Sr} (e)**	**Bulk K_{Mg} (f)**
0	0.032	0.052	0.504	0.041	1.250	0.064
2	0.024	0.049	0.511	0.045	1.080	0.046

4	0.092	0.043	0.485	0.040	1.065	0.190
6	0.075	0.024	0.487	0.040	0.609	0.153
8	0.076	0.042	0.481	0.038	1.091	0.158
10	0.036	0.026	0.420	0.034	0.778	0.086
12	0.092	0.031	0.502	0.040	0.772	0.183
14	0.063	0.027	0.485	0.038	0.705	0.130
16	0.051	0.023	0.499	0.040	0.584	0.103

Table 3. Bulk solid and fluid Mg/Ca and Sr/Ca molar ratios.
(a) mol Mg/mol Ca, 2σ ≤ 5%; (b) mol Sr/mol Ca, 2σ ≤ 5%; (c) mol Mg/mol Ca, 2σ ≤ 6.2%; (d) mol Sr/mol Ca, 2σ ≤ 5.8%; (e) 2σ ≤ 7.8%; (f) 2σ ≤ 8.2%.

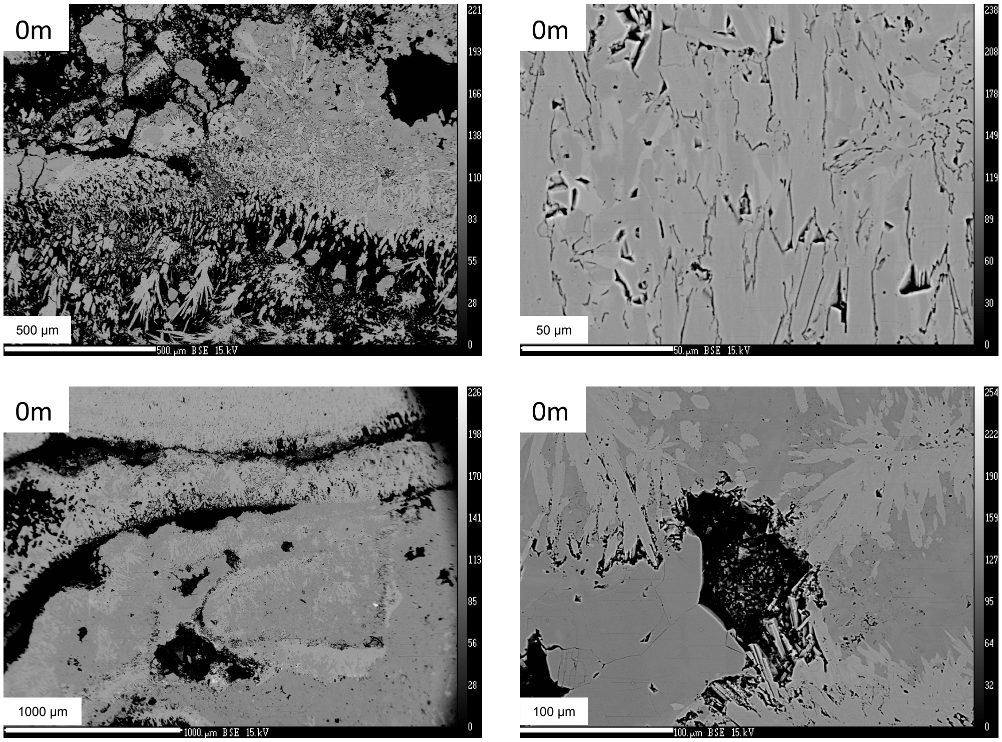

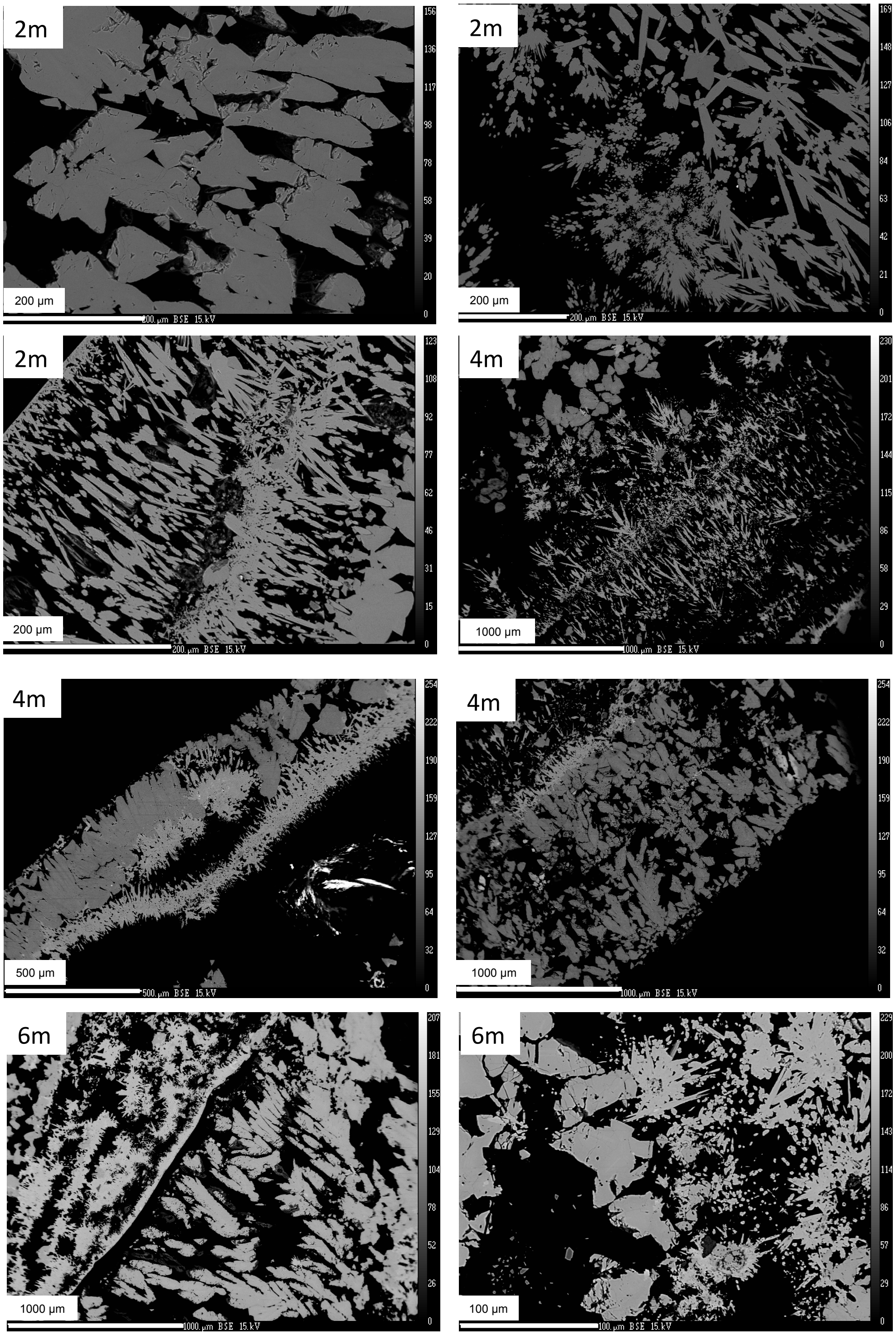
2m
200 µm
2m
200 µm
2m
200 µm
4m
1000 µm
4m
500 µm
4m
1000 µm
6m
1000 µm
6m
100 µm

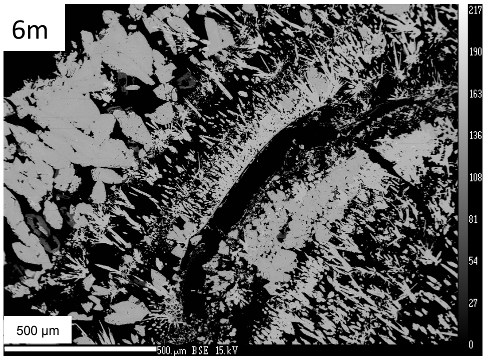
6m
500 μm
500.μm BSE 15.kV
217 190 163 136 108 81 54 27 0

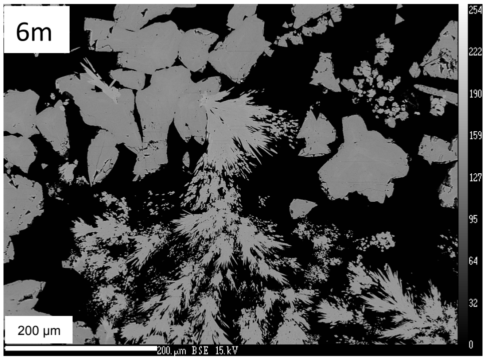
6m
200 μm
200.μm BSE 15.kV
254 222 190 159 127 95 64 32 0

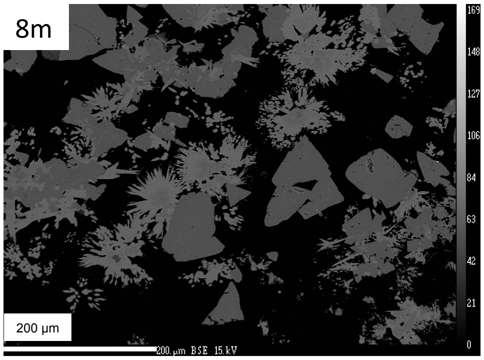
8m
200 μm
200.μm BSE 15.kV
169 148 127 106 84 63 42 21 0

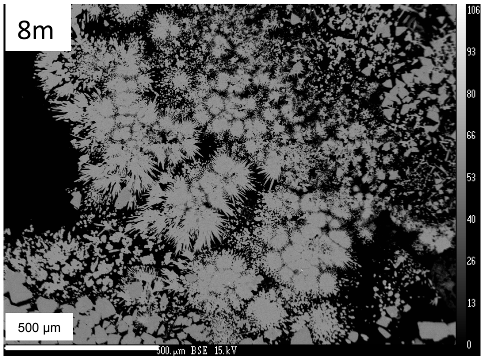
8m
500 μm
500.μm BSE 15.kV
106 93 80 66 53 40 26 13 0

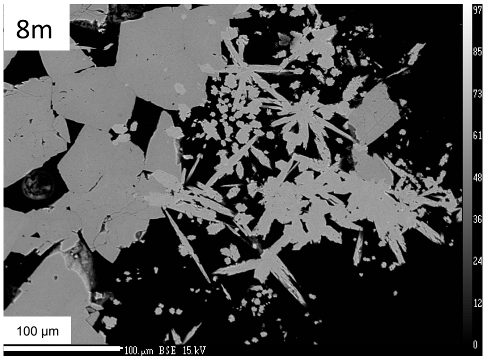
8m
100 μm
100.μm BSE 15.kV
97 85 73 61 48 36 24 12 0

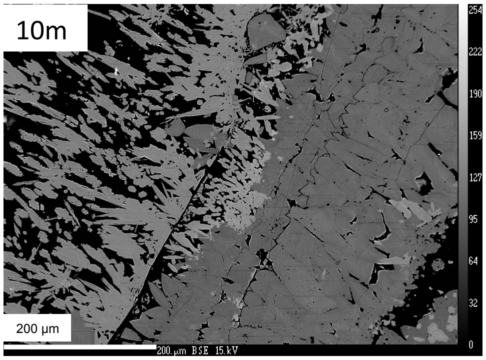
10m
200 μm
200.μm BSE 15.kV
254 222 190 159 127 95 64 32 0

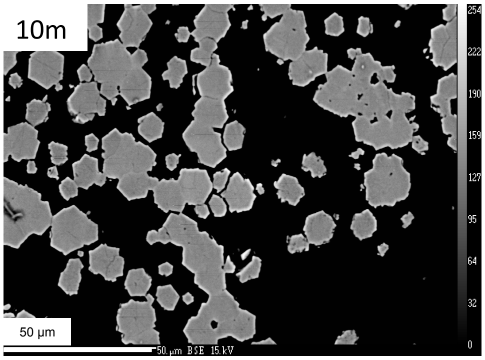
10m
50 μm
50.μm BSE 15.kV
254 222 190 159 127 95 64 32 0

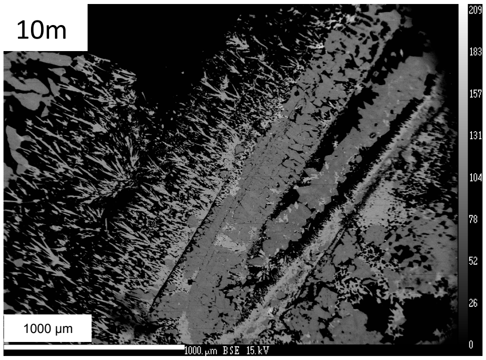
10m
1000 μm
1000.μm BSE 15.kV
209 183 157 131 104 78 52 26 0

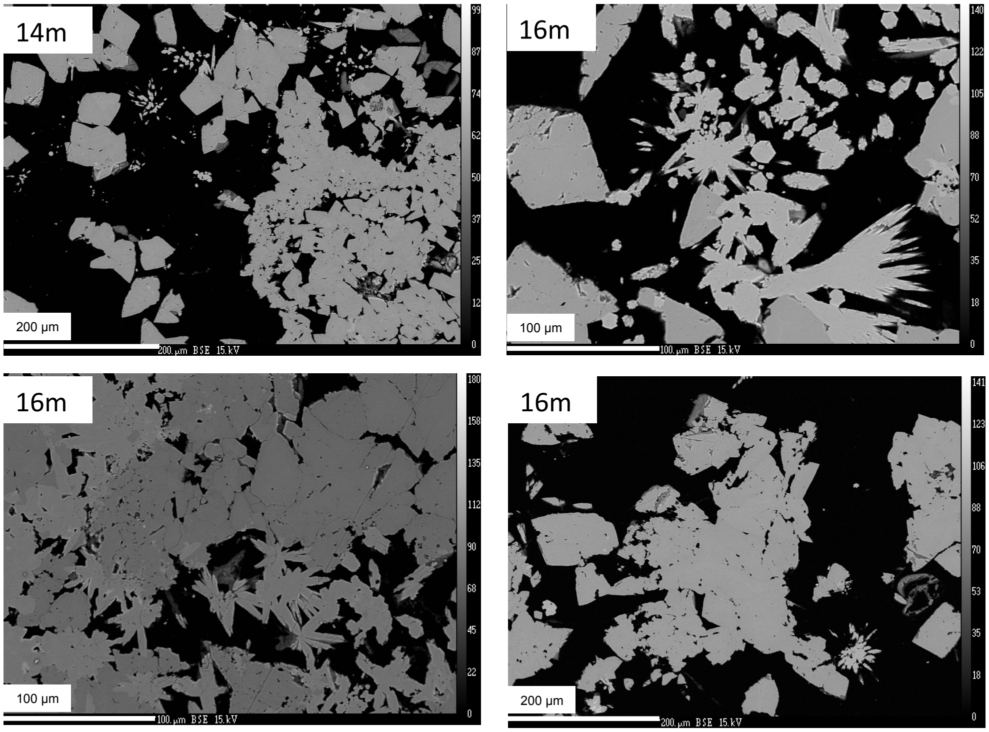

Figure 2. Selected EPMA images.

Although XRD data indicate that calcite and aragonite are the only dominant phases, it is possible other minerals are found in quantities <5% (v/v), the detection limit of the diffractometer. The fluid is supersaturated with respect to strontianite ($SrCO_3$) and various Fe-oxides as well as amorphous carbonates containing Mg and Sr. However, none of these minerals were seen in the microprobe images, and amorphous phases are relatively unstable, especially while in contact with calcite and aragonite surfaces. Solid Sr/Ca ratios fall into a narrow range (0.02-0.05), much lower than would be seen in strontianite, eliminating the possibility that it was morphologically mistaken for the calcite or aragonite. This suggests that either these phases are not present, they are present at spatial scales less than 1-2 µm (e.g., as thin coatings on calcite and aragonite) or are concentrated in regions not sampled on the microprobe.

Although the bulk solid is a mixture of aragonite and calcite, the bulk fluid and solid measurements of elemental ratios (Table 3) can be used to provide estimates of partition coefficients K_d for Mg and Sr (Fig. 3 and Table 3). Bulk K_d calculations for Sr show systematically decreasing values from 1.25 to 0.5 along the conduit, while no trend is observed for K_{Mg}, which varies from 0.04 to 0.19.

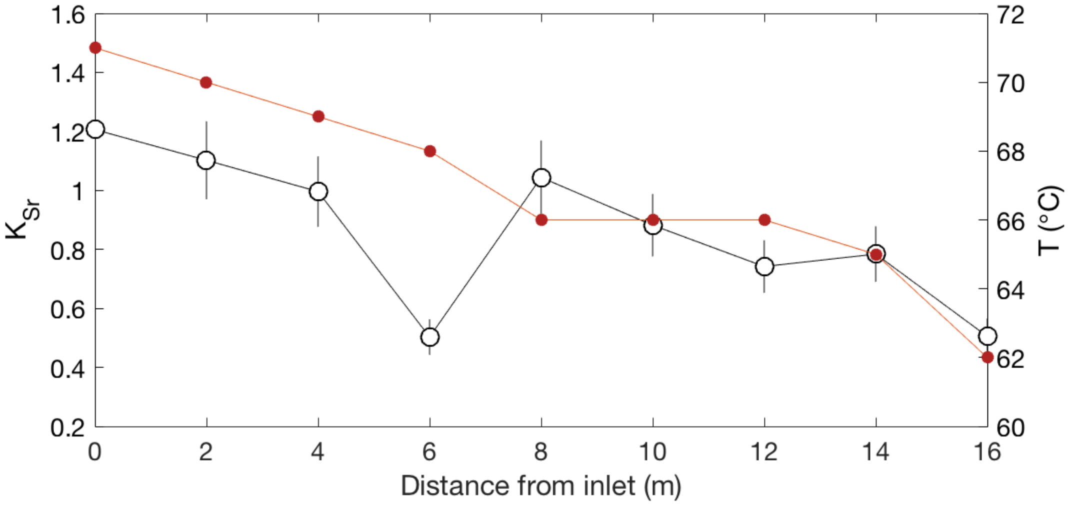

Figure 3. Bulk K_{Sr} values $[(Sr/Ca)_{solid}/(Sr/Ca)_{fluid}]$ shown with temperature as a function of distance from the inlet.

Electron microprobe element mapping shows that Sr is dominantly found in aragonite, while Mg is concentrated in calcite (Fig. 4). The Sr content appears to be fairly uniform across morphologies and within individual crystals. The Mg content seen in solids is variable: some crystals have homogeneously distributed Mg, while others (Fig. 4) have visible zoning.

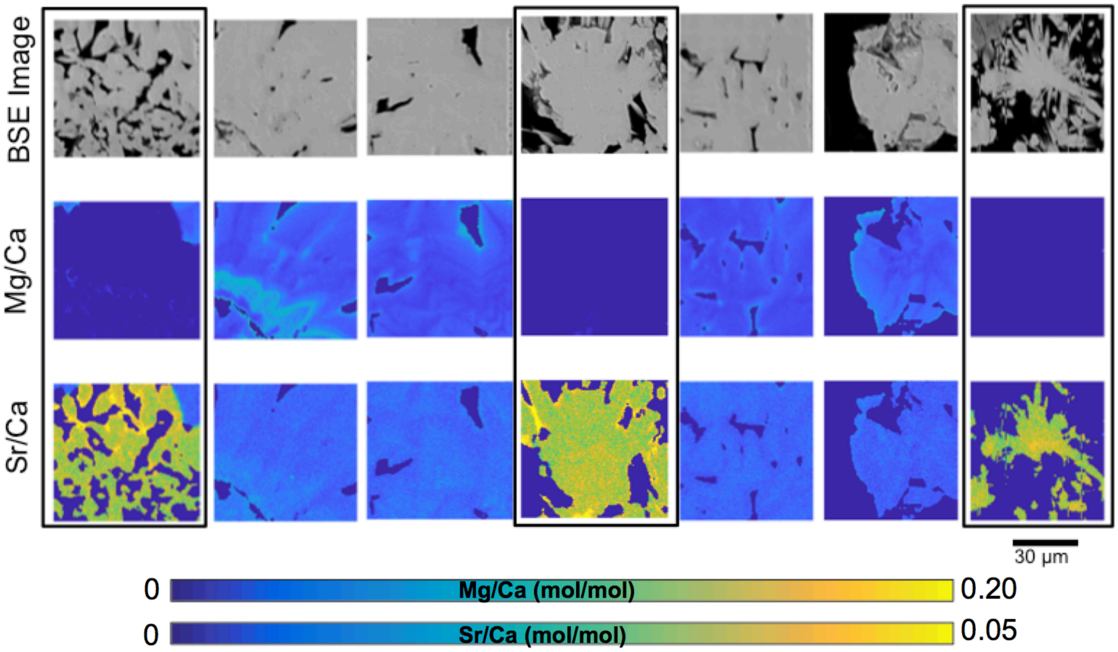

Figure 4. Element ratio maps of selected samples. Aragonite outlined in boxes. Not outlined are calcite.

Carbon isotopes measured in fluids (Fig. 5) are lightest at the inlet (-2.1‰ V-PDB), increasing to an average value of -1.6‰ by 4 meters down-conduit. Carbon isotopes measured in bulk solids (Fig. 5) show the opposite behavior, decreasing from ~0.2‰ at the inlet to ~0.6‰ at the end of the ridge. The isotopic fractionation between solids and fluids (Fig. 6) becomes smaller with increasing distance from the inlet. Oxygen isotopes measured in bulk solids and fluids (Fig. 7) show little variation along the conduit, averaging -24.11±1.26 (2σ; V-PDB) and -16.25±0.13 (2σ; V-SMOW), respectively, and are consistent with values from travertines formed in Yellowstone (Fouke et al., 2000) at similarly high temperatures. Two solid samples (at 6 and 12 meters) show anomalously high values in both $\delta^{13}C$ and $\delta^{18}O$ (Fig. 5, Fig. 7). Bulk solid Sr/Ca plotted against solid $\delta^{13}C$ are positively correlated (R^2 = 0.68), excluding the anomalously high $\delta^{13}C$ values at 6 and 12 meters (Fig. 5).

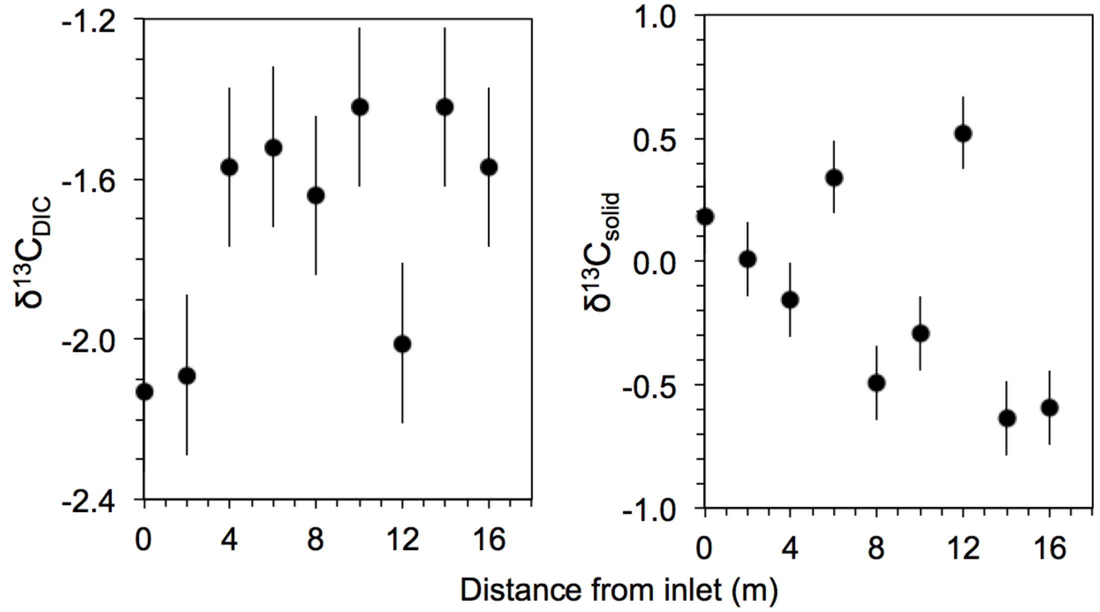

Figure 5. $\delta^{13}C$ of solids and dissolved inorganic carbon.

The positive correlation between Sr/Ca ratios and $\delta^{13}C$ in bulk solids (Fig. 8), both of which are decreasing downstream, supports the semi-quantitative XRD data that show decreasing aragonite and increasing calcite with distance from the inlet. On average, $\delta^{13}C$ fractionation between inorganic calcite and DIC ($\delta^{13}C_{cal}$ - $\delta^{13}C_{DIC}$) is 0.9 ± 0.2‰, and that of aragonite ($\delta^{13}C_{arag}$ - $\delta^{13}C_{DIC}$) is 2.7 ± 0.2‰ (Rubinson and Clayton, 1969; Romanek et al., 1992). This fractionation is independent of rate, and largely insensitive of temperature, with an estimated dependence of 0.035‰ per °C (Saltzmann and Thomas, 2012). Accordingly, the fractionation between bulk carbonate and DIC ($\delta^{13}C_{carb}$ - $\delta^{13}C_{DIC}$), as shown in Figure 6, is a useful proxy for determining relative fractions of calcite and aragonite.

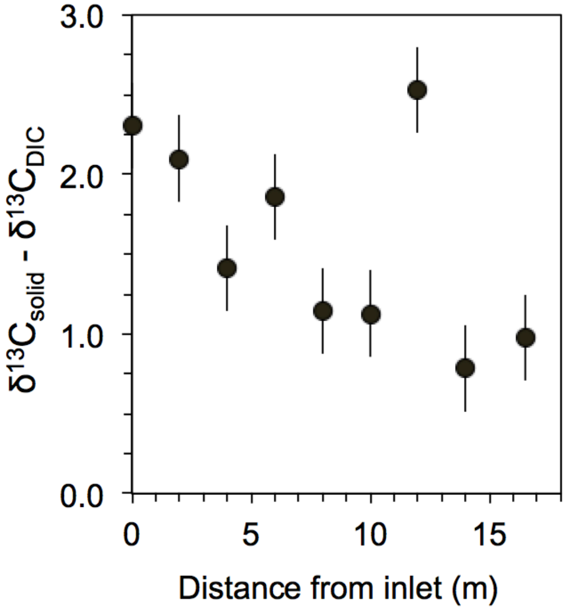

Figure 6. δ^{13}C fractionation between solids and fluid.

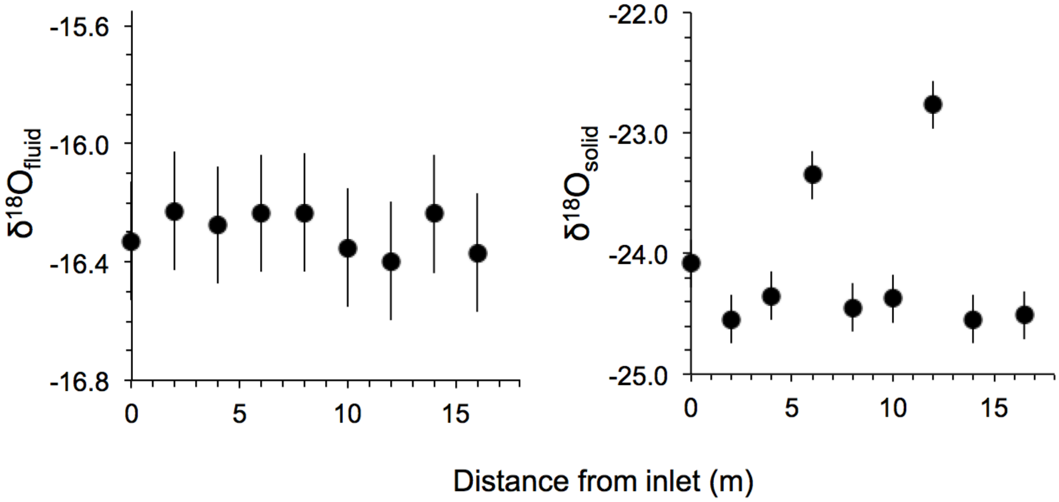

Figure 7. δ^{18}O of fluids and solids.

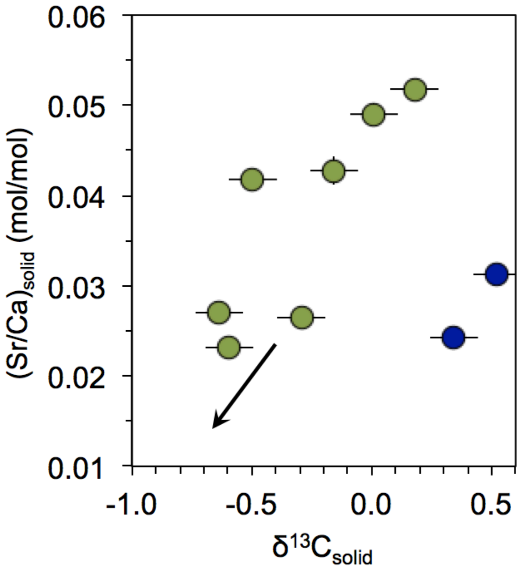

Figure 8. Solid δ^{13}C versus Sr/Ca. Arrow indicates downstream direction. Blue points are outliers in both δ^{13}C and δ^{18}O solid data.

Calcium isotopes (δ^{44}Ca) measured in fluids and solids have very small fluctuations overall (Fig. 9), and do not show any appreciable trends down-conduit. The Ca isotope composition of fluids averages -0.29 ± 0.12‰ (2 s.d.m.), and that of the solids averages -0.77 ± 0.23‰ (2 s.d.m.). The mean Ca isotope fractionation between solids and fluids, $\Delta_{s\text{-}f}$, is -0.48 ± 0.28‰ (2 s.d.m.), again has no apparent downstream trend (Fig. 9).

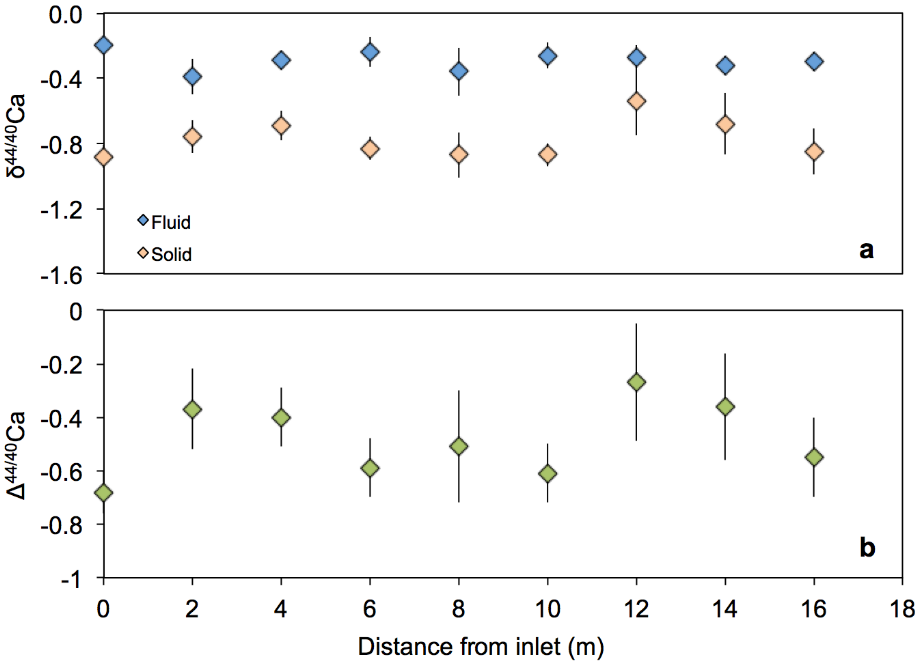

Figure 9. Ca isotope data: (a) fluid and solid δ^{44}Ca and (b) Ca isotope fractionation between solids and fluids ($\Delta^{44/40}$Ca).

Scanning electron microscope backscattered diffraction (SEM-BSE) images of material precipitated on glass slides shows both calcite and aragonite (Fig. 10). Calcite morphology includes sub-regular rhombs as well as the beginnings of feathery calcite nucleating on the rhomb surfaces. Aragonite formed on the growth slides in bundles of acicular needles, sometimes referred to as "dumbbell" morphology. Not enough carbonate precipitated on the slides to carry out further analyses, but the images of calcite can be used to make a rough estimate of growth rate under current conditions. Assuming a density of 2.71 g/cm^3 and approximating surface area based on rhombohedral geometry, we estimate surface-normalized growth rates of roughly 6×10^{-6} mol/m^2/s. From this growth rate we estimate that the mound could be as young as 10 ky old.

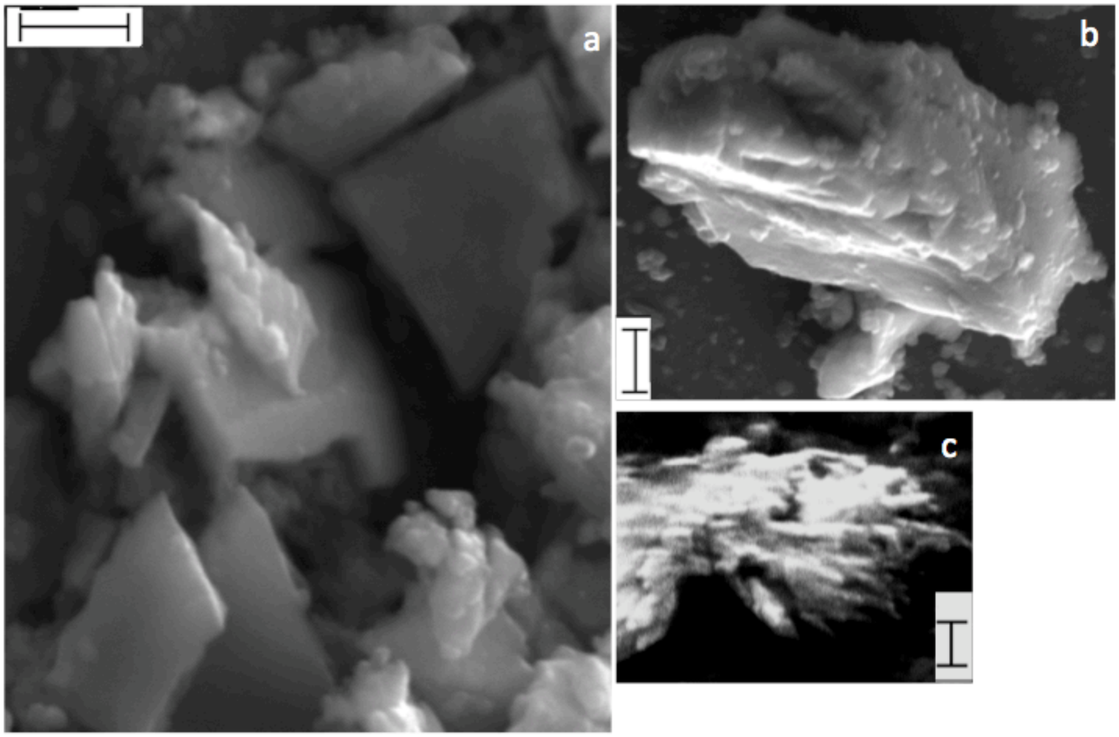

Figure 10. Selected SEM-BSE images of calcite (a,b) and aragonite (c) grown on glass slides in flowpath. Scale bars in (a) and (b) are 2µm and 1µm in (c).

One of the challenges in understanding the solid-fluid interactions in this system lies in the difficulty of knowing how well the present-day fluids represent fluids from which the bulk travertine solids formed. A means of circumventing use of existing solids is to precipitate fresh solids from active fluids, thereby clearly capturing and matching fluid signals to associated precipitates. This method has been utilized previously (e.g., Amundson and Kelly, 1987) and can be informative. However, there are shortcomings as well as challenges associated with this approach. One potential issue is that precipitating fresh carbonate on a foreign substrate – be it tape (Amundson and Kelly, 1987), Icelandic spar (Plummer et al., 2000), glass slides, or another surface – means that the nucleation and growth dynamics will necessarily be different than those that are occurring in that location. There are several possible implications of nucleation and growth on different substrates, including how trace elements are incorporated and determination of precipitate polymorph, as well as how the substrate is positioned in the flowpath and alters local fluid dynamics. The logistical challenge we faced was not being able to grow sufficient material on the slides to perform the many analyses required for a comprehensive study.

Fortunately, because of past studies of this locality, we were able to obtain some constraints on earlier geochemical and hydrodynamic conditions, which is unlike many other studies in the literature. A study of hydrothermal systems in the western United States and other localities (Mariner et al., 1977) provides select geochemical data of the inlet fluid at Bridgeport (Table 4) from over four decades ago. All measured parameters from this study are within 15% of the values reported in 1977, with ten of the thirteen within 5%, demonstrating that the fluid chemistry today provides a reasonable approximation of the fluid chemistry and growth conditions under which the solid samples formed. Semi-quantitative electron microprobe maps of elemental ratios Sr/Ca and Mg/Ca can also speak to the constancy of growth conditions in relation to the calcite and aragonite growth rates. Zonation/banding of Mg/Ca in calcite suggests fluctuations in the growth fluid affecting Mg uptake on timescales of crystal growth (Fig. 4). In contrast, the lack of zoning in Sr/Ca suggests both constant fluid Sr/Ca and uniform growth conditions on timescales of crystal growth. Although these constraints have uncertainty associated with them, they do provide reasonable estimates of how fluids have changed with time.

Parameter	This study	Mariner et al., 1977
T(°C)	69	71
pH	6.7	6.7
SiO_2 (aq)	1.66	1.44
Ca	1.6	1.64
Mg	0.74	0.66
Na	47.85	47
K	1.41	1.46
Li	0.36	0.37
Alk (as HCO_3)	29.5	32.8
SO_4	9.58	10.03
Cl	5.64	5.64
F	0.24	0.24
B	0.92	0.91

Table 4. Fluid chemistry at inlet comparing results from this study to measurements collected in 1977. Concentrations given in mM unless otherwise noted.

4. Discussion

In Part 1 of this discussion, we develop a conceptual framework of travertine deposition at this site. Here we broadly address controls on carbonate precipitation, discuss why biology likely does not play a strong role in the Bridgeport deposits, and consider explanations for the complex mineralogy observed. In Part 2, we interpret trace element and Ca isotope data from carbonates and fluids, as well as propose a more nuanced model of travertine deposition and alteration.

4.1 Site interpretation

4.1.1 CO_2 degassing

In general, little variation in fluid chemistry is seen in these samples due to the fast flow rate relative to the rate at which various reactions are occurring. However, one reaction that outpaces flow rate is CO_2 degassing (Fig. 11), which can be seen in the pH (Table 1), and DIC (Table 2) data, as well as somewhat in the fluid carbon isotope data (Fig. 5), although the signal is a bit more convoluted. Based on speciation calculations, we determined that P_{CO2} follows a weakly exponential decrease from the inlet to the edge of the ridge. This is consistent with CO_2-rich fluids coming to the surface and approaching equilibrium with the atmosphere. The change in P_{CO2} over the conduit is approximately 0.6 atm, corresponding to a rate of -0.009 atm/s using an average flow rate of 0.25 m/s. Our P_{CO2} values are similar to, although lower than, those reported by Amundson and Kelly (1987), who studied CO_2-rich thermogene deposits along the California Coast Range. They observed a decrease from P_{CO2} of 1.19 to 0.01 atm over 13 meters at an estimated discharge of 60 L/min. Amundson and Kelly (1987) do not provide channel dimensions, but if we assume a conduit cross-sectional area of 0.005 m^2, this corresponds to a degassing rate of -0.016 atm/s.

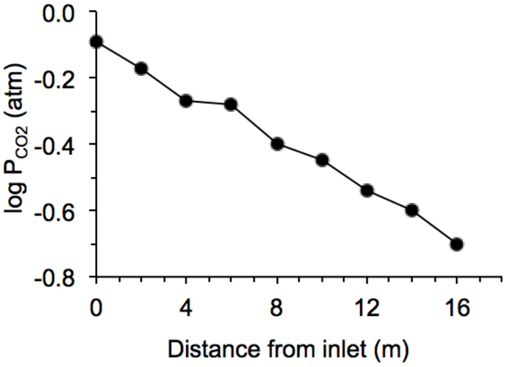

Figure 11. Decreasing P_{CO2} as a function of distance from inlet.

As ^{12}C is preferentially removed while the fluid evolves towards equilibrium with atmospheric CO_2, the resultant fluid becomes isotopically heavier, as seen commonly in other travertine studies (Kele et al., 2008; Amundson and Kelly, 1987). While measured $\delta^{13}C_{DIC}$ in the Bridgeport fluids do not correlate perfectly with the degassing rate, there is a clear trend of increasing $\delta^{13}C_{DIC}$ with distance from the source (Fig. 5). This co-variation indicates that fluid $\delta^{13}C$ is predominantly controlled by CO_2 degassing, rather than any biological or mineralogical effects.

4.1.2 Calcite-aragonite polymorphism and morphology

One interesting and complex aspect of travertine formation lies in the great variety of minerals formed, sometimes across seemingly similar environments. Based on field and experimental studies, it was previously thought that the dominant controls on calcite-aragonite polymorphism were fluid Mg/Ca ratios and temperature (Folk, 1994 and references therein; Morse et al., 1997). Based on these observations, aragonite rather than calcite was expected to form at Mg/Ca solution ratios greater than one, as well as at temperatures above approximately 40°C, regardless of Mg/Ca ratio. However, some studies of natural travertine deposits (e.g., Guo and Riding, 1992; Renaut and Jones, 1997; Jones and Peng, 2016) noted that both calcite and aragonite formed at temperatures and/or Mg/Ca ratios in regimes thought to be exclusively calcite or aragonite.

Although the Mg/Ca ratios in the Bridgeport fluids fall below this threshold of one, the temperature is greater than 60°C for the entire flowpath, which means only aragonite is expected to precipitate. However, as seen in the XRD data (see Appendix) as well as EPMA maps (Fig. 4) and images (Fig. 2), both calcite and aragonite exist along the conduit. While recrystallization of aragonite to calcite is likely occurring (see Section 4.2), it is possible that it is not the only reason calcite is present. The stability of a considerable fraction of aragonite along the entire length of the conduit as observed in EPMA images (Fig. 2) conflicts with extensive recrystallization. Down-conduit trends in Sr/Ca (Fig. 3) and $\delta^{13}C$ (Fig. 5,6) indicate decreasing aragonite content, which is consistent with a temperature control on polymorphism. Yet, temperature is clearly not the only determinant. While the relative *fractions* of aragonite and calcite change predictably with temperature down-conduit, polymorph morphology does not vary in any systematic way within micro-layers, as observed in EPMA images (Fig. 2).

The growth of both calcite and aragonite on *in situ* glass slides (Fig. 10) argues against a surface templating control on polymorph selection. If aragonite had recrystallized to calcite at the fluid-travertine interface, for instance, the presence of a calcite substrate could promote the subsequent growth of calcite. However, if this mechanism controlled calcite precipitation in an aragonite-dominant temperature regime, then calcite would not nucleate on glass slides. Alternatively, variations in fluid chemistry causing kinetic inhibition of aragonite in some places seem implausible at the spatial scale of calcite-aragonite distribution. Alternative proposed controls for the co-precipitation of calcite and aragonite included rates of CO_2 degassing (Jones and Peng, 2016; Renaut and Jones, 1997), and organisms acting as biological nuclei for specific phases (e.g., Guo and Riding, 1992). We can rule out biology as a sole determinant of polymorph, as we were able to precipitate both calcite and aragonite on glass slides. Jones and Peng (2016) and Renaut and Jones (1997) also argue that small-scale variability in fluid agitation can change the CO_2 degassing rate as well as impact polymorphism. This could be a plausible explanation for the intercalated calcite and aragonite observed, but it is not clear what mechanism links changes in polymorphism to degree or nature of fluid agitation.

An experimental study by Choudens-Sánchez and González (2009) demonstrated that the degree of calcite supersaturation and fluid Mg/Ca ratio can explain the coexistence of aragonite and calcite seen in natural samples. While Mg strongly inhibits calcite growth, it does not affect aragonite precipitation rates. Consequently, in the Bridgeport system, this kinetic effect is not expected to change significantly down-conduit, as the Mg/Ca fluid ratios vary minimally. However, the degree of calcite supersaturation increases at a faster rate than that of aragonite with distance from the inlet (Fig. 1), causing the system to move farther away from an aragonite-dominated regime (Choudens-Sánchez and González, 2009).

While these findings can account for the downstream trends in dominant polymorphism, they cannot explain the alternating micro-layers of aragonite and calcite observed in microprobe images (Fig. 2). It is possible that templating is not the main control on polymorph selection, but rather a second order effect that can account for the micro-layering observed. Experimental studies testing the effects of substrate within the regimes identified by Choudens-Sánchez and González (2009) could verify this hypothesis.

4.1.3 The role of biology

In many travertine systems, biology plays a dominant role in mediating carbonate precipitation, both serving as physical nuclei onto which carbonate can nucleate, and altering fluid chemistry (e.g., Buczynski and Chafetz, 1991; Fouke et al., 2000). To determine dominant controls on carbonate precipitation, it is important to assess the role of both macro- and microorganisms. In the Bridgeport hot springs, there is no apparent biological influence on precipitation based on the evidence from fluid data, morphology, or photomicrographs.

Photosynthetic activity causes preferential consumption of ^{12}C in growth media, leaving the residual fluid with heavier $\delta^{13}C$ that then becomes incorporated into solid phases. In a study of thermogene travertines from Iran, Zarasvandi et al. (2017) observe travertine $\delta^{13}C$ values ranging from +1.5 to +11.7, which they partially attribute to this mechanism. However, CO_2 degassing and aragonite precipitation impart a similar distillation to the fluid, so other methods are needed to distinguish the specific role of biology. Other potentially useful indicators of biologic metabolisms include redox-sensitive species such as sulfate. A common metabolism in high-sulfate systems such as this one is sulfate reduction, which generates hydrogen sulfide as an odorous byproduct. In addition to a constant sulfate concentration down-conduit, no such odor was detected in proximity to the fluids on the ridge like that observed in Kele et al. (2008) and other studies. However, in colder, stagnant pools west of the ridge there is evidence of bisulfide production.

In some travertines, there are biological artifacts in the carbonates including holes, hollowed out features indicating the former presence of biological nuclei (Guo and Riding, 1992; Kele et al., 2008), calcified bubbles (Guo and Riding, 1992; Fouke et al., 2000; Kele et al., 2008), and in some cases, the presence of diatom frustules (Chafetz et al., 1991; Zarasvandi et al., 2017). None of these features are observed in the samples from this study. The morphologies observed in the Bridgeport travertines also appear quite distinct from the more rounded features noted in biologically-mediated carbonates (e.g., Buczynski and Chafetz, 1991; Kele et al., 2008). Additionally, the often undulating, dome-like micro- and macroscale layering and terraces seen in stromatolite carbonates (cf. Riding, 2011) are absent along the Bridgeport conduit.

4.2 Isotopes and trace elements in carbonates

4.2.1 Trace element partitioning

4.2.1.1 Strontium partitioning, K_{Sr}

Bulk partition coefficients, K, are given by $(M/Ca)_{solid}/(M/Ca)_{fluid}$ where M is the substituting element. Overall, the measured bulk K_{Sr} values (0.5-1.2) are considerably higher than literature values for both calcite and aragonite. Experimental data show that pure aragonite has a K_{Sr} ranging from 0.98 and 0.85 between 60 to 80°C (Gaetani and Cohen, 2006; Kinsman and Holland, 1969). Sr partitioning in aragonite increases with decreasing temperature (e.g., Gaetani and Cohen, 2006; Kinsman and Holland, 1969), while K_{Sr} of calcite increases with precipitation rate (Lorens, 1981; Tesoriero and Pankow, 1996; Gabitov and Watson, 2006; Tang et al., 2008; Gebrehiwet et al., 2012; Gabitov et al., 2014). For calcite, the highest K_{Sr} reported from experiments is approximately 0.4, although most values fall closer to 0.1 (cf. Gabitov et al., 2014).

K_{Sr} values for calcite and aragonite are expected to differ greatly due to the difference in crystal structure between the two phases. With relatively small changes in fluid Sr/Ca, the trend towards lower bulk K_{Sr} values can be explained by an increasing calcite fraction in the bulk solid. A second-order temperature effect on bulk K_{Sr} can be explained by an aragonite K_{Sr} temperature dependence. There are not sufficient constraints on the end-member distribution coefficients to rigorously calculate fractions of each polymorph. However, we can approximate fractions of aragonite and calcite if we assume values for their distribution coefficients, given a mass balance approach where

$K_{Sr(bulk)} = f_A * K_{Sr(A)} + f_C * K_{Sr(C)}$ (f = polymorph fraction; C = calcite; A = aragonite). For this exercise, given the very high bulk K_{Sr} values, we assume (1) that all solid at the inlet is aragonite (and therefore $K_{Sr(A)} = 1.2$), and (2), that calcite is precipitating close to its kinetic end-member $K_{Sr(C)} = 0.4$. Following the temperature dependence given by Gaetani and Cohen (2006), K_{Sr} for aragonite will increase down-conduit at a rate of 0.0062 per °C. Given these constraints, we estimate aragonite fractions decreasing from 1 to 0.12. Alternatively, given a more slowly precipitating calcite with a $K_{Sr(C)}$ of 0.1 results in a range of aragonite fractions from 1 to 0.35.

Because the bulk distribution coefficient is a mixture between that of calcite and aragonite, and because calcite is present in fractions greater than 5% in all samples, the *pure aragonite* K_{Sr} will be even higher than the bulk K_{Sr} at the inlet. In other words, at >70°C, the K_{Sr} of aragonite could be larger than 1.2, which is approximately 50% larger than the value predicted by Gaetani and Cohen (2006) and Kinsman and Holland (1969). However, these bulk Sr partition coefficients and inferred K_{Sr} values may not be anomalous for thermogene travertine systems.

Kele et al. (2008) studied an active thermogene travertine deposit in northern Hungary composed dominantly of calcite and aragonite, formed from waters between 41-67°C within a pH range of 6.4-7.7. Although there are several other localities that are somewhat comparable to the Bridgeport travertines, none (to the best of our knowledge) report Sr/Ca in both solid and fluids as well as calcite and aragonite fractions. Although Kele et al. (2008) did not report K_{Sr} values, they are easily calculated from the solid and fluid Sr/Ca ratios. At temperatures between 45-67°C, their K_{Sr} values are strongly correlated to aragonite fraction via the linear relation $K_{Sr} = 1.248*f_A + 0.150$ ($R^2 = 0.947$). This indicates that the calcite end-member has an average K_{Sr} equal to 0.15, and extrapolating to $f_A = 1$ predicts a $K_{Sr(A)}$ of 1.40. Although there is a temperature dependence to $K_{Sr(A)}$ as previously discussed, the result of changing temperature by 20°C will shift $K_{Sr(A)}$ by only ~0.12, which is small in comparison to the effect of mineralogy. Assuming a $K_{Sr(A)}$ of 1.40 ± 0.06 at 56°C (the intermediate value of the Kele et al. temperatures) for the Bridgeport travertines would change our end-member $K_{Sr(A)}$ estimate to approximately 1.3. Accordingly, our estimates of aragonite fractions change to 0.90 to 0.11 and 0.92 to 0.32, depending on whether a $K_{Sr(C)}$ of 0.4 or 0.1 is used.

As expected based on experiments, the data from Kele et al. (2008) demonstrate a $K_{Sr(C)}$ that is independent of temperature over the range 61-67°C. In contrast, it is well established that $K_{Sr(C)}$ varies with precipitation rate (Gabitov et al., 2014 and references therein). Following the model of DePaolo (2011), we can produce model curves that predict $K_{Sr(C)}$ as a function of precipitation rates at a given pH and temperature. This framework will allow us to compare expected $K_{Sr(C)}$ at precipitation rates estimated from our growth slides at the Bridgeport site as well as for the travertines studied by Kele et al. (2008). The DePaolo (2011) model for Sr partitioning into calcite is given by:

$$K_{Sr(C)} = \frac{K_f}{1+\frac{R_b}{R_p+R_b}\left(\frac{K_f}{K_{eq}}-1\right)} \quad [1]$$

where K_{eq} and K_f are the equilibrium and kinetic end-member values for K_{Sr}, R_p is the precipitation rate, and R_b is the gross backwards rate (where $R_p = R_f - R_b$). Temperature and pH dependencies of R_b are given by Chou et al. (1989) and Pokrovsky et al. (2009), respectively. Within this model framework, the $K_{Sr(C)}$ of 0.15 seen in Kele et al. (2008) corresponds to a precipitation rate between $10^{-4.6}$ and $10^{-4.3}$ mol/m^2/s at 64°C and pH of 6.7 (Fig. 12). The range of possible rates is due to selection of equilibrium and kinetic end-member values for K_{Sr}, with most of the sensitivity accounted for by the selection of equilibrium partition coefficient. At a given $K_{Sr(C)}$, an equilibrium K_{Sr} of 0.02 shifts the curve to faster rates, and 0.03 shifts the curve towards slower rates (Fig. 12).

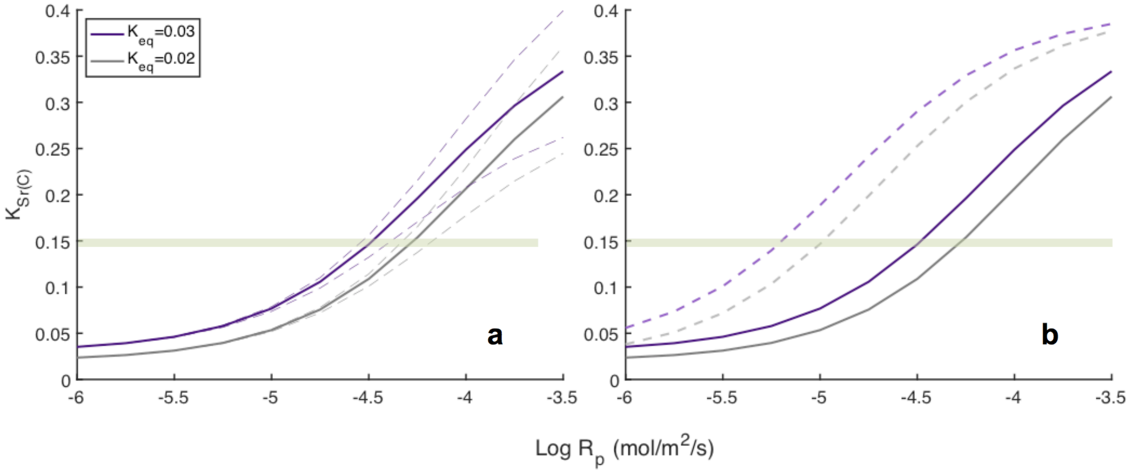

Figure 12. DePaolo (2011) model for calcite K_{Sr} as a function of precipitation rate at (a) 64°C and pH of 6.7, corresponding to conditions in the Hungarian travertines. Thin dashed lines show possible spread in model curves based on range of K_f from 0.3 to 0.5. (b) Bold dashed lines show shift in model curves based on use of smaller R_b. Horizontal line indicates approximate value of calcite K_{Sr} given by Kele et al. (2008), and solid lines are same as in (a).

It is important to note that the estimated value for the gross backwards rate, R_b, is experimentally derived for calcite under impurity-free conditions. Recent work (cf. Chapter 4 of this dissertation) has demonstrated that the presence of Mg (either in solution and/or as an incorporated impurity) may result in a corresponding decrease in R_b, even with the low Kele et al. (2008) Mg/Ca fluid ratios of ~0.3 and mole fractions, X_{MgCO3}, of ~3%. Consequently, corresponding rate estimates for the Kele et al. (2008) travertines could be as low as $10^{-5.2}$ or $10^{-5.0}$ mol/m^2/s (Fig. 12), which would put them in much closer agreement to the rates estimated based on our growth slides, of approximately $10^{-5.22}$ mol/m^2/s. Although there is no reason to expect that their rates will agree with ours, it is important to consider the uncertainty associated with assuming a value for R_b based on pure calcite dissolution experiments (Chou et al., 1989).

At the precipitation rate of $10^{-5.22}$ mol/m^2/s that we estimated with *in situ* growth slides, and in the pH and temperature range observed at Bridgeport (6.7-7.3 and 61-72°C, respectively), $K_{Sr(C)}$ is approximately 0.06 when K_f and K_{eq} values of 0.4 and 0.03 are used, using the pure-calcite-based R_b estimate. If a lower R_b is used, $K_{Sr(C)}$ at the same precipitation rate is approximately 0.14 (Fig. 13). As is evident from this comparison and as previously pointed out by DePaolo (2011), R_b is crucial for accurate predictions of $K_{Sr(C)}$ in this range of growth rates.

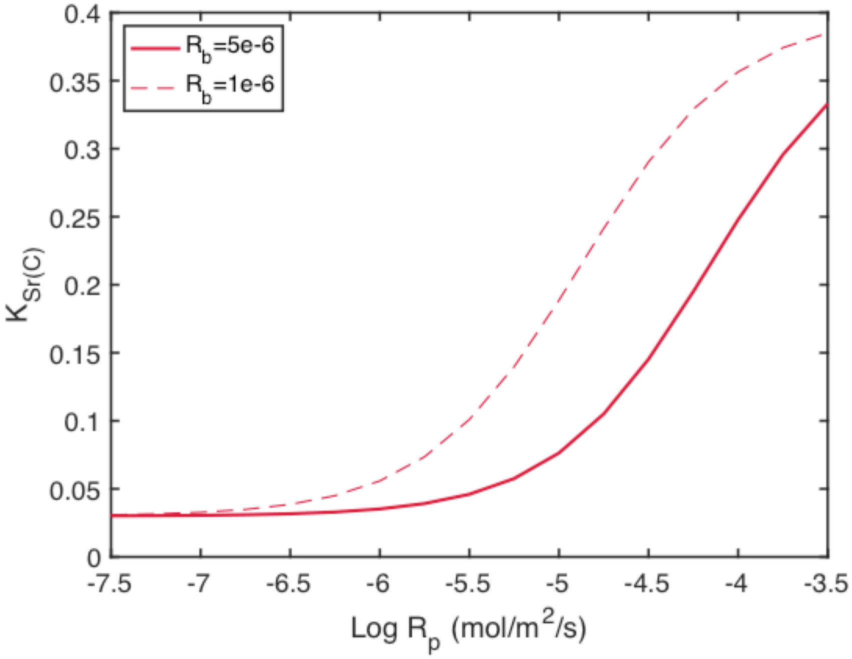

Figure 13. DePaolo (2011) model for calcite K_{Sr} in Bridgeport travertines as a function of precipitation rate at 66.5°C and pH of 7, corresponding to conditions mid-conduit. Shift in model curves indicates difference in predictions of K_{Sr} when the R_b is predicted by empirical models for pure calcite dissolution, versus a smaller R_b, which may occur in more complex solutions.

Although the absolute value of K_{Sr} in the Bridgeport calcite cannot be tightly constrained, we have shown that it most likely falls into the range of 0.04-0.20, which agrees with experimentally determined values as well as the value determined by Kele et al. (2008) in a similar growth environment. This approximation of $K_{Sr(C)}$ allows us to demonstrate that $K_{Sr(A)}$, although significantly higher than most literature values predict, is indeed greater than 1.2, again in agreement with the Hungarian travertines of Kele et al. (2008). There are numerous complexities in travertine environments in comparison to controlled laboratory studies, and consequently we cannot speak to what causes these $K_{Sr(A)}$ to be so much higher than predicted. However, our calculations illustrate the failure of experimental results to predict partitioning behavior in nature, and suggest they should therefore be used with caution both in model design and in application to natural systems.

4.2.1.2 Magnesium partitioning, K_{Mg}

Experimental studies of inorganic calcite suggest that K_{Mg} values in calcite are generally between 0.012 and 0.116 (Mucci and Morse, 1983; Oomori et al., 1987; Katz, 1973; Rimstidt et al., 1998; Mavromatis et al., 2013), while those of aragonite are approximately 2-3 orders of magnitude lower and shown to be inversely dependent on temperature (Gaetani and Cohen, 2006). Various controls on K_{Mg} in calcite have been proposed, including Mg/Ca of solution (Morse and Bender 1990; Mucci and Morse, 1983; Berner 1975), precipitation rate (e.g., Mavromatis et al., 2013), and temperature (Katz, 1973; Oomori et al., 1987; Lopez et al., 2009).

Bulk K_{Mg} values measured in Bridgeport travertines (0.04-0.19) are generally higher than the range of 0.02-0.11 observed by Kele et al. (2008), which is surprising considering the comparatively larger aragonite fraction. Given that $K_{Mg(A)}$ are thought to be 2-3 orders of magnitude smaller than that of calcite, more aragonite present should result in smaller bulk K_{Mg} values at the Bridgeport site. Furthermore, unlike the bulk K_{Sr} values, we do not observe a shift from lower to higher K_{Mg} down-conduit as would be expected from increasingly higher fractions of calcite.

Assuming a linear temperature dependence of $K_{Mg(C)} = 0.0009 + 0.0348$ (Katz et al., 1973), a temperature shift from 71°C to 62°C would correspond to $K_{Mg(C)}$ values of 0.0987 ± 0.0049 (2 s.d.) and 0.0906 ± 0.0045 (2 s.d.). These values, however, are still one half of the maximum value measured in the Bridgeport travertines. Notably, Katz (1973) observed anomalously high $K_{Mg(C)}$ values of 0.11 at 50°C and up to 0.44 at 70°C, which occurred during very fast recrystallization from aragonite to calcite. This observation is qualitatively consistent with findings of Kitano et al. (1971), who determined from free-drift seeded precipitation experiments that partitioning of Sr can be up to 3-4 times greater very early on in calcite precipitation than it is as precipitation proceeds and growth rate slows. Brown et al. (2013) found that in recrystallized carbonate from well casings at ~160°C in the Long Valley region of California, K_{Sr} ranges from 0.06 to 0.81, which is roughly twice the value thought to be possible at the kinetic limit based on experimental data. Although Sr and Mg are not expected to behave identically in terms of their partitioning into calcite, they both have partition coefficients less than 1, which means they both may be enriched in the surface layer during fast growth.

It is also possible that there is a Mg-rich solid phase in trace quantities, causing the Mg content determined via bulk digestion to be anomalously high for both calcite and aragonite. Alternatively, past Mg concentrations may have been considerably higher or temperatures much greater than those of today. An increase of fluid Mg/Ca ratios by 20 to 100% would be required to attain K_{Mg} values close to those expected for calcite at the given temperatures. Alternatively, much higher temperatures would make these values more reasonable, although this does conflict with the relative temperature stability between the 1970s and today (Table 4; Mariner et al., 1977).

4.2.2 Ca isotopes

Although there are small variations in the fluid and carbonate δ^{44}Ca values (Fig 9), they do not vary systematically in any way in spite of the near-monotonically changing polymorph fractions, decreasing temperature, or increasing pH. Consequently, the calculated $\Delta^{44/40}$Ca are also relatively invariant. Here we discuss possible explanations for the magnitude and lack of trend in Ca isotopes.

Because Ca isotope fractionation as well as Sr partitioning in calcite are rate-dependent processes, the surface kinetic model of DePaolo (2011) can be used to estimate values of $\Delta^{44/40}$Ca for the Bridgeport carbonates at our estimated rates and given temperatures and pH range. It should be emphasized that these are estimates, as we cannot assume *a priori* that calcite and aragonite have the same rate dependence, and literature data is insufficient for inorganic aragonite. Similar to $K_{Sr(C)}$, equation 2 (DePaolo, 2011) states that isotopic fractionation between solid and fluid (α_p) is a function of the equilibrium fractionation (α_{eq}), kinetic fractionation (α_f), net precipitation rate (R_p) and gross backwards rate (R_b). Alpha can be related to delta values through the relation: $\Delta \approx 1000*(\alpha-1)$, where an alpha value equal to unity means there is no isotopic discrimination between the solid and fluid (i.e., $\Delta = 0$).

$$\alpha_p = \frac{\alpha_f}{1+\frac{R_b}{R_p+R_b}\left(\frac{\alpha_f}{\alpha_{eq}}-1\right)} \quad [2]$$

Again, R_b is determined from the pH and temperature dependencies given by Chou et al. (1989) and Pokrovsky et al. (2009), respectively. Total variation in R_p due to T and pH constraints on R_b are relatively minor (maximum range of 0.3 logR units) within the Bridgeport system, but can be seen in Fig. 14. With an equilibrium fractionation α_{eq} = 1.0000 (Fantle and DePaolo, 2007) and kinetic fractionation α_f = 0.9984, estimated $\Delta^{44/40}$Ca around R_p of $10^{-5.22}$ mol/m^2/s is between -0.7 and -0.9 at temperatures of 71 and 62°C, respectively (Fig. 14).

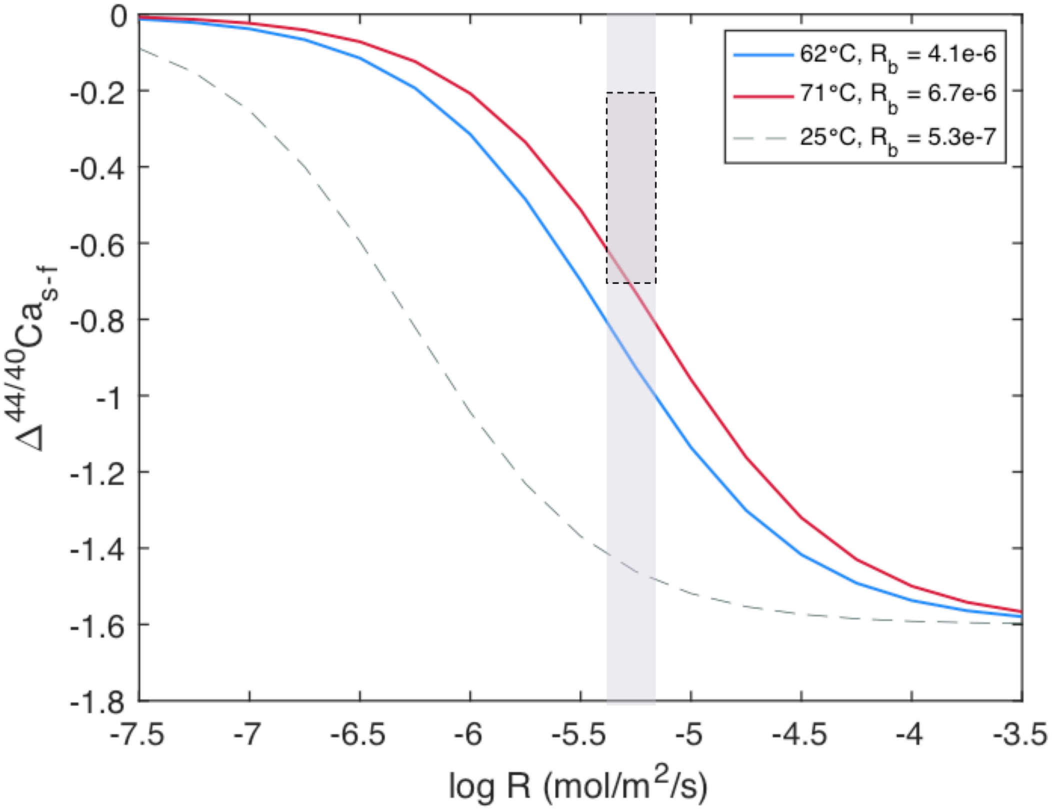

Figure 14. DePaolo (2011) model curves for $\Delta^{44/40}$Ca as a function of precipitation rate at temperatures between 62-71°C and pH = 7 (α_{eq} = 1.0000 and α_f = 0.9984). R_b is predicted by empirical models for pure calcite dissolution, approximately 6.7e-6 mol/m^2/s. Shaded bar indicates estimated precipitation rates from *in situ* growth slides, while dashed-line box provides range of measured $\Delta^{44/40}$Ca at the estimated precipitation rate.

Similar to the bulk partition coefficients, the solid $\Delta^{44/40}$Ca values reflect a mixture of calcite and aragonite fractionation in varying proportions. Aragonite fractionation is thought to be approximately 0.6 greater (i.e., more negative) than that of calcite (e.g., Tang et al., 2008; AlKhatib and Eisenhauer, 2017; Gussone et al., 2005). Consequently, in the model, we need to fit $\Delta^{44/40}$Ca values that are of smaller absolute magnitude than the bulk $\Delta^{44/40}$Ca data, which generally fall between -0.3 and -0.7 (Fig. 9). At the same rates, smaller magnitude fractionations at a given rate can be produced with the DePaolo (2011) model by increasing the kinetic fractionation factor such that it becomes closer to the equilibrium fractionation. However, increasing α_f from 0.9984 to 0.9986 can only shift the model $\Delta^{44/40}$Ca by +0.1 at the estimated rate (not shown). This suggests that either the actual precipitation rates are closer to 10^{-6} mol/m^2/s, or that R_b is approximately 5x faster than predicted, as depicted in Figure 15, which is unlikely, given the presence of Mg and other impurity ions in solution (cf. Chapter 4).

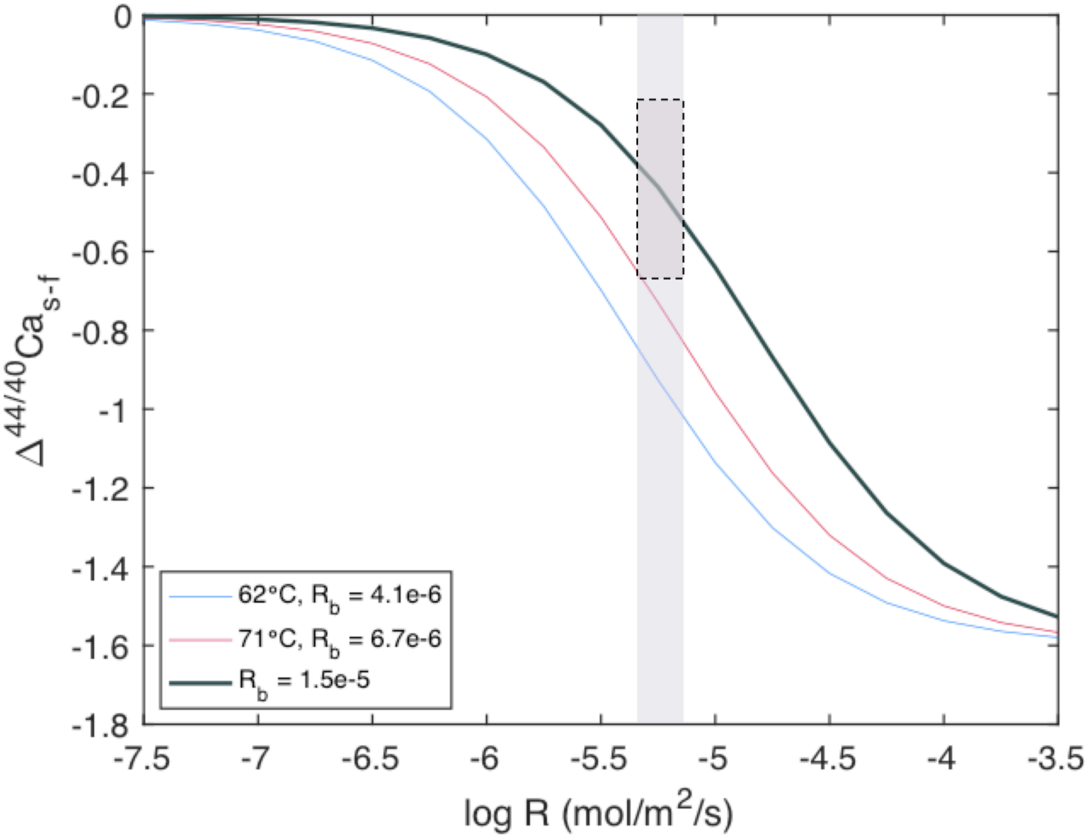

Figure 15. DePaolo (2011) model curve for $\Delta^{44/40}$Ca with R_b approximately 5x faster than predicted by empirical models for pure calcite dissolution. Shaded bar indicates estimated precipitation rates from *in situ* growth slides, while dashed-line box provides range of measured $\Delta^{44/40}$Ca at the estimated precipitation rate (α_{eq} = 1.0000 and α_f = 0.9984).

If both calcite and aragonite were forming at the same rate and had a fixed offset in $\Delta^{44/40}$Ca, we would expect to see a mixing line like that observed in the bulk data for solid δ^{13}C and Sr/Ca (Fig. 3 and 6). It is possible that the precipitation rates do not change monotonically down-conduit. However, given no significant changes in the Sr, Mg, SO_4 concentrations in fluids, the increasing Ω values for both calcite and aragonite with distance from the inlet (Fig. 1) suggest rates should also be increasing in proportion to these values according to affinity-based rate models (cf. Palandri and Kharaka, 2004). Literature suggests that aragonite will precipitate faster than calcite in this system (Zhong and Mucci, 1989) with Ω_A values >3.0. However, even if this were the case, with a fixed offset in fractionation, the phase mixture should still be observable. Many factors can alter the kinetics of precipitation greatly from those expected based on experimental data, however, and consequently affinity-based rate models often do not predict growth rates accurately, which is likely what we are observing here.

Given that $\Delta^{44/40}$Ca is a function of rate, the most straightforward explanation for invariant $\Delta^{44/40}$Ca is that the rate is not increasing in proportion to the increase in saturation state down-conduit, or the rate of CO_2 degassing, which we estimate would correspond to a precipitation rate of approximately 0.016 mol/m^2/s, assuming changes in DIC are reflecting only CO_2 degassing. Burton and Walter (1987) demonstrated that rates of aragonite precipitation are strongly temperature dependent, but only weakly dependent on solution saturation state. This lack of dependence may play a role in explaining the absence of a mixing line.

The consistent offset in fractionation between calcite and aragonite precipitated at the same growth rate observed in both experimental studies and marine calcifying organisms (if it is a robust phenomenon within carbonate systems), may not be as large at temperatures of 62-71°C. If an offset exists and is relatively small, then systematic changes in $\Delta^{44/40}$Ca would not be observable if the rates of calcite and aragonite precipitation resulted in fractionation of similar magnitude. With that in mind, deviations from a monotonically decreasing fraction of aragonite could possibly create the type of scatter seen in the data.

The most plausible explanation for why we do not observe a mixing line between calcite and aragonite in the calcium isotope data is that we are observing effects of partially recrystallized carbonate. It may be that the solids measured in this study are composed of primary calcite and aragonite precipitated on the walls of the crestal conduit as well as recrystallized carbonate from within the first few millimeters of the newly precipitated porous travertine (Fig. 16). Although we do not have measurements of the temperature gradient moving orthogonally from the fluid into the conduit walls, there will be some degree of cooling as a function of distance from the hot fluid and proximity to ambient air, decreasing the stability of aragonite and promoting recrystallization to calcite. Electron microprobe images (Fig. 2) show massive calcite grown around aragonite spherulites as well as less commonly, tightly intergrown bladed aragonite. These observations have the following implications: (1) this massive calcite precipitation occurred quickly relative to the larger, euhedral calcite rhombs, and (2) precipitation occurred in a confined space. Secondary calcite precipitation occurring at different rates than primary calcite and aragonite growth, if extensive enough, could shift the bulk δ^{44}Ca.

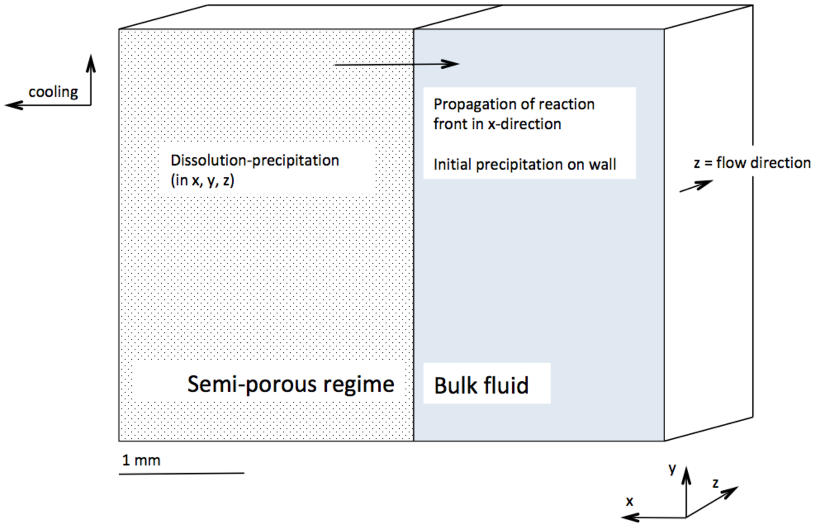

Figure 16. Schematic of growth regimes. While initial precipitation occurs on the wall of the conduit, we propose a possible role of dissolution-precipitation (i.e., recrystallization) within all directions in the semi-porous regime.

5. Conclusions

Travertine deposits are highly complex carbonate systems, and complicated in the case of the Bridgeport locality by simultaneous deposition of calcite and aragonite. In spite of these complexities, our work has interesting implications for trace element partitioning and interpretation of Ca isotopes in terrestrial carbonates based on existing kinetic models.

Our calculations demonstrate that although there is a temperature dependence on the Sr partition coefficient (K_{Sr}) for aragonite, constraints of calcite partition coefficients require that most of the down-conduit decrease in K_{Sr} reflects decreasing fractions of aragonite. Overall, bulk Sr partition coefficients (K_{Sr}) are very high, although given the estimated fractions of calcite and aragonite, results in calcite K_{Sr} values that are reasonable based on experimental data. In contrast, the K_{Sr} values for aragonite are much higher than expected based on laboratory experiments, but may not be anomalous for aragonite-dominant thermogene travertines. These high K_{Sr} values could be also due to very fast rates of aragonite precipitation on the conduit walls and fast calcite precipitation in the porous matrix of the conduit wall. Future studies should explore further why and how this large magnitude partitioning occurs. Bulk partition coefficients of Mg are abnormally high, even for thermogene travertines. They can potentially be explained by rapid incorporation during early growth stages of aragonite and calcite.

We observe Ca isotope fractionation that is relatively invariant with changing fractions of aragonite and calcite, which is surprising given the expected difference in fractionation factors between these two polymorphs. We argue that the isotopic invariance is likely due to recrystallization in the porous conduit wall occurring at different rates than initial carbonate growth, and that these different rates alter the initial $\Delta^{44/40}$Ca signal.

Appendix

XRD spectra.

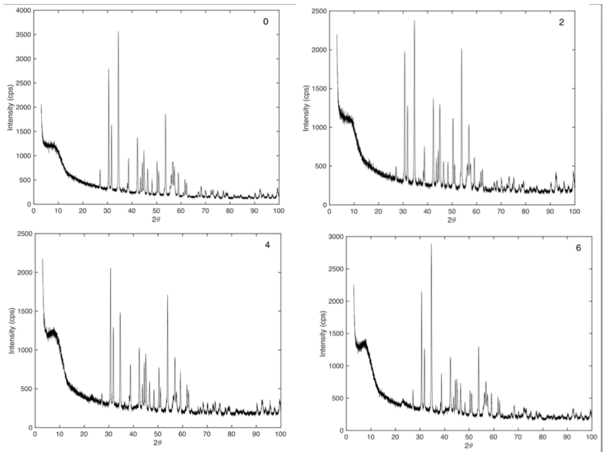

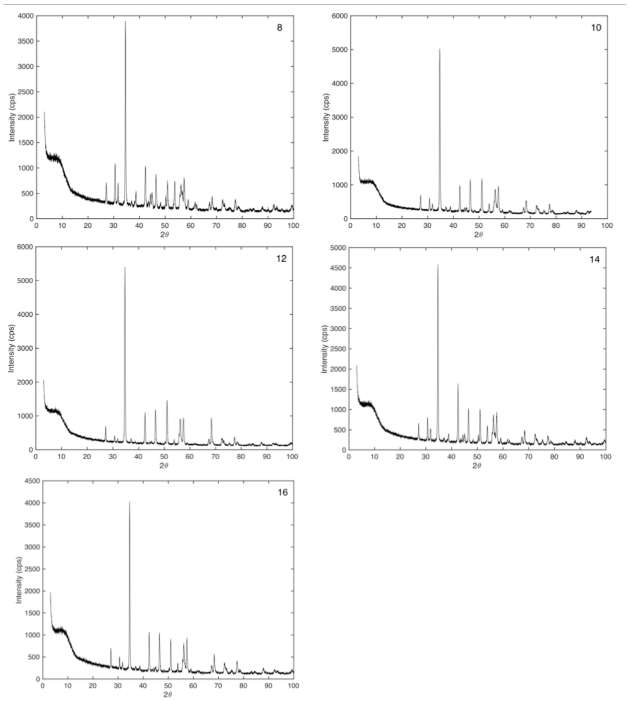

Acknowledgements

I am grateful to the following people who helped assist with field sampling and analyses.

Nick Botto, UC Davis
Wenbo Yang, UC Berkeley
Markus Bill, LBNL
Shaun Brown, UC Berkeley/LBNL
Holly Barnhart, UC Berkeley
Chelsea Willett, UC Berkeley
Marissa Tremblay, UC Berkeley
Jenny Mills, UC Berkeley
Tim Teague, UC Berkeley

This research was supported by the U.S. Department of Energy, Office of Science, Office of Basic Energy Sciences, Chemical Sciences, Geosciences, and Biosciences Division, under Award Number DE-AC02-05CH11231.

References

AlKhatib, M., & Eisenhauer, A. (2017a). Calcium and strontium isotope fractionation in aqueous solutions as a function of temperature and reaction rate; I. Calcite. *Geochimica et Cosmochimica Acta*, *209*, 296-319

AlKhatib, M., & Eisenhauer, A. (2017b). Calcium and strontium isotope fractionation during precipitation from aqueous solutions as a function of temperature and reaction rate; II. Aragonite. *Geochimica et Cosmochimica Acta*, *209*, 320-342.

Amundson, R., & Kelly, E. (1987). The chemistry and mineralogy of a CO2-rich travertine depositing spring in the California Coast Range. *Geochimica et Cosmochimica Acta*, *51*(11), 2883-2890.

Barnes, I. (1965). Geochemistry of Birch Creek, Inyo County, California a travertine depositing creek in an arid climate. *Geochimica et Cosmochimica Acta*, *29*(2), 85-112.

Berner, R. A. (1975). The role of magnesium in the crystal growth of calcite and aragonite from sea water. *Geochimica et Cosmochimica Acta*, *39*(4), 489-504.

Böhm, F., Gussone, N., Eisenhauer, A., Dullo, W. C., Reynaud, S., & Paytan, A. (2006). Calcium isotope fractionation in modern scleractinian corals. *Geochimica et Cosmochimica Acta*, *70*(17), 4452-4462.

Brown, S. T., Kennedy, B. M., DePaolo, D. J., Hurwitz, S., & Evans, W. C. (2013). Ca, Sr, O and D isotope approach to defining the chemical evolution of hydrothermal fluids: Example from Long Valley, CA, USA. *Geochimica et Cosmochimica Acta*, *122*, 209-225.

Buczynski, C., & Chafetz, H. S. (1991). Habit of bacterially induced precipitates of calcium carbonate and the influence of medium viscosity on mineralogy. *Journal of Sedimentary Research*, *61*(2), 226-233.

Burton, E. A., & Walter, L. M. (1987). Relative precipitation rates of aragonite and Mg calcite from seawater: Temperature or carbonate ion control?. *Geology*, *15*(2), 111-114.

Chafetz, H., Rush, P. F., & Utech, N. M. (1991). Microenvironmental controls on mineralogy and habit of CaCO3 precipitates: an example from an active travertine system. *Sedimentology*, *38*(1), 107-126.

Chou, L. E. I., Garrels, R. M., & Wollast, R. (1989). Comparative study of the kinetics and mechanisms of dissolution of carbonate minerals. *Chemical geology*, *78*(3-4), 269-282.

De Choudens-Sanchez, V., & Gonzalez, L. A. (2009). Calcite and aragonite precipitation under controlled instantaneous supersaturation: elucidating the role of CaCO3 saturation state and Mg/Ca ratio on calcium carbonate polymorphism. *Journal of Sedimentary Research*, *79*(6), 363-376.

DePaolo, D. J. (2011). Surface kinetic model for isotopic and trace element fractionation during precipitation of calcite from aqueous solutions. *Geochimica et Cosmochimica Acta*, *75*(4), 1039-1056.

Fantle M. S. and DePaolo D. J. (2007) Ca isotopes in carbonate sediment and pore fluid from ODP Site 807A: the Ca2+(aq)- calcite equilibrium fractionation factor and calcite recrystallization rates in Pleistocene sediments. Geochim. Cosmochim. Acta 71, 2524–2546.

Farkaš, J., Buhl, D., Blenkinsop, J., & Veizer, J. (2007). Evolution of the oceanic calcium cycle during the late Mesozoic: evidence from δ44/40Ca of marine skeletal carbonates. *Earth and Planetary Science Letters*, *253*(1-2), 96-111.

Folk, R. (1994). Interaction between bacteria, nannobacteria, and mineral precipitation in hot springs of central Italy. *Géographie physique et Quaternaire*, *48*(3), 233-246.

Fouke, B. W., Farmer, J. D., Des Marais, D. J., Pratt, L., Sturchio, N. C., Burns, P. C., & Discipulo, M. K. (2000). Depositional facies and aqueous-solid geochemistry of travertine-depositing hot springs (Angel Terrace, Mammoth Hot Springs, Yellowstone National Park, USA). *Journal of Sedimentary Research*, *70*(3), 565-585.

Friedman, I. (1970). Some investigations of the deposition of travertine from hot springs—I. The isotopic chemistry of a travertine-depositing spring. *Geochimica et Cosmochimica Acta*, *34*(12), 1303-1315.

Gabitov, R. I., & Watson, E. B. (2006). Partitioning of strontium between calcite and fluid. *Geochemistry, Geophysics, Geosystems*, *7*(11).

Gabitov, R. I., Sadekov, A., & Leinweber, A. (2014). Crystal growth rate effect on Mg/Ca and Sr/Ca partitioning between calcite and fluid: An in situ approach. *Chemical Geology*, *367*, 70-82.

Gaetani, G. A., & Cohen, A. L. (2006). Element partitioning during precipitation of aragonite from seawater: a framework for understanding paleoproxies. *Geochimica et Cosmochimica Acta*, *70*(18), 4617-4634.

Gebrehiwet, T. A., Redden, G. D., Fujita, Y., Beig, M. S., & Smith, R. W. (2012). The Effect of the CO 3 2-to Ca 2+ Ion activity ratio on calcite precipitation kinetics and Sr 2+ partitioning. *Geochemical transactions*, *13*(1), 1.

Govan, F. A. (Ed.). (1983). *Thermal Insulation, Materials, and Systems for Energy Conservation in the'80s* (Vol. 789). ASTM International.

Guo, L., & Riding, R. (1992). Aragonite laminae in hot water travertine crusts, Rapolano Terme, Italy. *Sedimentology*, *39*(6), 1067-1079.

Gussone, N., Böhm, F., Eisenhauer, A., Dietzel, M., Heuser, A., Teichert, B. M., ... & Dullo, W. C. (2005). Calcium isotope fractionation in calcite and aragonite. *Geochimica et Cosmochimica Acta*, *69*(18), 4485-4494.

Gussone, N., Eisenhauer, A., Tiedemann, R., Haug, G. H., Heuser, A., Bock, B., ... & Müller, A. (2004). Reconstruction of Caribbean sea surface temperature and salinity fluctuations in response to the Pliocene closure of the Central American Gateway and radiative forcing, using δ 44/40 Ca, δ 18 O and Mg/Ca ratios. *Earth and Planetary Science Letters*, *227*(3), 201-214.

Herman, J. S., & Lorah, M. M. (1988). Calcite precipitation rates in the field: measurement and prediction for a travertine-depositing stream. *Geochimica et Cosmochimica Acta*, *52*(10), 2347-2355.

Jones, B., & Peng, X. (2016). Mineralogical, crystallographic, and isotopic constraints on the precipitation of aragonite and calcite at Shiqiang and other hot springs in Yunnan Province, China. *Sedimentary geology*, *345*, 103-125.

Jones, B., & Renaut, R. W. (2008). Cyclic development of large, complex, calcite dendrite crystals in the Clinton travertine, Interior British Columbia, Canada. *Sedimentary Geology*, *203*(1-2), 17-35.

Katz, A. (1973). The interaction of magnesium with calcite during crystal growth at 25–90 C and one atmosphere. *Geochimica et Cosmochimica Acta*, *37*(6), 1563-1586.

Kele, S., Demény, A., Siklósy, Z., Németh, T., Tóth, M., & Kovács, M. B. (2008). Chemical and stable isotope composition of recent hot-water travertines and associated thermal waters, from Egerszalók, Hungary: Depositional facies and non-equilibrium fractionation. *Sedimentary Geology*, *211*(3-4), 53-72.

Kinsman, D. J., & Holland, H. D. (1969). The co-precipitation of cations with CaCO3—IV. The co-precipitation of Sr2+ with aragonite between 16° and 96° C. *Geochimica et Cosmochimica Acta*, *33*(1), 1-17.

Lopez, O., Zuddas, P., & Faivre, D. (2009). The influence of temperature and seawater composition on calcite crystal growth mechanisms and kinetics: Implications for Mg incorporation in calcite lattice. *Geochimica et Cosmochimica Acta*, *73*(2), 337-347.

Lorens, R. B. (1981). Sr, Cd, Mn and Co distribution coefficients in calcite as a function of calcite precipitation rate. *Geochimica et Cosmochimica Acta*, *45*(4), 553-561.

Mariner, R.H., Presser, T.S., Evans, W.C. (1977). Hot springs of the central Sierra Nevada, California. United States Department of the Interior Geological Survey, Open-File Report 77-559.

Mavromatis, V., Gautier, Q., Bosc, O., & Schott, J. (2013). Kinetics of Mg partition and Mg stable isotope fractionation during its incorporation in calcite. *Geochimica et Cosmochimica Acta*, *114*, 188-203.

Morse, J. W., & Bender, M. L. (1990). Partition coefficients in calcite: Examination of factors influencing the validity of experimental results and their application to natural systems. *Chemical Geology*, *82*, 265-277.

Morse, J. W., Wang, Q., & Tsio, M. Y. (1997). Influences of temperature and Mg: Ca ratio on CaCO3 precipitates from seawater. *Geology*, *25*(1), 85-87.

Mucci, A., & Morse, J. W. (1983). The incorporation of Mg2+ and Sr2+ into calcite overgrowths: influences of growth rate and solution composition. *Geochimica et Cosmochimica Acta*, *47*(2), 217-233.

Nägler, T. F., Eisenhauer, A., Müller, A., Hemleben, C., & Kramers, J. (2000). The δ44Ca-temperature calibration on fossil and cultured Globigerinoides sacculifer: New tool for reconstruction of past sea surface temperatures. *Geochemistry, Geophysics, Geosystems*, *1*(9).

Nielsen, L. C., & DePaolo, D. J. (2013). Ca isotope fractionation in a high-alkalinity lake system: Mono Lake, California. *Geochimica et Cosmochimica Acta*, *118*, 276-294.

Oehlerich, M., Mayr, C., Gussone, N., Hahn, A., Hölzl, S., Lücke, A., ... & Zolitschka, B. (2015). Lateglacial and Holocene climatic changes in south-eastern Patagonia inferred from carbonate isotope records of Laguna Potrok Aike (Argentina). *Quaternary science reviews*, *114*, 189-202.

Oomori, T., Kaneshima, H., Maezato, Y., & Kitano, Y. (1987). Distribution coefficient of Mg2+ ions between calcite and solution at 10–50 C. *Marine Chemistry*, *20*(4), 327-336.

Palandri, J. L., & Kharaka, Y. K. (2004). *A compilation of rate parameters of water-mineral interaction kinetics for application to geochemical modeling* (No. OPEN-FILE-2004-1068). Geological Survey Menlo Park CA.

Parkhurst, D. L., & Appelo, C. A. J. (1999). User's guide to PHREEQC (Version 2): A computer program for speciation, batch-reaction, one-dimensional transport, and inverse geochemical calculations.

Payne, J. L., Turchyn, A. V., Paytan, A., DePaolo, D. J., Lehrmann, D. J., Yu, M., & Wei, J. (2010). Calcium isotope constraints on the end-Permian mass extinction. *Proceedings of the National Academy of Sciences*, *107*(19), 8543-8548.

Pentecost, A. (2005). *Travertine*. Springer Science & Business Media.

Plummer, L. N., Busenberg, E., & Riggs, A. C. (2000). In-situ growth of calcite at Devils Hole, Nevada: comparison of field and laboratory rates to a 500,000 year record of near-equilibrium calcite growth. *Aquatic Geochemistry*, *6*(2), 257-274.

Pokrovsky, O. S., Golubev, S. V., Schott, J., & Castillo, A. (2009). Calcite, dolomite and magnesite dissolution kinetics in aqueous solutions at acid to circumneutral pH, 25 to 150 C and 1 to 55 atm pCO2: New constraints on CO2 sequestration in sedimentary basins. *Chemical geology*, *265*(1-2), 20-32.

Renaut, R. W., & Jones, B. (1997). Controls on aragonite and calcite precipitation in hot spring travertines at Chemurkeu, Lake Bogoria, Kenya. *Canadian Journal of Earth Sciences*, *34*(6), 801-818.

Riding, R. (2011). Microbialites, stromatolites, and thrombolites. In *Encyclopedia of Geobiology* (pp. 635-654). Springer, Dordrecht.

Rimstidt, J. D., Balog, A., & Webb, J. (1998). Distribution of trace elements between carbonate minerals and aqueous solutions. *Geochimica et Cosmochimica Acta*, *62*(11), 1851-1863.

Romanek, C. S., Grossman, E. L., & Morse, J. W. (1992). Carbon isotopic fractionation in synthetic aragonite and calcite: effects of temperature and precipitation rate. *Geochimica et cosmochimica acta*, *56*(1), 419-430.

Rubinson and Clayton, 1969;, M., & Clayton, R. N. (1969). Carbon-13 fractionation between aragonite and calcite. *Geochimica et Cosmochimica Acta*, *33*(8), 997-1002.

Saltzman, M. R., & Thomas, E. (2012). Carbon isotope stratigraphy. In *The geologic time scale* (pp. 207-232).

Tang, J., Dietzel, M., Böhm, F., Köhler, S. J., & Eisenhauer, A. (2008). Sr2+/Ca2+ and 44Ca/40Ca fractionation during inorganic calcite formation: II. Ca isotopes. *Geochimica et Cosmochimica Acta*, *72*(15), 3733-3745.

Tang, J., Niedermayr, A., Köhler, S. J., Böhm, F., Kısakürek, B., Eisenhauer, A., & Dietzel, M. (2012). Sr2+/Ca2+ and 44Ca/40Ca fractionation during inorganic calcite formation: III. Impact of salinity/ionic strength. *Geochimica et cosmochimica acta*, *77*, 432-443.

Tesoriero, A. J., & Pankow, J. F. (1996). Solid solution partitioning of Sr2+, Ba2+, and Cd2+ to calcite. *Geochimica et Cosmochimica Acta*, *60*(6), 1053-1063.

Tipper, E. T., Galy, A., & Bickle, M. J. (2006). Riverine evidence for a fractionated reservoir of Ca and Mg on the continents: implications for the oceanic Ca cycle. *Earth and Planetary Science Letters*, *247*(3-4), 267-279.

Usdowski, E., Hoefs, J., & Menschel, G. (1979). Relationship between13C and18O fractionation and changes in major element composition in a recent calcite-depositing spring—A model of chemical variations with inorganic CaCO3 precipitation. *Earth and Planetary Science Letters*, *42*(2), 267-276.

Yan, H., Schmitt, A. D., Liu, Z., Gangloff, S., Sun, H., Chen, J., & Chabaux, F. (2016). Calcium isotopic fractionation during travertine deposition under different hydrodynamic conditions: Examples from Baishuitai (Yunnan, SW China). *Chemical Geology*, *426*, 60-70.

Zarasvandi, A., Roshanak, R., Gratzer, R., Pourkaseb, H., & Moore, F (2017) Stable isotope geochemistry of travertines from northern Urumieh-Dokhtar volcano-plutonic belt, Iran. *Carbonates and Evaporites*, 1-13.

Zhong, S., & Mucci, A. (1989). Calcite and aragonite precipitation from seawater solutions of various salinities: Precipitation rates and overgrowth compositions. *Chemical geology*, *78*(3-4), 283-299.

Zhu, P., & Macdougall, J. D. (1998). Calcium isotopes in the marine environment and the oceanic calcium cycle. *Geochimica et Cosmochimica Acta*, *62*(10), 1691-1698.

Chapter 4

Probing effects of Mg on Ca isotope fractionation in calcite: results from seeded growth experiments in a chemostat reactor

Abstract

This chapter presents the results of seeded calcite growth experiments performed at variable fluid Mg/Ca ratios at 25°C, pH of 8.2, ionic strength (NaCl) of 0.5M, and constant saturation index (SI) of 0.58. The aim of this study is to determine how the presence of Mg in solution during calcite growth impacts the fractionation of Ca isotopes between solid and fluid. A chemostat system was designed to titrate Ca and CO_3 ions into the solution in a 1:1 molar ratio, allowing the growth solution to remain at approximately steady state with respect to pH, carbonate alkalinity, and concentrations of Ca and Mg over 20 hours or more. In solutions with Mg/Ca varying from 0 to 1, we find that increasing Mg results in slower calcite growth and inhibition of spontaneous calcite nucleation, as predicted based on previous modeling and experimental work. Additionally, we find that the directionality and magnitude of the growth rate-dependence of Ca isotope fractionation is similar to that observed previously in Mg-free experiments where growth rate is varied by changing SI.

When considered within a surface kinetic modeling framework, these experiments enable us to distinguish between two surface growth inhibition mechanisms: pure kink blocking and incorporation inhibition. The observation that changing Mg/Ca at constant SI and changing SI in Mg-free solutions both result in a similar rate dependence on Ca isotope fractionation ($\Delta^{44/40}$Ca) has implications for understanding the mechanisms of growth inhibition. Using our data with previously established kinetic models, we infer that kink blocking cannot be the sole mechanism of growth inhibition by Mg. With only kink blocking, the forward and reverse fluxes of Ca ions (R_f and R_b) to the crystal surface would decrease proportionally with increasing Mg/Ca and slower growth rates. Hence, there would be no dependence of Ca isotope fractionation on growth rate. Our results show that Mg must decrease growth rate in a manner that allows R_f/R_b to approach unity with decreasing growth rate at constant SI, thus decoupling R_f/R_b from SI. This effect is expected to occur if Mg on the growing calcite surface destabilizes surface Ca ions, an incorporation inhibition effect. The dependence of $\Delta^{44/40}$Ca on the Mg/Ca ratio in solution demonstrates that both kink blocking and incorporation inhibition impact the kinetics of calcite growth.

Our experiments also suggest that partitioning of Mg into calcite may be controlled by the expression and growth of specific crystal faces onto which Mg preferentially attaches, and which are only present under certain growth conditions. Higher Mg/Ca ratios and more complex solutions should be probed in future work to more effectively inform interpretations of Ca isotope fractionation and Mg partitioning data in calcite, and increase applicability of experimental results to modern marine environments.

1. Introduction

A large body of work over the past decades has been dedicated to studying Ca isotopes in natural and synthetic calcite (e.g., DePaolo, 2004; LeMarchand et al., 2004; Fantle and DePaolo, 2005; Gussone et al., 2005; Fantle and DePaolo, 2007; Tang et al., 2008b; Tang et al., 2012; DePaolo, 2011; Nielsen and DePaolo, 2013; Higgins et al., 2018). Measurable variations in the ^{44}Ca/^{40}Ca ratio in calcite reflect the relative rates of incorporation of ^{44}Ca and ^{40}Ca into the growing solid (Nielsen et al., 2012). Ca isotope measurements in natural materials can be used to reveal specifics of the surrounding growth environment at the time of crystallization and thereby have the potential to serve as a useful proxy for interpreting geological samples (e.g., Fantle and DePaolo, 2005; Fantle and DePaolo, 2007; De La Rocha and DePaolo, 2000; Zhu and Macdougall, 1998). There have been significant advances in theory, including the surface kinetic model of DePaolo (2011) and development of the ion-by-ion model of calcite growth (Nielsen et al., 2012) linking ion attachment and detachment rates at the calcite surface to bulk precipitation rates, partitioning of trace elements, and isotopic effects. These models lead to specific hypotheses for which stable isotope effects can shed light on growth processes, and more specifically, on mechanisms of growth rate inhibition by trace elements. However, to improve the robustness of these models and advance our understanding of controls on Ca isotope incorporation, more experimental data is needed.

Few of the many experimental studies that have grown inorganic calcite under relatively controlled conditions (e.g., Bischoff, 1968; Katz, 1973; Berner, 1975; Mucci, 1986; Romanek et al., 1992; Zuddas and Mucci, 1994; Paquette and Reeder, 1995; Hartley and Mucci, 1996; Morse et al., 1997; Zuddas and Mucci, 1998; Kile et al., 2000; Jimenez-Lopez et al., 2001; Meldrum and Hyde, 2001; Jimenez-Lopez et al., 2004; LeMarchand et al., 2004; Nehrke et al., 2007; Tang et al., 2008a; Tang et al., 2008b; Lin and Singer, 2009; Lopez et al., 2009; Gebrehiwet et al., 2012; Tang et al., 2012; Mavromatis et al., 2013; AlKhatib and Eisenhauer, 2017) have also reported calcium isotope fractionation between the fluid and growing solid (LeMarchand et al., 2004; Tang et al., 2008b; Tang et al., 2012; AlKhatib and Eisenhauer, 2017). Although these experimental studies indicate that the ^{44}Ca/^{40}Ca fractionation between solid and growth solution varies with precipitation rate, there has been disagreement as to the directionality of the dependence (Fig. 1). LeMarchand et al. (2004) observed that the smallest ^{44}Ca/^{40}Ca solid-fluid fractionation occurs at fast rates, while the data from Tang et al. (2008b; 2012) and Watkins et al. (2017) illustrate the inverse behavior. Unfortunately, the dataset of AlKhatib and Eisenhauer (2017) was not able to conclusively resolve this disagreement, finding variable directionality of rate dependencies on fractionation as a function of temperature. However, plotting the data of AlKhatib and Eisenhauer (2017) alongside results sampling a much larger range of precipitation rates (Fig. 1) suggests that the spread in data from their experiments at 25°C may very well be due to inter-experimental variation, as their results match those of Tang et al. (2008b; 2012) within error.

While these experiments have been essential to understanding the rate dependence of Ca isotope fractionation, there are still numerous complexities in natural systems that may impact these isotopic effects. For robust application of δ^{44}Ca to interpretation of calcite formation in natural systems, it is crucial to understand how some of the complexities seen in nature impact the isotopic signatures. One important complexity is that natural calcite grows in the presence of a variety of trace metals that subsequently are scavenged from the aqueous phase and substitute for Ca in the growing lattice (e.g., Mg, Sr, Mn). Marine calcite, the most abundant type of calcite globally, forms from seawater with high molar Mg/Ca ratios. While modern Mg/Ca in oceans is approximately 5.2 (Lowenstein et al., 2014 and references therein), secondary or authigenic calcite that forms in sediments often does so with much higher and lower ambient pore fluid ratios (e.g., Wefer et al., 1998). Because marine calcite forms a large fraction of the geologic record and it is known that Mg in solution inhibits calcite growth, it is crucial to determine if the presence of this ion changes the relative rates at which ^{40}Ca and ^{44}Ca are incorporated into calcite.

It is currently thought that Mg in solution inhibits $CaCO_3$ growth predominately via kink blocking (Mucci and Morse, 1983; Nielsen et al., 2013; Dobbershütz et al., 2018) with a smaller contribution from incorporation inhibition. During kink blocking, solvated or partially desolvated Mg ions adsorb to kink sites, inhibiting subsequent attachment of carbonate ions. This process effectively decreases the total number of actively exchanging kink sites on the surface, and serves to proportionally decrease the forward and backward fluxes of Ca on the surface. Consequently, kink blocking due to Mg is not expected to affect the fractionation of Ca isotopes (Fig. 1) according to current models.

However, new thermodynamic data for the Mg-calcite solid solution suggest that Mg is likely to destabilize calcite considerably more than previously thought (Lammers and Mitnick, *in press*). If incorporation of Mg ions at the growing surface enhances solubility of the solid solution, we expect that the backwards, or detachment flux of Ca ions from the surface will either increase (or decrease less quickly) with respect to the forward flux. In this case, we expect the magnitude of Ca isotope fractionation to increase with lower Mg/Ca and increasing growth rate (Fig. 1). Thus, a careful study of the impact of variable aqueous Mg/Ca on Ca stable isotope fractionation can provide clear evidence of whether incorporation inhibition occurs during Mg-calcite growth.

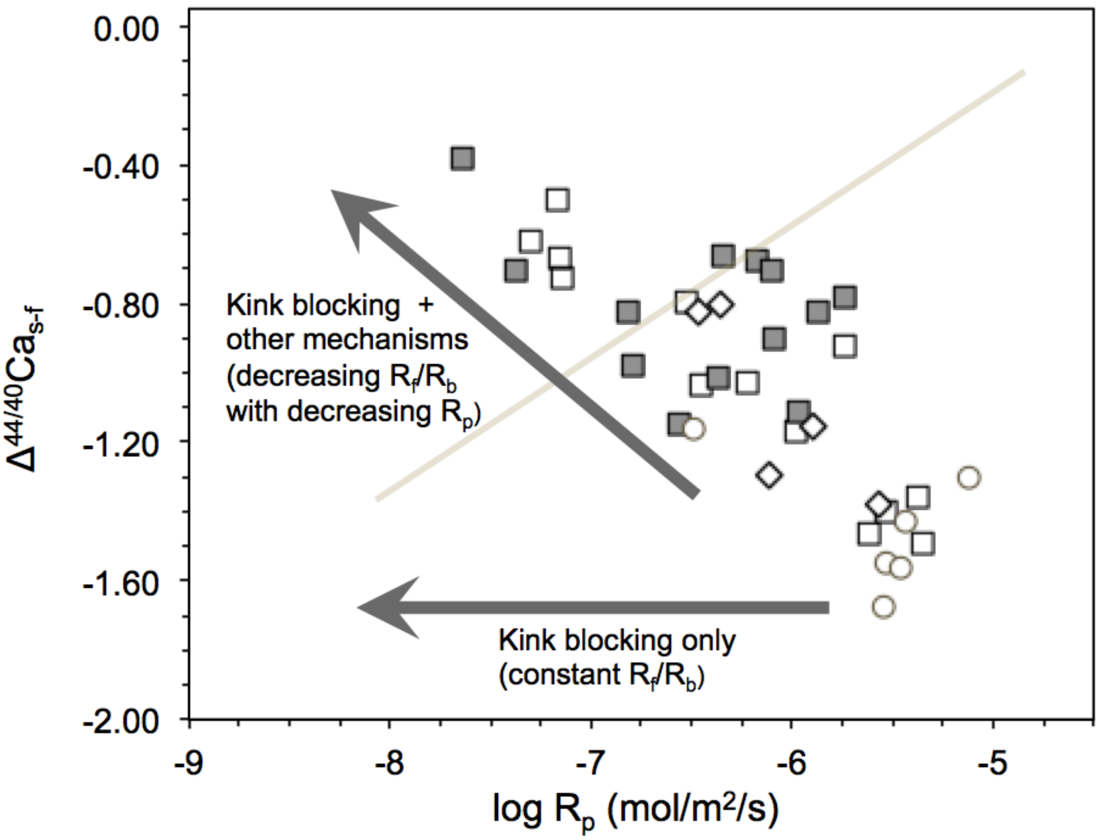

Figure 1. Ca isotope fractionation in laboratory-synthesize inorganic calcite reported as the isotopic composition of the solid (s) relative to fluid (f), where $\Delta^{44/40}Ca_{s\text{-}f}$ = $\delta^{44/40}Ca_{solid}$ - $\delta^{44/40}Ca_{fluid}$. (solid line = LeMarchand et al., 2004; open squares = Tang et al., 2008b; filled squares = Tang et al., 2012; open circles = AlKhatib and Eisenhauer, 2017; open diamonds = Watkins et al., 2017). Arrows illustrate expected trends based on Mg kinetic effects.

Several other factors may also contribute to the influence of Mg on the $\Delta^{44/40}$Ca during growth. The presence of Mg in solution and/or its preference for specific sites on the calcite surface (e.g., Wasylenki et al., 2005; Stephenson et al., 2011) suggests that the nature of Ca attachment could be perturbed to some degree. The slow desolvation kinetics of Mg (Kerisit and Parker, 2004; Hamm et al., 2010) could result in a perturbation to the local water structure and ionic interactions. If these perturbations are of sufficiently long duration relative to Ca attachment rates, they may affect dynamics of how the different Ca isotopes are incorporated. Furthermore, via kink blocking, Mg attachment will change the distribution of acute versus obtuse sites (e.g., Stephenson et al., 2011), which, beyond its effect on rate, could affect dynamics of ^{44}Ca/^{40}Ca attachment. Additionally, substitution of Ca by any foreign ion will strain the crystal lattice to some degree due to differences in cation radii, potentially increasing the activity of Ca enough to affect the surfaces fluxes that control isotopic fractionation. However, it has not previously been explored whether Mg simply inhibits growth, or if the disruption to the surface structure and energy landscape also results in a corresponding effect on Ca isotope fractionation.

The aim of the present study is to determine how the presence of Mg in solution, attachment of Mg on the calcite surface or the incorporation of Mg as a foreign ion affects Ca isotope fractionation. These data will shed light on the dominant mechanism of calcite growth rate inhibition by Mg. To this end, we have grown calcite at fixed supersaturation, ionic strength, pH, temperature, calcium concentrations and carbonate alkalinity in the presence of varying Mg/Ca solution ratios from 0 to 0.95. We report and discuss results of $^{44}Ca/^{40}Ca$ isotope fractionation measured in this experimentally grown calcite.

2. Methods

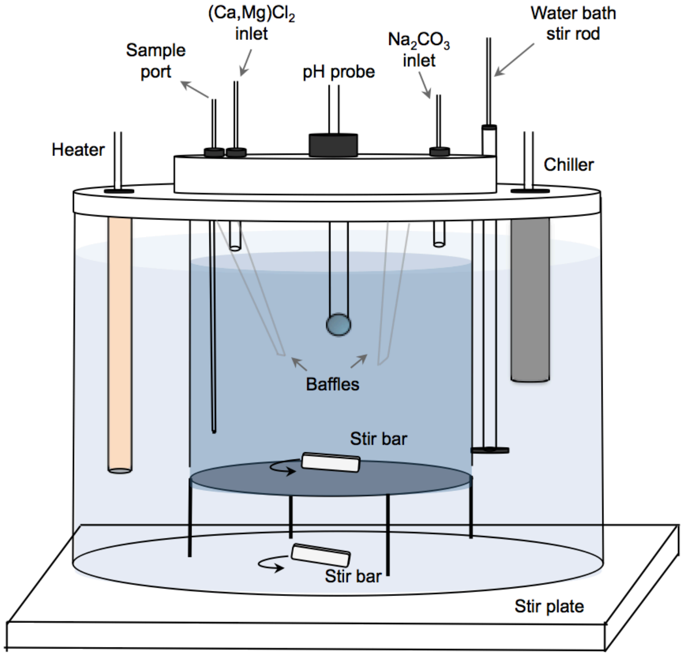

Figure 2. Schematic of experimental apparatus, with inner growth chamber residing in temperature-controlled water bath. (Inner vessel is 2 L; Stir bars approximately 2 inches long).

We modified the experimental apparatus of Watkins et al. (2013) to achieve a chemostat system (Fig. 2) capable of maintaining approximately steady state conditions with respect to pH, Ca, Mg, and carbonate alkalinity, on timescales ranging from many hours to several weeks. In most cases, Ca concentrations remained within 5%, but we consider steady state up to shifts of 15%. In order to maintain constant pH, Mg/Ca and

Ca/CO_3 during calcite precipitation, 0.2M $(Ca,Mg)Cl_2$ and 0.2M Na_2CO_3 solutions were titrated in as specified by the drift in pH. The titrators for the experimental apparatus were controlled via an interface manufactured by Jensen Systems, connecting the pH probe (Schott Instruments) to the titration software, MultiT 2.2. The method in MultiT allowed us to titrate in a designated volume of titrant to maintain a pH of 8.2. It should be noted for future chemostat growth experiments that fine-tuning this volume and determining titrant concentrations are non-trivial tasks.

Experiments were carried out in a 2L borosilicate vessel within a larger water bath, maintained at constant temperature by a dual heating-cooling system (Fig. 2). In all experiments, the inner reaction chamber was stirred at approximately 350 rpm with a basal stir bar. Many unsuccessful trial experiments as well as two successful runs (Exp1 and Exp3) were carried out prior to the determination that these systems were not sufficiently well stirred with a basal stir bar alone, causing a delay between the time of titration and a homogeneous growth solution. Upon discovery that the fluid was not homogenizing quickly enough, 10 mL pipette tips were added as baffles to promote much faster homogenization of the growth solution. Experiments were performed seeded at a pH of 8.2, ionic strength of 0.5 M (NaCl) and 25°C under fluid conditions specified in Table 1, with molar Mg/Ca ratios in the fluid ranging from 0 to 0.95. These Mg/Ca ratios correspond to experiment durations of 8 to 285 hours for experiments performed with baffles, and 481 and 1492 hours for two experiments (Exp1 and Exp3) run without baffles. Saturation indices and aqueous speciation calculations were done with the PhreeqC geochemistry program (Parkhurst and Appelo, 1999) using a calcite $\log K_{sp}$ value of -8.48 at 25°C (Plummer and Busenberg, 1982).

Concentrated solutions of $CaCl_2$-$MgCl_2$-NaCl and Na_2CO_3 (adjusted to pH 8.2) were prepared separately using NaCl salt, Na_2CO_3 salt, and two stock solutions of 2M $CaCl_2$ and 1M $MgCl_2$ in MilliQ water (18.2 Ω). After combining the two solutions in the 2L growth vessel and adjusting the final pH to 8.2 with HCl, seed was added and the vessel was sealed. Benchtop experiments ruled out any significant pH-effect of CO_2 degassing into the 0.8L headspace. Once the vessel was sealed, fluid aliquots were collected via a sampling port, then syringe filtered with 0.2μm Whatman filters. Cation and Ca isotope samples were acidified with trace metal grade nitric acid then stored in Parafilm-wrapped centrifuge tubes and refrigerated until measurement. Samples collected for alkalinity titrations were similarly stored but not acidified. Titrants were stored in either tedlar bags or tightly sealed flasks during the experiments to mitigate CO_2 degassing from the carbonate titrant as well as evaporation of both carbonate and $(Ca,Mg)Cl_2$ titrants. Measurements of titrant concentrations between identical trials confirmed that there was negligible drift in concentrations over the course of experiments. Ca and Mg concentrations of titrants and samples were measured via inductively coupled plasma optical emission spectroscopy (ICP-OES) and carbonate alkalinity was measured via Gran titration.

Sampling frequency was determined by growth rate, and is therefore variable, but in all cases a minimum of three samples were collected at the beginning, middle, and end of each trial. Because calcite was grown on pure calcite seed, the experiment duration was determined by how long it took for sufficient overgrowth to form in order that the uncertainty on the solid Ca isotope measurements approached the analytical uncertainty on the thermal ionization mass spectrometer (TIMS; approximately 0.12‰). Fractions of overgrowth (f_{OG}) relative to the total mass of calcite (seed plus overgrowth) are given in Table 1. At the completion of an experiment, the solution was immediately filtered via vacuum filtration and solids were collected on filter paper then rinsed with MilliQ and dried in a fume hood. The amount of overgrowth is calculated using the titration curves, concentration of Ca in the titrant measured via ICP-OES, and the seed is weighed on an analytical balance prior to addition.

Although these experiments were performed seeded, a fraction of calcite precipitation occurred on the surfaces of the growth chamber, pH probe, tubing, and baffles. Furthermore, although the calcite seed was effective in promoting growth of low-Mg calcite, rather than aragonite, the variant crystal sizes observed in SEM images (Fig. 3a-e) indicate that using the surface area of seed material is not a good approximation of precipitate specific surface area due to extensive 2D nucleation on the seed surfaces.

As pointed out by Watkins et al. (2013), quantifying surface area during growth experiments is challenging. It is not possible to collect solids during an experiment with this type of apparatus for two reasons. One, opening the sealed vessel to collect precipitate would introduce fluid-atmosphere exchange, perturb pH, and result in titration not due to precipitation, thereby increasing supersaturation of fluids and changing the targeted growth conditions. Two, because most (if not all) precipitation was occurring on calcite and vessel surfaces, it was not possible to collect solids through the tubing used to collect fluid samples. Furthermore, even if this were possible, the suspended particles would not be fairly representative of the growing material, given that they would likely be of much higher specific surface area than the real particle distribution.

However, given the importance of total surface area (SA_{total}) in determining rates, it is imperative to estimate specific surface areas (SSA; m^2/g) based on the precipitates and not simply use a literature estimate (cf. Watkins et al., 2013), as small differences in experimental conditions may result in considerable differences in crystal size distributions or morphology. To provide the most rigorous estimates of SA_{total} possible, we analyzed seed material (Fig. 4) as well as precipitates from each experiment individually and obtained experiment-specific SSA values reported in Table 2. The seed material had an average SSA of 0.45±0.1 m^2/g. Using these values, we implemented an approach similar to that described by Tang et al. (2008b), but with a modification akin to that employed by Jimenez-Lopez et al. (2001) due to our use of seed and observation of nucleation on seed surfaces. The total surface area is estimated according to Equation 1 in order to account for the average surface area from each experiment:

$$SA_{total} = 0.5*(SSA_s * m_s + SSA_p * m_p) \qquad (1)$$

where *s* denotes seed, *p* denotes precipitate, and *m* is mass. This equation captures the average surface area present, which begins entirely as seed and evolves with overgrowth precipitation. The mass of seed material used was determined via weighing prior to addition, and the mass of the precipitate is determined from the rate of titrant addition in units of volume per time, taking into account the concentration of Ca in the titrant measured with ICP-OES.

In most experiments, the solids were dominantly (typically >95% of particles) regular and sub-regular rhombohedral particles, and therefore approximated as rhombohedra (or trigonal trapezohedra). However, scanning electron microscope (SEM) images indicate there are also geometries that can be approximated as right pentagonal prisms or, less commonly, dodecahedra. Assuming that a particle is a rhombohedron (or a trigonal trapezohedron), rather than a regular dodecahedron or a right regular pentagonal prism, will predict an SSA that is comparatively 50% larger. Because of this discrepancy in SSA, in samples where non-rhombohedral morphologies are noted in fractions exceeding 0.05, we estimate the fractions of these particles from several SEM images and account for their geometries (Table 2).

All experiments have unimodal crystal size distributions skewed to the right (Fig. 5), meaning the mean value is larger than the median. We therefore use the median particle size to capture the representative specific surface area, as the particles do not fall along a normal distribution. With smaller crystals corresponding to larger specific surface areas, selecting the mean rather than the median would result in reporting higher surface normalized rates than is representative of the bulk. Surface areas estimated with geometric approximations are generally lowermost estimates of SSA because they do not include any amount of surface roughness (cf. Morse et al., 2007). Precipitation rates, R_p, are calculated from titration data (mL/s), concentrations of titrants (mol/L), and these surface area estimates (m^2), providing surface normalized growth rates in units of moles/m^2/s.

Ca isotope measurements were performed via thermal ionization mass spectrometry (TIMS) following the methods described in Appendix A of this dissertation. Ca isotope data are reported in delta notation ($\delta_{sample} = 1000\times\left(\frac{R_{sample}}{R_{standard}} - 1\right)$; R = $^{44}Ca/^{40}Ca$) relative to bulk silicate earth (BSE; $^{44}Ca/^{40}Ca$ = 0.0212035; Nielsen and DePaolo, 2013). Replicate measurements of the standard SRM 915A ($^{44}Ca/^{40}Ca$ = 0.02118336) yielded a mean value of -1.05±0.05 (2 s.e., n = 20), with an average 2σ = 0.11. Each Ca isotope sample was measured at least twice on separate filaments and passed a series of quality control checks.

The average fractionation between solid growth and solution is reported using cap-delta notation, or $\Delta^{44/40}Ca$ (often abbreviated $\Delta_{s\text{-}f}$), where $\Delta_{s\text{-}f} = \delta_{solid} - \delta_{fluid}$ at any given point during the experiment. It is not appropriate to determine $\Delta_{s\text{-}f}$ by simply subtracting the final fluid $\delta^{44}Ca$ value from that of the measured solid, because the measured, or bulk solid (after corrected for seed material) is not fairly representative of the final precipitating calcite. Although chemical steady state is maintained throughout the experiments, there is significant evolution of $\delta^{44}Ca$ in both fluids and solids because a large fraction of the original Ca reservoir is consumed (and subsequently replaced with titrant to maintain steady state). As a result, new solid is forming from an increasingly distilled reservoir, and the bulk overgrowth is therefore the *integrated* δ^{44}Ca of calcite precipitated over the entire experiment.

The measured solid can be corrected for the seed material following a mass balance approach, where $\delta_{overgrowth} = (\delta_{bulk} - f_{seed} * \delta_{seed})/f_{overgrowth}$; f_i = mass fraction). This approach assumes the fraction of seed material in the measured solid is that of the larger system, and that the overgrowth is representative of the average precipitate. Once corrected for the seed fraction and composition, this overgrowth composition is assumed to be a reasonable approximation of the average δ^{44}Ca of the precipitate. The corresponding fluid δ^{44}Ca is given by the mean of the final and initial fluids. Then, $\Delta_{s\text{-}f}$ is calculated as the difference between δ^{44}Ca of the bulk overgrowth and the mean δ^{44}Ca of the fluids.

For comparison to these calculated averages, we estimate the $\Delta_{s\text{-}f}$ values according to Equation 2, using only the initial and final δ^{44}Ca of the fluid reservoir. The $\Delta_{s\text{-}f}$ values for each experiment were calculated numerically to fit the measured δ^{44}Ca of the fluid to within 0.01, using the time-resolved titration curve with Ca measurements of titrants and growth solution. Time steps (dt) were at the resolution of titration data and variable based on experimental duration due to software restrictions. All time steps were shorter than 60 seconds and therefore sufficient to capture individual titrant additions for all experiments. The following equation, similar to those seen in DePaolo (2004) and Nielsen and DePaolo (2013), was used in fitting measured fluid δ^{44}Ca values, assuming steady state conditions with respect to Ca concentrations but accounting for the evolution of fluid δ^{44}Ca in proportion to the titration rate. Equation derivation can be found in Appendix I.

$$\frac{d\delta_{res}}{dt} = \frac{F}{N_{Ca}}(\delta_{in} - \Delta - \delta_{res}) \qquad (2)$$

In Equation 2, δ_{res} is the fluid δ^{44}Ca in the reservoir and δ_{in} is the fluid δ^{44}Ca in the titrant. F is the titrant addition flux in units of moles per time, which is equal to the moles per unit time of Ca uptake due to calcite precipitation. N_{Ca} is equal to the number of moles of Ca in the reservoir.

The error on measurements of δ_{in} (titrant/initial growth solution), δ_{final} (final fluid), and titrant concentration are included in reported uncertainty of $\Delta_{s\text{-}f}$. The δ^{44}Ca of the stock solutions used in preparing the titrant and growth solution (and therefore serving as the "input fluid" in Equation 2) were each measured three times, yielding values of 0.02±0.10 for experiments E2T2, Exp1, and Exp3, and 0.16±0.06 for all others. The δ^{44}Ca of seed material was 0.01±0.09 for all experiments.

3. Results & discussion

3.1 Morphology and specific surface area (SSA)

The specific surface area of seed material (Fig. 3a) was determined to be 0.45±0.1 m^2/g. Specific surface area (SSA) calculated for all particles (Table 2) averages 1.53±0.34 m^2/g and does not correspond to Mg/Ca ratio in solution. While BET surface area measurements (Brunauer et al., 1938) were not possible with the small amount of precipitate produced, it has been shown that surface areas determined via BET for euhedral calcite rhombs do agree closely with those estimated using a geometric surface area approximation (Morse, 1983). However, it is likely that our calculated SSA values are lowermost estimates of overgrowth SSA (cf. Morse et al., 2007), as geometric approximations do not take into account surface roughness that is observed in many of our samples due to the addition of Mg. Consequently, surface-normalized rates are uppermost estimates. Calculated specific surface areas of overgrowth are a factor of 3-8x higher than pure calcite grown experimentally at similar rates (Watkins et al., 2013; Tang et al., 2008b), demonstrating that Mg has a material effect on crystal size distribution, even at low Mg/Ca ratios.

Trial	Rhomb. SSA (m^2/g)	Non-rhomb. frac.	Corr. SSA (m^2/g)
E0T3	1.38 ± 0.18	0.00	-
E7T1	1.29 ± 0.15	0.20	1.16
E7T3	1.72 ± 0.27	0.25	1.50
E4T1	1.42 ± 0.12	0.10	1.35
E4T2	1.32 ± 0.16	0.10	1.25
E6T1	1.74 ± 0.16	0.50	1.30
E2T2	1.36 ± 0.13	<0.05	-
E2T3	1.33 ± 0.14	<0.05	-
E5T1	2.13 ± 0.26	0.10	2.02
E8T1	2.16 ± 0.19	<0.05	-
E3T1	1.15 ± 0.16	<0.05	-
E0T4	1.17 ± 0.21	0.00	-
E1T4	1.73 ± 0.37	<0.05	-
Exp1	0.88 ± 0.13	<0.05	-
Exp3	1.43 ± 0.22	<0.05	-
Seed	0.45 ± 0.10	0.00	-

Table 2. Specific surface areas used in rate calculations. Rhombohedron SSA assumes all particles are rhombohedra. Corrected SSA accounts for precipitate containing >5% estimated non-rhombohedral particles with lower SSA. Fractions estimated in third column.

SEM images of Mg-calcite precipitates reveal highly aggregated crystals, sometimes of varying habit, and regular as well as irregular rhombs. We observe that Mg demonstrably increases growth of certain crystal faces not expressed in classic rhombohedral calcite (Zhang and Dawe, 2000; Jimenez-Lopez et al., 2004; Meldrum and Hyde, 2001), which was surprisingly not observed in the low-Mg calcite grown by Mavromatis et al. (2013). While there are some instances of nearly anhedral precipitation in the slightly more rounded-type aggregates from experiment E5T1 (Fig. 3e), these are not found in most other cases. There is no apparent correlation between either the variance in the crystal size distributions or the shape of the distributions (Fig. 5) and any other measurable parameter.

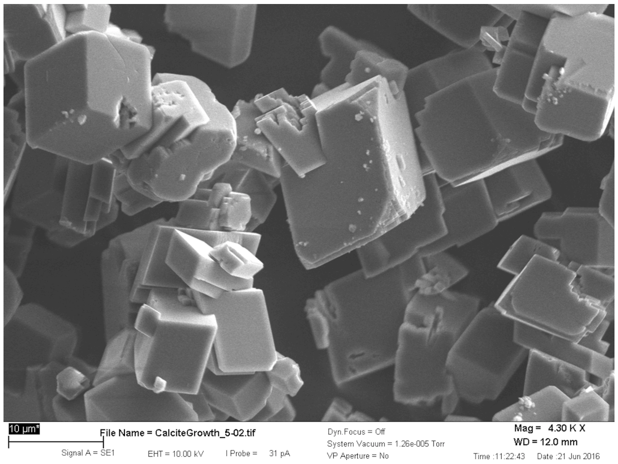

Figure 3a. Scanning electron microscope image of calcite seed. (Scale bar = 10µm)

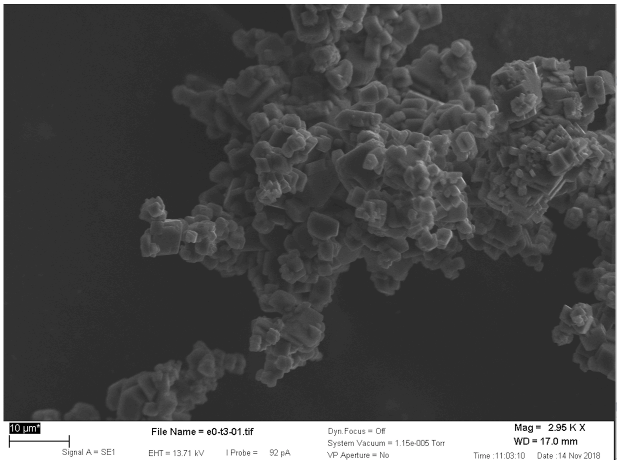

Figure 3b. Scanning electron microscope image of material from experiment E0T3, $(Mg/Ca)_{fl} = 0$. (Scale bar = 10µm)

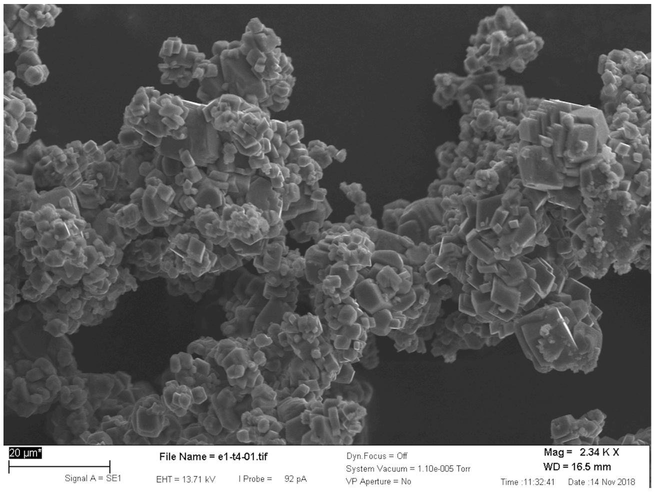

Figure 3c. Scanning electron microscope image of material from experiment E1T4, $(Mg/Ca)_{fl} = 0.07$. (Scale bar = 20μm)

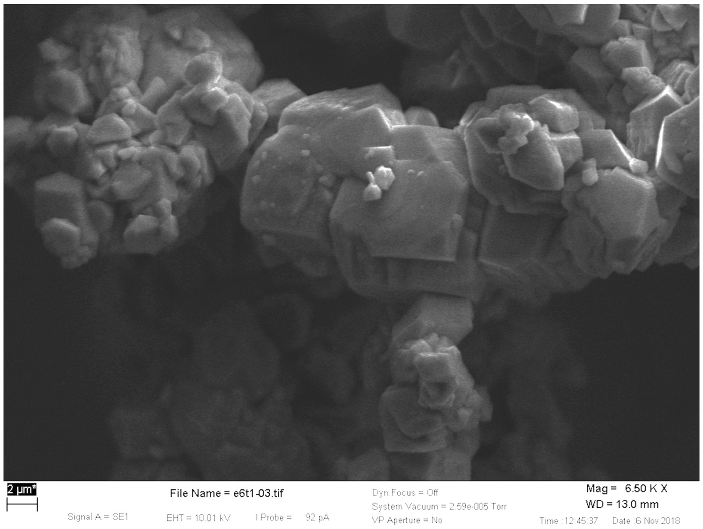

Figure 3d. Scanning electron microscope image of material from experiment E6T1, $(Mg/Ca)_{fl} = 0.36$. (Scale bar = 2μm)

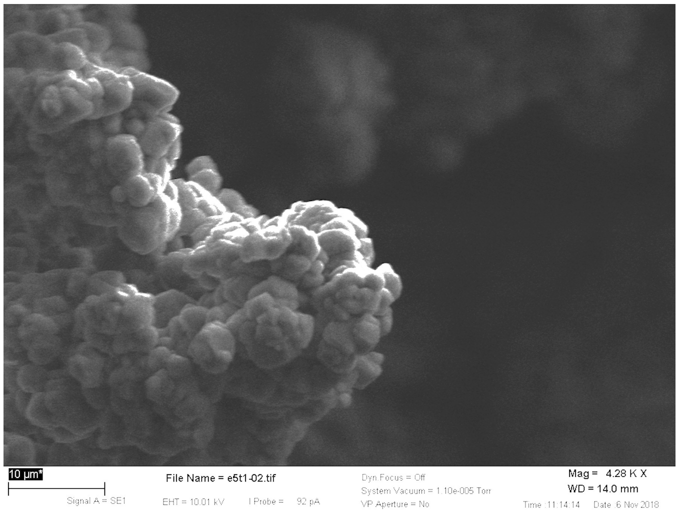

Figure 3e. Scanning electron microscope image of material from experiment E5T1, $(Mg/Ca)_{fl} = 0.6$. (Scale bar = 10μm)

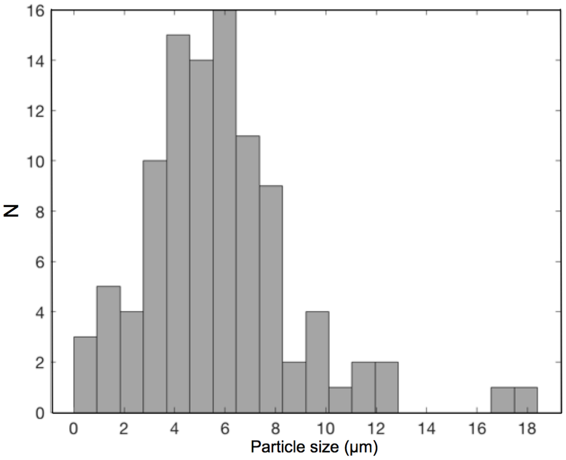

Figure 4. Crystal size distribution of seed material. N = number of particles. Particle size is edge length of approximated rhombohedron.

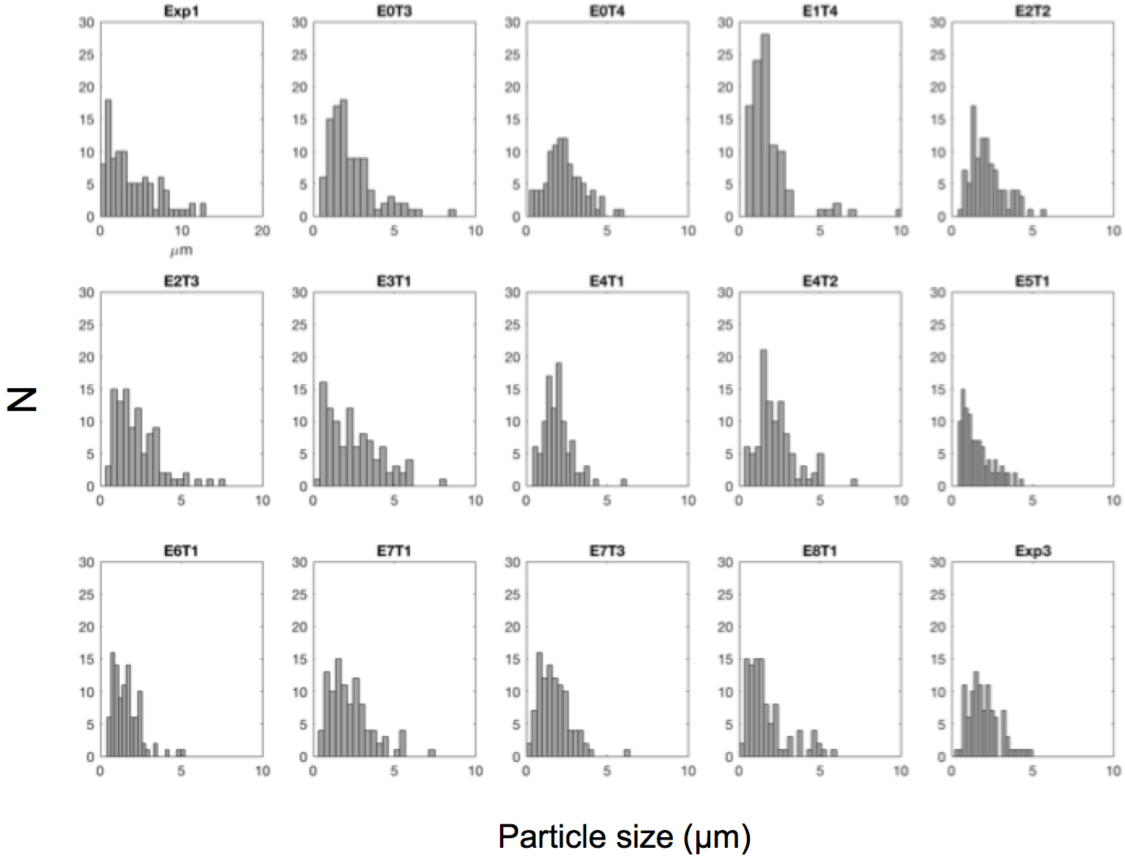

Figure 5. Crystal size distributions from experimental trials. For each trial, 100 crystals were analyzed with 20 bins in each histogram. N = number of particles. Particle size is edge length of approximated rhombohedron. Note that the x-axis for Exp1 extends to 20, while all others have an upper limit of 10.

3.2 Partition coefficients (K_{Mg})

Calculated partition coefficients for experiments of Mg/Ca > 0 are shown in Figure 6. There does not appear to be any rate dependence, which is consistent with most other Mg-calcite precipitation studies (e.g., Katz, 1973; Mucci and Morse, 1983; Mucci 1986; Mucci 1987; Morse and Bender, 1990; Rimstidt et al., 1998), with few exceptions (Mavromatis et al., 2013; Gabitov et al., 2014). Experiments performed with baffles have an average K_{Mg} of 0.0461±0.0160 when overgrowth fractions (Table 1) are assumed to be the same in measured solids as they are in the bulk. Assuming only Mg-calcite overgrowth (and no seed) is included in the measurements, values do not deviate significantly from the estimates assuming the presence of seed. If the two baffle-free experiments performed at lower SI are included, there may be a SI dependence or very weak rate dependence, but we cannot determine this with the present dataset. The average K_{Mg} calculated falls within the range observed in the literature for experimental studies, which is approximately 0.012 to 0.057 (Mucci and Morse, 1983; Oomori et al., 1987; Katz, 1973; Rimstidt et al., 1998; Mavromatis et al., 2013), although most of these studies found K_{Mg} values on the lower end of this range. It should be noted that due to the poorly constrained fraction of overgrowth measured via bulk digestion, the data shown in Fig. 6 are low estimates. However, higher values of K_{Mg} would not significantly impact our interpretation.

Trial	f_{OG}	mg seed	total hr	SI calcite	avg Ca (mM)	avg Mg (mM)	avg Alk (mM)	a(Ca^{2+}/CO_3^{2-})	a(Ca^{2+})	a(Mg^{2+})
E0T3	0.74	91	8	0.59	4.0	0.0	3.3	87.7	1.00E-03	0
E7T1	0.87	94	23	0.54	3.6	0.7	3.3	78.9	9.02E-04	2.03E-04
E7T3	0.84	96	18	-	-	-	-	-	-	-
E4T1	0.82	97	23	0.69	5.3	1.1	3.2	120.5	1.32E-03	3.18E-04
E4T2	0.75	97	21	0.57	4.0	1.2	3.2	90.6	1.00E-03	3.48E-04
E6T1	0.76	93	20	0.56	3.8	1.4	3.3	83.4	9.50E-04	4.06E-04
E2T2	0.88	59	66	0.55	3.7	1.7	3.3	81.2	9.24E-04	4.92E-04
E2T3	0.87	98	45	0.57	3.9	1.9	3.3	85.7	9.74E-04	5.50E-04
E5T1	0.75	96	32	0.56	3.8	2.3	3.3	83.6	9.48E-04	6.66E-04
E8T1	0.76	97	139	-	-	-	3.4	-	-	-
E3T1	0.71	92	285	0.59	4.1	3.9	3.3	90.6	1.02E-03	1.13E-03
E0T4	0.93	96	16	0.49	3.2	0.0	3.3	69.9	8.02E-04	0
E1T4	0.90	98	25	0.66	5.4	0.4	2.9	135.4	1.35E-03	1.16E-04
Exp1	0.76	144	1492	0.19	1.6	1.4	3.3	34.9	4.01E-04	4.07E-04
Exp3	0.72	1303	481	0.57	3.9	1.0	3.3	85.5	9.75E-04	2.90E-04

Table 1. Trial details. Fraction of overgrowth (f_{OG}), mass of seed, experiment duration, saturation index of solution with respect to calcite, average Ca, Mg, alkalinity, activity ratio of Ca/CO_3, and activities (a) of Ca and Mg. Saturation indices and activities calculated using PhreeqC.

The experiments performed by Mucci and Morse (1983) in seawater-like solutions indicate that Mg partitioning depends on the Mg/Ca ratio in solution, which is also suggested by others (Morse and Bender 1990; Berner 1975). However, a dependence on the Mg/Ca ratio in solution would also be seen in the data as a rate dependence, as these two parameters are strongly correlated (Fig. 7), and rate-controlled K_{Mg} is not supported by our observations. While the K_{Mg} values in this study are not necessarily inconsistent with a temperature dependence, they are still ~2-5x higher than most inorganic calcite precipitation at 25°C (Katz, 1973; Burton and Walter, 1987; Oomori et al., 1987; Lopez et al., 2009), and more than two orders of magnitude higher than the inferred equilibrium values observed in deep-sea authigenic calcite (Lammers and Mitnick, *in press*). Although the temperature in the sediment core at depths pertaining to the samples studied by Lammers and Mitnick (*in press*) is approximately 10°C, it is unlikely that an increase of 15°C could shift the equilibrium K_{Mg} by more than a factor of 5 or so.

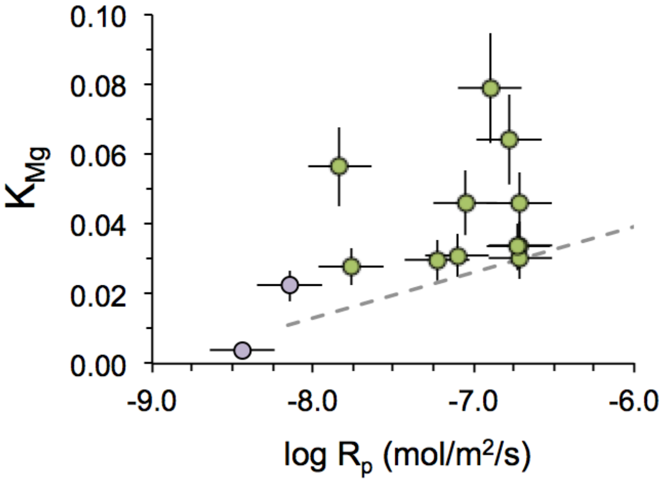

Figure 6. Calculated partition coefficients (K_{Mg}) for all experiments with Mg/Ca > 0. Purple circles = no baffles; Green = baffles; Upper error bounds are not well constrained given unknown amount of seed in digested solid. Grey dashed line represents rate dependence observed by Mavromatis et al. (2013).

The relatively large variation in K_{Mg} values of our experiments are difficult to explain given the small inter-experimental variations other than fluid Mg/Ca ratios. The most likely explanation is that variations in expression of different crystal faces observed among experiments, and the preferential incorporation of Mg on specific faces (Paquette and Reader, 1990; Paquette and Reader, 1995; Jimenez-Lopez et al., 2004) may be the cause of the spread in our data. High-resolution element mapping of our experimental samples coupled with an accounting of the expression of specific crystal face distribution could help address this hypothesis. The expression of certain crystal faces, as discussed in Section 3.1, has implications for understanding Mg partitioning, as previously established (e.g., Paquette and Reeder, 1990; Paquette and Reeder, 1995; Zhang and Dawe, 2000) due to preferential attachment of Mg to specific growth steps and consequently specific faces. Accordingly, although Mg partitioning may not be correlated with bulk growth rate, we propose that it is likely correlated with surface normal growth rates on Mg-preferred faces. Paquette and Reeder (1990) demonstrated that Mg partitioning can increase by a factor of four depending on morphology. Additionally, changes in crystal face expression also have been shown to differ under the same Mg/Ca ratios at different temperatures (e.g., Zhang and Dawe, 2000), which may have important implications for cross-species variation in K_{Mg} and utilization of the Mg/Ca temperature proxy in both biological and inorganic calcite.

3.3 Possible influence of ionic strength and background electrolyte on K_{Mg}

Step propagation rates (and consequently growth rates) are mostly independent of ionic strength (Zuddas and Mucci, 1998; Stephenson et al., 2011; Hong and Teng, 2014), but work by Stephenson et al. (2011) demonstrated that relative propagation rates of acute and obtuse steps are a function of the specific background electrolyte. NaCl as a background electrolyte, which was used in the present study, has interesting implications for Mg attachment and site availability (Ruiz-Agudo et al., 2010). While overall, high ionic strength is associated with less Mg incorporation due to increased kink blocking, sodium ions are thought to increase the total amount of Mg incorporated in comparison to cations of other electrolyte solutions (Stephenson et al., 2011). This consequence of Na-Mg surface interactions seems counter-intuitive, as Mg and Na both preferentially attach to acute steps when calcite growth is controlled by surface reactions (Stephenson et al., 2011; Wasylenki et al., 2005). With both Mg and Na preferring acute step attachment, one might expect the result of this competition to be an overall decrease in the amount of Mg adsorbed and subsequently incorporated. However, because the kink blocking slows acute step propagation, more of the bulk crystal is formed via ion attachment at acute steps, and the overall effect of NaCl with Mg *compared to* other electrolytes is that relatively more Mg will be incorporated (Stephenson et al., 2011). These dynamics may not be solely responsible for determining K_{Mg}, as is obvious by the large range of values found among experiments with Mg/Ca > 0 and ionic strength close to that of seawater. However, it is likely an important control on K_{Mg}.

3.4 Net precipitation rates (R_p)

All experiments at the same SI for calcite show decreasing rates as a function of aqueous Mg/Ca ratio (Fig. 7), as expected based on numerous other studies (e.g., Bischoff, 1968; Berner, 1975; Mucci and Morse, 1983; Zuddas and Mucci, 1994; Lin and Singer, 2009; Davis et al., 2000; Zhang and Dawe, 2000; Wasylenki et al., 2005; Astilleros et al., 2010). Growth rates from four of our experiments of higher Mg/Ca are significantly lower than previous experiments in which Ca isotopes were measured with values less than 10^{-8} mol/m^2/s, allowing us to sample rates that may be slow enough to express the equilibrium $\Delta^{44/40}$Ca.

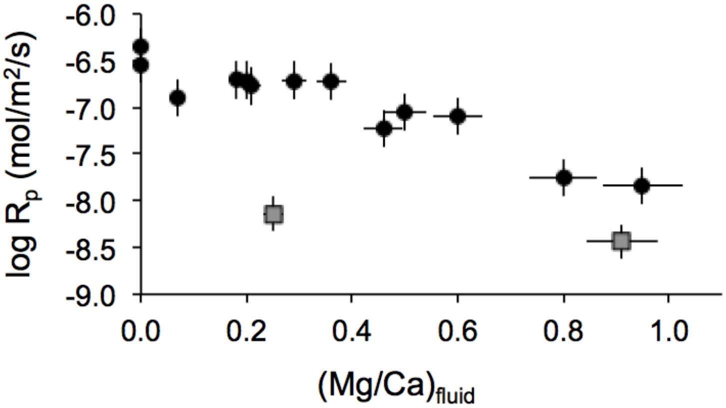

Figure 7. Precipitation rates of all experiments shown as a function of Mg/Ca ratio (mol/mol) in growth solution. Experiments performed without baffles shown in grey.

The relationship between precipitation rate and Mg/Ca solution ratios that we determined generally agree with the data of Mucci and Morse (1983), who grew inorganic calcite with varying Mg/Ca in modified seawater solutions (Fig. 8). However, our data have a slightly stronger dependence, which is apparent at Mg/Ca of approximately 1, where our rate curve diverges from that of Mucci and Morse (1983). Berner (1975) observed that the dependence of precipitation rate on Mg/Ca in solution is a function of saturation index, which likely accounts for this disparity. Still, the comparison between experiments done in seawater-like solutions versus our relatively simple $CaCl_2$-$MgCl_2$-$NaCO_3$ solutions indicates the dominance of the Mg/Ca rate control. Data of Lin and Singer (2009) and Mavromatis et al. (2013) show a similar Mg/Ca dependence on growth rate to our experiments, with variations likely due to different saturation indices and Ca/CO_3 activity ratios probed (Nielsen et al., 2012).

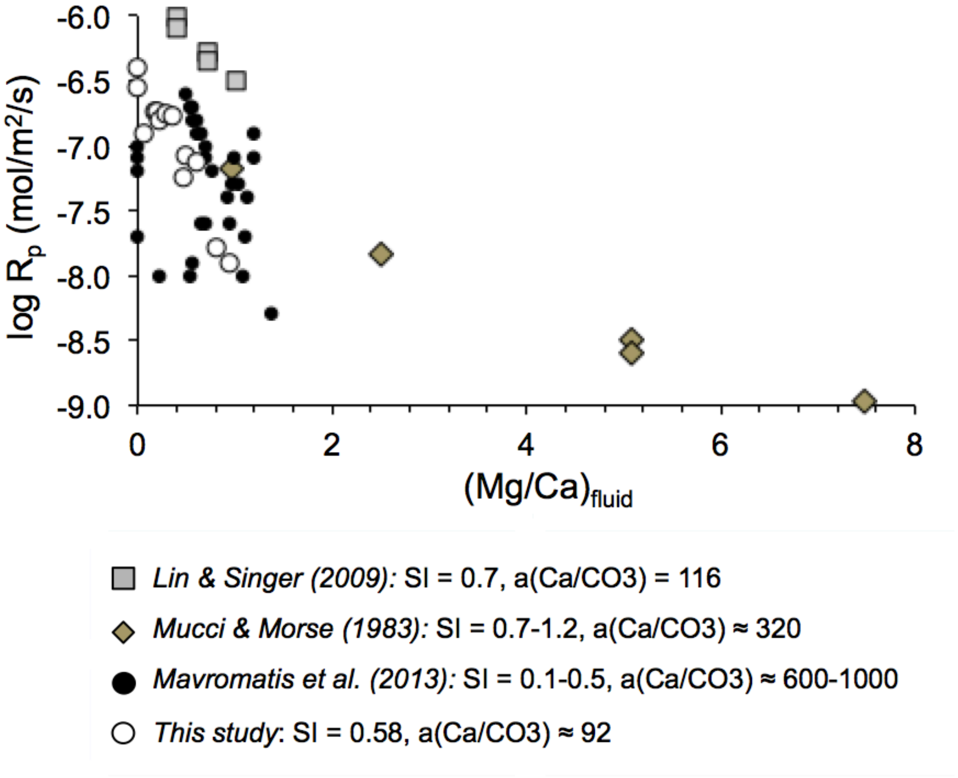

Figure 8. Rate data from all experiments performed with baffles compared to literature values.

3.5 Ca isotopes

3.5.1 δ^{44}Ca and $\Delta^{44/40}$Ca with increasing Mg/Ca and decreasing growth rate

As observed in numerous other experimental studies (e.g., LeMarchand et al., 2004; Tang et al., 2008b, Tang et al., 2012; AlKhatib and Eisenhauer, 2017) and as predicted by kinetic models (DePaolo, 2011; Nielsen et al., 2012), our data also show that the light isotope is preferentially incorporated into the solid during growth. A significant fraction of the initial Ca in the reservoir is precipitated, and consequently there is an evolution of the fluid δ^{44}Ca to heavier values as the light isotope is scavenged by the growing calcite. Consistent with slower growing calcite consuming less of the total Ca reservoir, experiments at low Mg/Ca ratios and higher growth rates have the heaviest final fluid δ^{44}Ca, with slowly growing calcite at higher Mg/Ca ratios having the smallest increase in δ^{44}Ca (Table 3; Fig. 9). The largest magnitude fractionation we observe (-1.32±0.14) is from a Mg-free experiment, E0T3, corresponding to a precipitation rate of $10^{-6.35}$ mol/m^2/s (Fig. 10). The smallest magnitude fractionation (-0.57±0.20) from Exp1 with Mg/Ca of 0.91 corresponds to a precipitation rate of $10^{-8.14}$ mol/m^2/s. The data show that as Mg/Ca ratios increase and rate decreases correspondingly (Fig. 10), the magnitude of the observed fractionation becomes smaller.

Class.	Trial	fluid Mg/Ca	X_{Mg}	log R_p	δ^{44}Ca final fluid	δ^{44}Ca bulk solid	$\Delta^{44/40}$Ca
SS	E0T3	0.00	-	-6.35	0.70 ± 0.10	-0.66 ± 0.10	-1.32 ± 0.14
SS	E7T1	0.18	0.0061 ± 0.0007	-6.71	0.98 ± 0.09	-0.21 ± 0.13	-0.81 ± 0.17
SS	E7T3	0.20	0.0060 ± 0.0007	-6.78	-	-	-
SS	E4T1	0.21	0.0133 ± 0.0016	-6.71	0.74 ± 0.13	-0.50 ± 0.18	-1.06 ± 0.21
SS	E4T2	0.29	0.0131 ± 0.0016	-6.72	0.42 ± 0.06	-0.57 ± 0.17	-1.05 ± 0.19
SS	E6T1	0.36	0.0119 ± 0.0014	-7.23	0.66 ± 0.08	-0.55 ± 0.09	-1.13 ± 0.13
SS	E2T2	0.46	0.0135 ± 0.0016	-7.05	0.74 ± 0.09	-0.61 ± 0.11	-1.07 ± 0.16
SS	E2T3	0.50	0.0225 ± 0.0027	-7.10	0.72 ± 0.04	-0.38 ± 0.04	-0.88 ± 0.11
SS	E5T1	0.60	0.0183 ± 0.0022	-7.76	0.35 ± 0.11	-0.41 ± 0.14	-0.80 ± 0.18
SS	E8T1	0.80	0.0218 ± 0.0026	-7.83	0.49 ± 0.10	-0.24 ± 0.06	-0.64 ± 0.12
SS	E3T1	0.95	0.0509 ± 0.0061	-6.54	0.21 ± 0.10	-0.48 ± 0.05	-0.86 ± 0.11
non-SS	E0T4	0.00	-	-6.90	1.09 ± 0.05	-0.14 ± 0.06	-0.78 ± 0.12
non-SS	E1T4	0.07	0.0055 ± 0.0007	-8.44	0.84 ± 0.15	-0.51 ± 0.12	-1.07 ± 0.18
no baffles, SS	Exp1	0.91	0.0036 ± 0.0004	-8.14	0.28 ± 0.13	-0.32 ± 0.16	-0.57 ± 0.20
no baffles, non-SS	Exp3	0.25	0.0056 ± 0.0007	-6.35	0.63 ± 0.07	-0.21 ± 0.14	-0.62 ± 0.17

Table 3. Trial results. Measured fluid δ^{44}Ca, description, Mg/Ca molar fluid ratio, mole fraction Mg, and calculated rates for all experiments using either corrected SSA from Table 2, or Rhomb. SSA where the non-rhomb fraction was <0.05. Trials not included were ones in which stable growth conditions could not be maintained, or other errors occurred. Solids from experiments E0T3 and E0T4 had Mg concentrations below detection.

Calculated $\Delta_{s\text{-}f}$ values (Fig. 10) align with the compiled data (Fig. 11) of Tang et al. (2008b), Tang et al. (2012), AlKhatib and Eisenhauer (2017), and Watkins et al. (2013). There is also no significant difference observable in the rate-dependence seen in experiments without baffles in comparison to those with baffles, or those considered non-steady state in comparison to those in which steady state was maintained (Fig. 10). In comparison to other studies (Fig. 11), most of our experiments show a larger magnitude fractionation at the same rates. However, the present dataset cannot conclusively demonstrate if this is an artifact of how $\Delta^{44/40}$Ca values were determined, as discussed in the next sections.

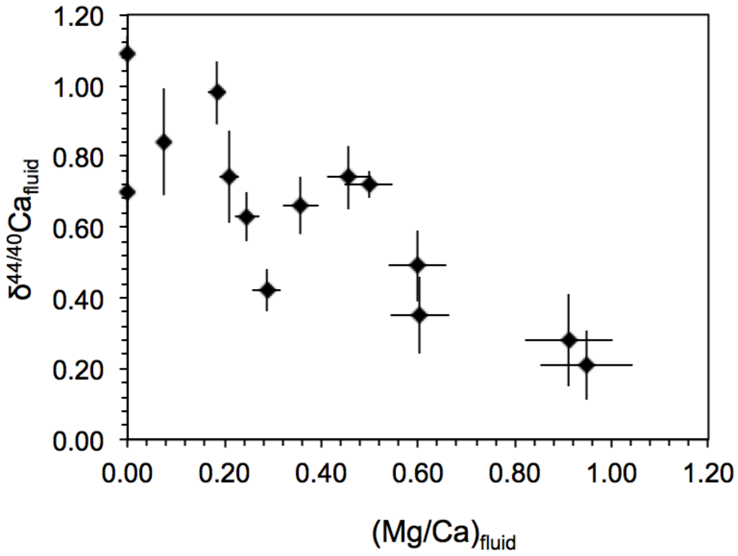

Figure 9. δ^{44}Ca of fluid shown as a function of Mg/Ca solution ratio (mol/mol).

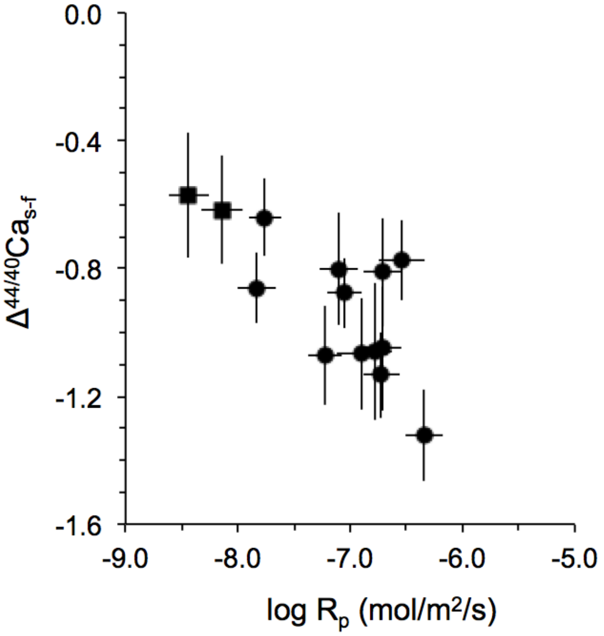

Figure 10. Ca isotope fractionation between solid overgrowth and fluid reported as a function of precipitation rate calculated using bulk solid and average fluid δ^{44}Ca for each experiment. Circles are experiments with baffles; Squares were performed without baffles.

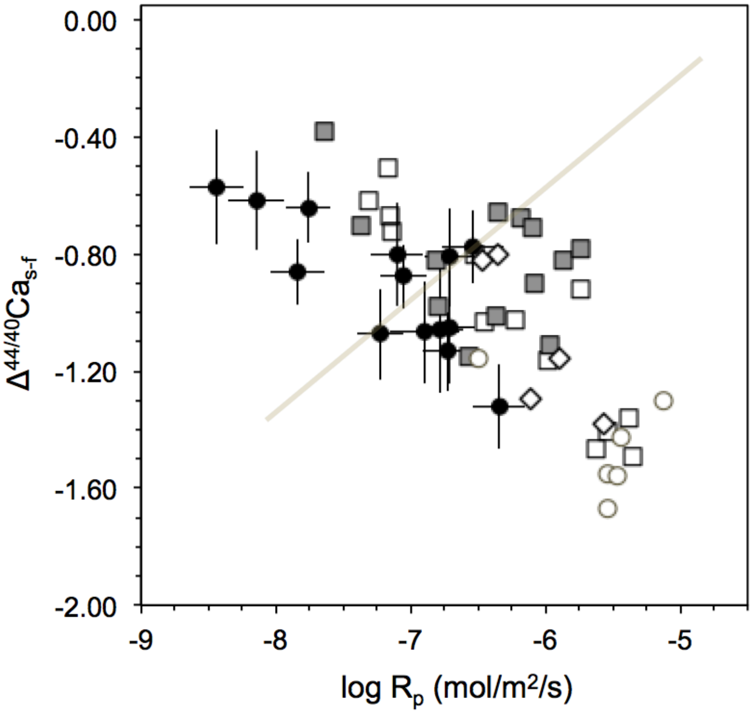

Figure 11. Compilation of $\Delta_{s\text{-}f}$ values in experimentally grown calcite at 25°C from the literature plotted with results from this study (solid line = LeMarchand et al., 2004; open squares = Tang et al., 2008b; filled squares = Tang et al., 2012; open circles = AlKhatib and Eisenhauer, 2017; open diamonds = Watkins et al., 2017; filled circles = this study).

3.5.2 Interpreting $\Delta^{44/40}$Ca in framework of a surface kinetic model

As discussed previously, Mg serves to decrease precipitation rates of calcite due to kink blocking. Since our experiments were performed at constant Ca/CO_3 and SI with respect to calcite, we are able to isolate effects of Mg on $\Delta^{44/40}$Ca. We interpret these data in the framework of the surface kinetic model by DePaolo (2011), who demonstrated that the isotopic fractionation between solids and solution can be expressed as a function of the ratio between backward (R_b) and forward (R_f) gross rates, according to Equation 3.

$$\alpha_p = \frac{\alpha_f}{1+\frac{R_b}{R_f}\left(\frac{\alpha_f}{\alpha_{eq}}-1\right)} \quad [3]$$

The fractionation factor, $\alpha_{s\text{-}f,}$ is related to $\Delta_{s\text{-}f}$ by the approximation $\Delta_{s\text{-}f} \cong 10^3 * (\alpha_{s\text{-}f}$ -1), where $\alpha_{s\text{-}f} = (1000 + \delta_{solid}) / (1000 + \delta_{fluid})$. The fractionation factors in Equation 3 are as follows: α_p = fractionation factor between solid and fluid during surface-controlled precipitation; α_f = kinetic fractionation factor; α_{eq} = equilibrium fractionation factor. R_b is the gross backwards rate, and R_p is the net precipitation rate (where $R_p = R_f - R_b$). While the equilibrium and kinetic fractionation end members could fall within a range of values (0.9985±0.0005 and 1.0000±0.0005), we can use estimates of these values based on our data as well as other experimental and field studies. The model predicts that as equilibrium is approached and R_f/R_b gets closer to unity, the magnitude of the fractionation between the precipitating solid and ambient solution decreases. This behavior is depicted in Fig. 12 for different kinetic and equilibrium fractionation factors.

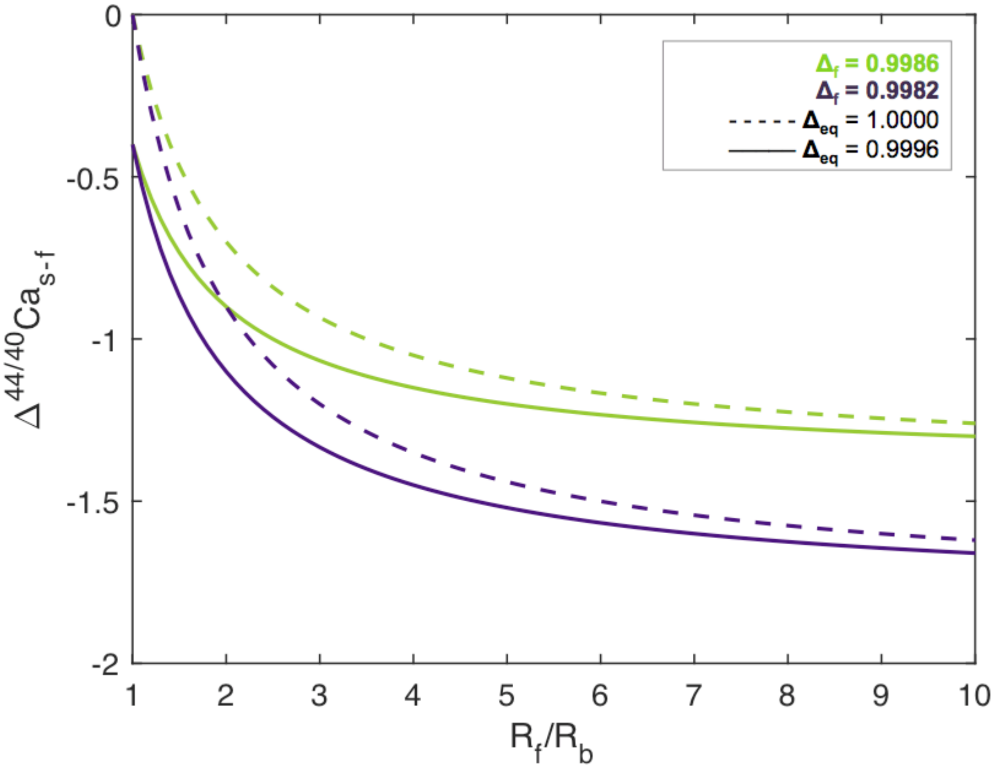

Figure 12. Ca isotope fractionation shown as a function of R_f/R_b ratios, given by Equation 3. Equilibrium is where $R_f/R_b = 1$. Light green and dark purple indicate kinetic fractionation factors α_f of 0.9986 and 0.9982, respectively, while dashed and solid lines indicate equilibrium fractionation α_{eq} of 1.0000 and 0.9996, respectively.

Following an affinity-type rate model where the net precipitation rate R_p is proportional to Ω-1 (where $\Omega = 10^{SI}$), DePaolo (2011) posits that the rate constant is equivalent to the gross backwards rate, R_b. Given that $R_p = R_f - R_b$, which can also be written $R_p = R_b(R_f/R_b - 1)$, this implies that R_f/R_b is proportional to Ω, and consequently, a constant Ω (or SI) corresponds to a constant R_f/R_b. While past studies varied SI in order to probe different precipitation rates, we held SI constant while varying solution Mg/Ca ratios. Our data therefore demonstrate that R_f/R_b can vary independently of the saturation index.

The Ca isotope data indicate that R_f/R_b decreases with decreasing R_p due to the addition of Mg. Experiments E0T3 and Exp1 grew at surface-normalized precipitation rates of $10^{-6.35}$ and $10^{-8.14}$ mol/m^2/s, respectively, corresponding to $\Delta^{44/40}$Ca of -1.32±0.14 and -0.57±0.20. Depending on the kinetic and equilibrium fractionation factors, this difference in $\Delta^{44/40}$Ca could correspond to a decrease in R_f/R_b from approximately 4 to 1.5 (Fig. 12). According to the equation $R_p = R_b(R_f/R_b - 1)$, a decrease in approximately two orders of magnitude in R_p and only a factor of 2-3 in R_f/R_b means that the forward gross rate, R_f, is decreasing considerably faster than the backwards rate, R_b, by at least a factor of 4-5. In other words, as more Mg is added, the decrease in the rate of Ca attachment is much greater than the corresponding decrease in Ca detachment rate. This suggests that R_f exerts a stronger control on Ca isotope fractionation than R_b.

Fitting the DePaolo (2011) model to our experimental data allows us to estimate possible values for the kinetic and equilibrium fractionation factors as well as the Ca detachment flux. We estimate values of R_b to meet the following criteria: (1) R_f/R_b decreases from 2.50 to 1.02 over the R_p values obtained in our experiments, where R_f decreases at a faster rate than R_b, (2) R_b changes with R_p, and (3) R_b for our experiment performed at $R_p = 10^{-6.35}$ mol/m^2/s without Mg is of a similar magnitude to that predicted by Chou et al. (1989) at the given pH and temperature (Fig 13). We find that the best fit to our data is found with variable R_b as a function of R_p, where $\log R_b = 0.095 * \log R_p - 6.181$, and the end-member fractionation factors are 0.9983 and 0.9995 (Fig. 13).

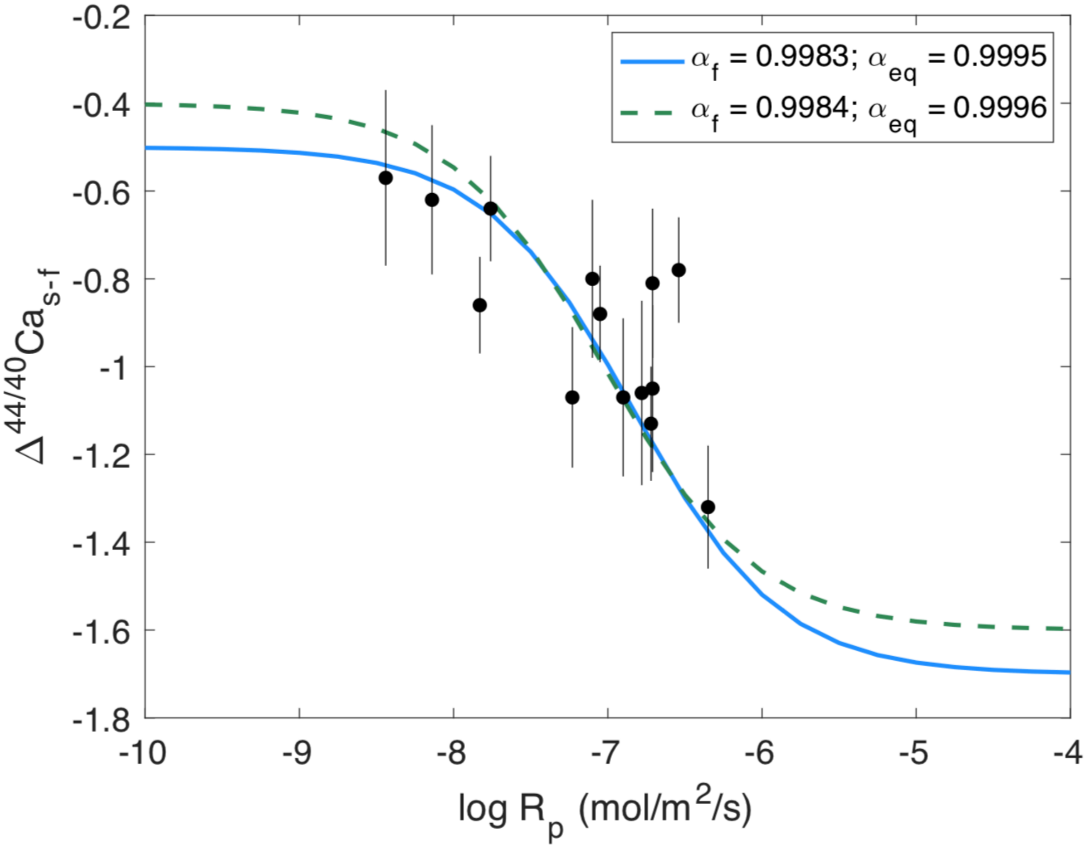

Figure 13. Data from this study (black markers) shown in relation to model curves of Equation 3 using variable R_b, where $\log R_b = k * \log R_p - 6.181$ (k = 0.095 and 0.120 for solid blue and dashed green lines, respectively). Values used for the kinetic and equilibrium fractionation factors are shown in the legend.

Another reasonable fit is found with $\log R_b = 0.120 * \log R_p - 6.181$ and corresponding kinetic and equilibrium fractionation factors of 0.9984 and 0.9996 (Fig. 13). The values of R_b at $R_p = 10^{-6.35}$ mol/m^2/s are found to be $10^{-6.78}$ and $10^{-6.94}$ mol/m^2/s, which are close to, although smaller than, the value determined experimentally by Chou et al. (1989) of $10^{-6.22}$ mol/m^2/s of pure calcite. To fit the value determined by Chou et al. (1989) exactly implies that $\log R_b = 0.026 * \log R_p - 6.181$, which in turn requires that R_f/R_b decreases over a much smaller range, from 1.75 to 1.01. Given the kinetic fractionation factors that best fit the data, it is likely that the maximum R_f/R_b is no smaller than 2 and therefore the reverse fluxes are approximately a factor of 5 lower than Chou et al. (1989) determined for pure calcite.

These results are qualitatively consistent with those of Nielsen et al. (2013), who compared the detachment rates of Ca in Mg-calcite to those in pure calcite and found that with increasing mole fractions of Mg (X_{MgCO3}), this ratio decreased to values less than one. In the X_{MgCO3} range of overgrowth in this study (approximately 0 to 0.05), we do not observe a correlation between X_{MgCO3} and estimated R_b. Based on the calculations from Nielsen et al. (2013), the ratio of detachment rates for Mg-calcite to pure calcite does not decrease significantly until X_{MgCO3} values of ~0.1 are reached, which could explain why we do not observe this correlation between X_{MgCO3} and R_b in our samples.

3.5.3 Effects of Mg/Ca on $\Delta^{44/40}$Ca in natural systems

The Mg/Ca ratios probed in our experiments are lower than those in seawater (approximately 5.2) as well as in some marine sedimentary pore fluids, which can reach fluid Mg/Ca ratios of 20 (e.g., Wefer et al., 1998). However, in carbonate-rich marine sediments studied by Fantle and DePaolo (2007), Mg/Ca ratios are approximately 1.7 at depths at which calcite is expected to be in equilibrium with the surrounding pore fluids. In a study of marine sediments by Turchyn and DePaolo (2011), dissolution rates of calcite in sediments containing significant amounts of clays and organic material were found to be 1-3 orders of magnitude slower than in the carbonate-rich sediments studied by Fantle and DePaolo (2007). Although Turchyn and DePaolo (2011) concluded that it was the presence of clays and organics that decreased dissolution rates, higher Mg/Ca ratios observed in sediment pore fluids may have an important role in this as well.

In addition to the implications for inorganic calcite precipitation, our results have interesting implications for calcite formed by marine organisms. Our data suggest that biogenic calcite formed from seawater (Mg/Ca ~5.2) at 25°C should form at rates ~10^{-8} mol/m^2/s or lower and have small magnitude fractionations (approximately -0.5‰). Indeed, Chang et al. (2004) measured $\Delta^{44/40}$Ca in wild foraminifera (including *O. universa* and *G. sacculifer*) of approximately -0.6‰, which implies that it formed at rates ~10^{-8} mol/m^2/s or lower based on our data. Marine organisms are likely not calcifying this slowly given their relatively short lifespans. However, it is possible that the high Ca/CO_3 activity ratios found in seawater (300 or higher) drives the $\Delta^{44/40}$Ca much closer to equilibrium at faster rates than observed in this study (Nielsen et al., 2012). In contrast, other studies such as the experimental culture experiments of Gussone et al. (2003) show fractionations in excess of -1.0 (*O. universa*) and -3.0‰ (*G. sacculifer*) at 20°C, which imply very fast growth rates (>10^{-5} mol/m^2/s). These rates are greater than 3 orders of magnitude faster than predicted based on seawater Mg/Ca ratios of ~5.2, especially at seawater Ca/CO_3 activity ratios. The disagreement between $\Delta^{44/40}$Ca of biogenic and inorganic calcite at expected rates of biomineralization suggests a strong biological influence on calcite growth kinetics, likely due to engineering of fluid composition within test vacuoles of organisms.

3.5.4 Comparison to numerically calculated $\Delta^{44/40}$Ca using only fluid δ^{44}Ca

Many of the modeled $\Delta^{44/40}$Ca values (calculated numerically via Equation 2) closely agree with those determined using the average solid and fluid δ^{44}Ca values (Fig. 14). However, four experiments show a considerably smaller magnitude fractionation when only δ^{44}Ca fluid values are used to calculate $\Delta^{44/40}$Ca. The misfits of ≥0.4‰ cannot be explained by variation in the curvature of the titration curves, nor by the degree of drift in Ca, Mg, or alkalinity. Uncertainty in the composition of the seed material or stock solution is likely not a significant factor in the misfit, as the other data agree relatively well and rely on the same measurements. Theoretically, the $\Delta^{44/40}$Ca can be determined independently of the solid δ^{44}Ca, as the fluid δ^{44}Ca will capture the evolution of the system in response to fractionation if the titrant composition is specified. It is possible that Equation 1 is too simplistic, but this is difficult to explain given that (1) it closely predicts the measured $\Delta^{44/40}$Ca values for most experiments, and (2) there is no correlation in shape of titration curve or degree of Ca-Mg-CO_3 drift between the well- and poorly-fit data. The composition of overgrowth is one of the most uncertain parameters, due to the assumption that the relative fractions of overgrowth and seed in the measured solids are reflecting those of the bulk system. An increase in the fraction of overgrowth (f_{OG}) decreases the magnitude of the fractionation calculated from the average fluid and bulk solid accordingly. However, though this modification diminishes the offset between the two reported $\Delta^{44/40}$Ca values for the misfit data, *even assuming f_{OG} values of 1*, it does not sufficiently decrease the magnitude such that the values agree.

We cannot conclusively determine which method reports the correct $\Delta^{44/40}$Ca for these misfit data, and consequently, we cannot use the present dataset to confidently constrain an equilibrium $\Delta^{44/40}$Ca value. Fantle and DePaolo (2007), Jacobsen and Holmden (2008), and Brown et al. (2013) suggest that the equilibrium $\Delta^{44/40}$Ca value is close to 0. If this is the case, the numerically calculated model fit is in closer agreement with this equilibrium value than the $\Delta^{44/40}$Ca calculated using the bulk overgrowth and average fluid δ^{44}Ca. However, Bradbury and Turchyn (2018) suggest an equilibrium fractionation that is closer to -0.5, which agrees with our values determined using the bulk overgrowth and average fluid δ^{44}Ca. We also cannot conclusively determine if Mg results in a larger magnitude fractionation at a given rate, as discussed previously. Additional experiments at high Mg/Ca ratios (≥ 1) could resolve these uncertainties. However, irrespective of these misfit data, overall directionality remains the same, and the discrepancies do not change our conclusions regarding R_f/R_b and $\Delta^{44/40}$Ca, nor implications for natural systems.

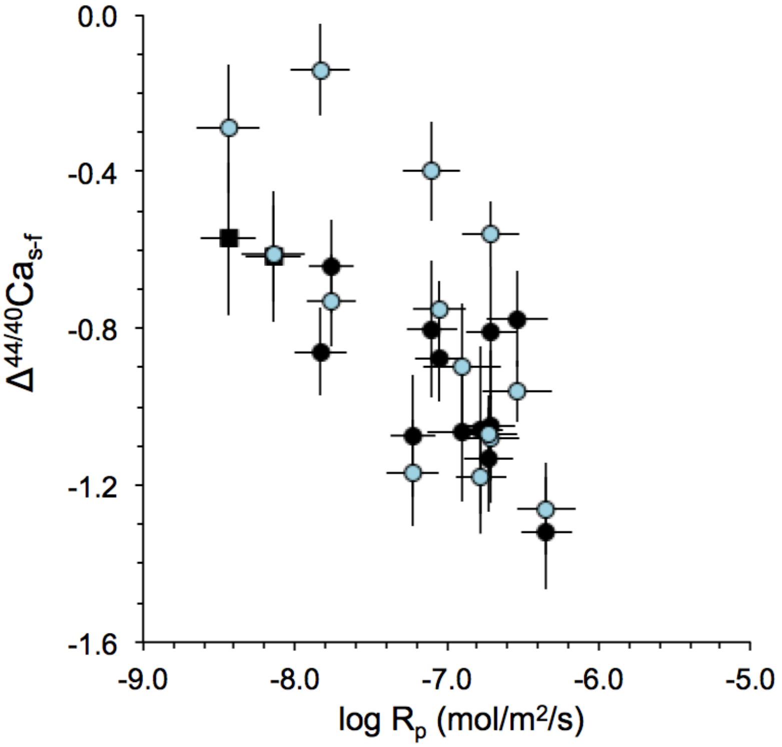

Figure 14. Comparison of results: Ca isotope fractionation between solid overgrowth and fluid reported using initial and final fluid δ^{44}Ca with Equation 2 (blue shaded circles) shown in comparison to those reported as a function of precipitation rate calculated using bulk solid and average fluid δ^{44}Ca for each experiment, as shown in Fig. 10 (black markers).

3.5.5 Reconciling K_{Mg} with Ca isotope data

The significantly higher K_{Mg} values observed in our experiments in comparison to other studies as well as the inferred near-equilibrium values of authigenic carbonate (Lammers and Mitnick, *in press*) are difficult to resolve with the Ca isotope data if the equilibrium fractionation is close to -0.5. While there is a temperature discrepancy between the deep-sea calcite analyzed in Lammers and Mitnick (*in press*) and the temperatures at which the experiments were carried out, it is unlikely this could account for the differences observed, especially in light of the comparatively lower K_{Mg} values from other experimental studies.

We propose that differences in crystallographic face expression and surface area between deep-sea authigenic calcite and our experimental low-Mg calcite could account for the seemingly opposing observations. It is clear that differential expression of specific crystal faces does not change the Ca isotope fractionation in comparison to other studies (Tang et al., 2008b; Tang et al., 2012; AlKhatib and Eisenhauer, 2017), given the variety in morphology observed in this study as compared to those from pure calcite growth experiments (e.g., Watkins et al., 2013; Tang et al., 2008b). However, it may be possible that the crystallographic faces expressed in sub-regular rhombohedra and crystals of other geometries significantly change the amount of incorporated Mg at a given Mg/Ca because of preferred attachment of Mg. Additionally, the rough surfaces and large extent of two dimensional surface-nucleated particles observed in our Mg-calcite could promote increased attachment of Mg.

4. Conclusions

We have used the Ca isotope composition of laboratory-synthesized low-Mg calcite to demonstrate that in addition to the kinetic effect of kink blocking, Mg also slows calcite growth via incorporation inhibition. There is no predicted effect on the ratio of forward (R_f) to reverse (R_b) attachment fluxes of Ca at the calcite surface due to kink blocking alone. Therefore, the decrease in R_f/R_b with decreasing precipitation rate as seen in the isotope data suggests that incorporation inhibition is also a key surface kinetic effect during calcite growth. The change in $\Delta^{44/40}$Ca with precipitation rate at constant saturation index (SI) sampled in our experiments demonstrates that R_f/R_b varies independently of SI. Furthermore, our data indicate that the forward gross rate (R_f) is more strongly dependent on changes in Mg/Ca than R_b.

The K_{Mg} values in our experiments are consistent with previous work demonstrating that there is no rate dependence on Mg partitioning in calcite. The variety of morphologies among experiments suggests a crystallographic influence on Mg partitioning, due to the preference of Mg attaching to specific crystal faces, which may be further pronounced due to the presence of Na.

Our findings have implications for interpreting the behavior of both inorganic and biogenic natural calcite found in marine sediments and the tests of foraminifera. Similar experiments with solutions of Mg >> Ca, at lower ionic strength, as well as those sampling Ca isotope and growth rate effects in more complex solutions should be the priority of future work in order to more robustly apply Ca isotope fractionation proxies to modern marine calcite. Non-incorporating impurities such as polyaspartate should also be tested to probe the isolated effect (or lack thereof) of non-incorporating impurities on Ca isotope fractionation.

Appendix

$$\frac{d}{dt}(\delta_{res}N_{Ca}) = \delta_{in}F_{in} - \delta_{out}F_{out} \qquad \textit{(A1-a)}$$

$$\delta_{res}\frac{dN_{Ca}}{dt} + N_{Ca}\frac{d\delta_{res}}{dt} = \delta_{in}F_{in} - \delta_{out}F_{out} \qquad \textit{(A1-b)}$$

$$\frac{dN_{Ca}}{dt} = F_{in} - F_{out} \qquad \textit{(A1-c)}$$

$$\frac{dN_{Ca}}{dt} = 0;\ F_{in} = F_{out} = F \qquad \textit{(A1-d)}$$

$$N_{Ca}\frac{d\delta_{res}}{dt} = \delta_{in}F_{in} - \delta_{out}F_{out} \qquad \textit{(A1-e)}$$

$$\Delta = \delta_{out} - \delta_{res} \qquad \textit{(A1-f)}$$

Acknowledgements

I am extremely thankful to Holly Barnhart for her enormous contribution in running many experiments, readying samples for Ca isotope measurements in the clean lab, and her positive attitude throughout the many trials we endured to achieve a working setup. Jenny Mills is most gratefully acknowledged for her observations of slow fluid homogenization due to improper stirring and her suggestion to add baffles. I also would like to thank Shaun Brown for assistance with Ca isotope measurements and many helpful conversations, as well as Jim Watkins for his growth apparatus, software, and expertise.

This research was supported by the U.S. Department of Energy, Office of Science, Office of Basic Energy Sciences, Chemical Sciences, Geosciences, and Biosciences Division, under Award Number DE-AC02-05CH11231.

References

AlKhatib, M., & Eisenhauer, A. (2017). Calcium and strontium isotope fractionation in aqueous solutions as a function of temperature and reaction rate; I. Calcite. *Geochimica et Cosmochimica Acta*, *209*, 296-319.

Astilleros, J. M., Fernández-Díaz, L., & Putnis, A. (2010). The role of magnesium in the growth of calcite: An AFM study. *Chemical Geology*, *271*(1-2), 52-58.

Berner, R.A. (1975) The role of magnesium in the crystal growth of calcite and aragonite from sea water. Geochimica et Cosmochimica Acta 39: 489-504.

Bischoff, J. L. (1968). Kinetics of calcite nucleation: magnesium ion inhibition and ionic strength catalysis. *Journal of Geophysical Research*, *73*(10), 3315-3322.

Böhm, F., Gussone, N., Eisenhauer, A., Heuser, A., Haase-Schramm, A., Vacelet, J., ... & Dullo, W. C. (2003). Calcium isotopic composition of marine biogenic carbonates: Influences of mineralogy and biology. In *Geophys. Res. Abstr*(Vol. 5, No. 12,938).

Bradbury, H. J., & Turchyn, A. V. (2018). Calcium isotope fractionation in sedimentary pore fluids from ODP Leg 175: Resolving carbonate recrystallization. *Geochimica et Cosmochimica Acta*.

Brown, S. T., Kennedy, B. M., DePaolo, D. J., Hurwitz, S., & Evans, W. C. (2013). Ca, Sr, O and D isotope approach to defining the chemical evolution of hydrothermal fluids: Example from Long Valley, CA, USA. *Geochimica et Cosmochimica Acta*, *122*, 209-225.

Brunauer, S., Emmett, P. H., & Teller, E. (1938). Absorption of gases in multimolecular layers J Am Chem Soc 60: 309–319

Burton, E. A., & Walter, L. M. (1987). Relative precipitation rates of aragonite and Mg calcite from seawater: Temperature or carbonate ion control?. *Geology*, *15*(2), 111-114.

Plummer, L. N., & Busenberg, E. (1982). The solubilities of calcite, aragonite and vaterite in CO2-H2O solutions between 0 and 90 C, and an evaluation of the aqueous model for the system CaCO3-CO2-H2O. *Geochimica et cosmochimica acta*, *46*(6), 1011-1040.

Chou, L. E. I., Garrels, R. M., & Wollast, R. (1989). Comparative study of the kinetics and mechanisms of dissolution of carbonate minerals. *Chemical geology*, *78*(3-4), 269-282.

Dandekar, P., & Doherty, M. F. (2014). A mechanistic growth model for inorganic crystals: Growth mechanism. *AIChE Journal*, *60*(11), 3720-3731.

Davis, K. J., Dove, P. M., & De Yoreo, J. J. (2000). The role of Mg2+ as an impurity in calcite growth. *Science*, *290*(5494), 1134-1137.

De La Rocha, C. L. & DePaolo DJ, (2000). Isotopic evidence for variations in the marine calcium cycle over the Cenozoic. *Science*, *289*, 1176-1178.

DePaolo, D. J. (2011). Surface kinetic model for isotopic and trace element fractionation during precipitation of calcite from aqueous solutions. *Geochimica et Cosmochimica Acta*, *75*(4), 1039-1056.

DePaolo D. J. (2004) Calcium isotopic variations produced by biological, kinetic, radiogenic and nucleosynthetic processes. In Geochemistry of non-traditional stable isotopes, vol. 55 (eds. C. M. Johnson, B. L. Beard and F. Albarede). Mineralogical Society of America, Geochemical Society, pp. 255–285.

Dobberschütz, S., Nielsen, M. R., Sand, K. K., Civioc, R., Bovet, N., Stipp, S. L. S., & Andersson, M. P. (2018). The mechanisms of crystal growth inhibition by organic and inorganic inhibitors. *Nature communications*, *9*(1), 1578.

Fantle, M. S., & DePaolo, D. J. (2007). Ca isotopes in carbonate sediment and pore fluid from ODP Site 807A: the Ca 2+(aq)–calcite equilibrium fractionation factor and calcite recrystallization rates in Pleistocene sediments. *Geochimica et Cosmochimica Acta*, *71*(10), 2524-2546.

Gabitov, R. I., Sadekov, A., & Leinweber, A. (2014). Crystal growth rate effect on Mg/Ca and Sr/Ca partitioning between calcite and fluid: An in situ approach. *Chemical Geology*, *367*, 70-82.

Gebrehiwet, T. A., Redden, G. D., Fujita, Y., Beig, M. S., & Smith, R. W. (2012). The Effect of the CO 3 2-to Ca 2+ Ion activity ratio on calcite precipitation kinetics and Sr 2+ partitioning. *Geochemical transactions*, *13*(1), 1.

Gussone, N., Eisenhauer, A., Heuser, A., Dietzel, M., Bock, B., Böhm, F., ... & Nägler, T. F. (2003). Model for kinetic effects on calcium isotope fractionation (δ44Ca) in inorganic aragonite and cultured planktonic foraminifera. *Geochimica et Cosmochimica Acta*, *67*(7), 1375-1382.

Gussone N., Bohm F., Eisenhauer A., Dietzel M., Heuser A., Teichert B. M. A., Reitner J., Worheide G. and Dullo W. C. (2005) Calcium isotope fractionation in calcite and aragonite. Geochim. Cosmochim. Acta 69(18), 4485–4494.

Hamm, L. M., Wallace, A. F., & Dove, P. M. (2010). Molecular dynamics of ion hydration in the presence of small carboxylated molecules and implications for calcification. *The Journal of Physical Chemistry B*, *114*(32), 10488-10495.

Hartley, G., & Mucci, A. (1996). The influence of PCO2 on the partitioning of magnesium in calcite overgrowths precipitated from artificial seawater at 25 and 1 atm total pressure. *Geochimica et Cosmochimica Acta*, *60*(2), 315-324.

Higgins, J. A., Blättler, C. L., Lundstrom, E. A., Santiago-Ramos, D. P., Akhtar, A. A., Ahm, A. C., ... & Swart, P. K. (2018). Mineralogy, early marine diagenesis, and the chemistry of shallow-water carbonate sediments. *Geochimica et Cosmochimica Acta*, *220*, 512-534.

Hofmann, A. E., Bourg, I. C., & DePaolo, D. J. (2012). Ion desolvation as a mechanism for kinetic isotope fractionation in aqueous systems. *Proceedings of the National Academy of Sciences*, 201208184.

Hong, M., & Teng, H. H. (2014). Implications of solution chemistry effects: Direction-specific restraints on the step kinetics of calcite growth. *Geochimica et Cosmochimica Acta*, *141*, 228-239.

Jacobson, A. D., & Holmden, C. (2008). δ44Ca evolution in a carbonate aquifer and its bearing on the equilibrium isotope fractionation factor for calcite. *Earth and Planetary Science Letters*, *270*(3-4), 349-353.

Jimenez-Lopez, C., Caballero, E., Huertas, F. J., & Romanek, C. S. (2001). Chemical, mineralogical and isotope behavior, and phase transformation during the precipitation of calcium carbonate minerals from intermediate ionic solution at 25 C. *Geochimica et Cosmochimica Acta*, *65*(19), 3219-3231.

Jimenez-Lopez, C., Romanek, C. S., Huertas, F. J., Ohmoto, H., & Caballero, E. (2004). Oxygen isotope fractionation in synthetic magnesian calcite 1. *Geochimica et Cosmochimica Acta*, *68*(16), 3367-3377.

Katz, A. (1973). The interaction of magnesium with calcite during crystal growth at 25–90 C and one atmosphere. *Geochimica et Cosmochimica Acta*, *37*(6), 1563-1586.

Kerisit, S., & Parker, S. C. (2004). Free energy of adsorption of water and metal ions on the {1014} calcite surface. *Journal of the American Chemical Society*, *126*(32), 10152-10161.

Kile, D. E., Eberl, D. D., Hoch, A. R., & Reddy, M. M. (2000). An assessment of calcite crystal growth mechanisms based on crystal size distributions. *Geochimica et Cosmochimica Acta*, *64*(17), 2937-2950.

Lammers, L.N., & Mitnick, E.H. Magnesian calcite solid solution thermodynamics inferred from authigenic deep-sea carbonate. *Geochimica et Cosmochimica Acta (in press).*

Lemarchand, D., Wasserburg, G. J., & Papanastassiou, D. A. (2004). Rate-controlled calcium isotope fractionation in synthetic calcite. *Geochimica et Cosmochimica Acta*, *68*(22), 4665-4678.

Lin, Y. P., & Singer, P. C. (2009). Effect of Mg2+ on the kinetics of calcite crystal growth. *Journal of Crystal Growth*, *312*(1), 136-140.

Lopez, O., Zuddas, P., & Faivre, D. (2009). The influence of temperature and seawater composition on calcite crystal growth mechanisms and kinetics: Implications for Mg incorporation in calcite lattice. *Geochimica et Cosmochimica Acta*, *73*(2), 337-347.

Lowenstein, T.K., Kendall, B., Anbar, A.D., 2014. The geologic history of seawater. In: Treatise on Geochemistry, second edition. Elsevier Inc.

Mavromatis, V., Gautier, Q., Bosc, O., & Schott, J. (2013). Kinetics of Mg partition and Mg stable isotope fractionation during its incorporation in calcite. *Geochimica et Cosmochimica Acta*, *114*, 188-203.

Meldrum, F. C., & Hyde, S. T. (2001). Morphological influence of magnesium and organic additives on the precipitation of calcite. *Journal of Crystal Growth*, *231*(4), 544-558.

Morse, J. W., Wang, Q., & Tsio, M. Y. (1997). Influences of temperature and Mg: Ca ratio on CaCO3 precipitates from seawater. *Geology*, *25*(1), 85-87.

Morse J. W. (1983) The kinetic of calcium carbonate dissolution and precipitation. In Carbonate: Mineralogy and Chemistry, vol. 11 (ed. R. J. Reeder). Mineralogical Society of America, pp. 227–264.

Morse, J. W., & Bender, M. L. (1990). Partition coefficients in calcite: Examination of factors influencing the validity of experimental results and their application to natural systems. *Chemical Geology*, *82*, 265-277.

Morse, J. W., Arvidson, R. S., & Lüttge, A. (2007). Calcium carbonate formation and dissolution. *Chemical reviews*, *107*(2), 342-381.

Mucci, A. (1986). Growth kinetics and composition of magnesian calcite overgrowths precipitated from seawater: Quantitative influence of orthophosphate ions. *Geochimica et Cosmochimica Acta*, *50*(10), 2255-2265.

Mucci, A. (1987). Influence of temperature on the composition of magnesian calcite overgrowths precipitated from seawater. *Geochimica et Cosmochimica Acta*, *51*(7), 1977-1984.

Mucci, A., & Morse, J. W. (1983). The incorporation of Mg2+ and Sr2+ into calcite overgrowths: influences of growth rate and solution composition. *Geochimica et Cosmochimica Acta*, *47*(2), 217-233.

Nehrke, G., Reichart, G. J., Van Cappellen, P., Meile, C., & Bijma, J. (2007). Dependence of calcite growth rate and Sr partitioning on solution stoichiometry: non-Kossel crystal growth. *Geochimica et Cosmochimica Acta*, *71*(9), 2240-2249.

Nielsen, L. C., De Yoreo, J. J., & DePaolo, D. J. (2013a). General model for calcite growth kinetics in the presence of impurity ions. *Geochimica et Cosmochimica Acta*, *115*, 100-114.

Nielsen, L. C., & DePaolo, D. J. (2013b). Ca isotope fractionation in a high-alkalinity lake system: Mono Lake, California. *Geochimica et Cosmochimica Acta*, *118*, 276-294.

Oomori, T., Kaneshima, H., Maezato, Y., & Kitano, Y. (1987). Distribution coefficient of Mg2+ ions between calcite and solution at 10–50 C. *Marine Chemistry*, *20*(4), 327-336.

Paquette, J., & Reeder, R. J. (1990). New type of compositional zoning in calcite: Insights into crystal-growth mechanisms. *Geology*, *18*, 1244.

Paquette, J., & Reeder, R. J. (1995). Relationship between surface structure, growth mechanism, and trace element incorporation in calcite. *Geochimica et Cosmochimica Acta*, *59*(4), 735-749.

Parkhurst, D. L., & Appelo, C. A. J. (1999). User's guide to PHREEQC (Version 2): A computer program for speciation, batch-reaction, one-dimensional transport, and inverse geochemical calculations.

Rimstidt, J. D., Balog, A., & Webb, J. (1998). Distribution of trace elements between carbonate minerals and aqueous solutions. *Geochimica et Cosmochimica Acta*, *62*(11), 1851-1863.

Romanek, C. S., Grossman, E. L., & Morse, J. W. (1992). Carbon isotopic fractionation in synthetic aragonite and calcite: effects of temperature and precipitation rate. *Geochimica et cosmochimica acta*, *56*(1), 419-430.

Ruiz-Agudo, E., Kowacz, M., Putnis, C. V., & Putnis, A. (2010). The role of background electrolytes on the kinetics and mechanism of calcite dissolution. *Geochimica et cosmochimica acta*, *74*(4), 1256-1267.

Stephenson, A. E., Hunter, J. L., Han, N., DeYoreo, J. J., & Dove, P. M. (2011). Effect of ionic strength on the Mg content of calcite: Toward a physical basis for minor element uptake during step growth. *Geochimica et Cosmochimica Acta*, *75*(15), 4340-4350.

Tang, J., Köhler, S. J., & Dietzel, M. (2008a). Sr2+/Ca2+ and 44Ca/40Ca fractionation during inorganic calcite formation: I. Sr incorporation. *Geochimica et Cosmochimica Acta*, *72*(15), 3718-3732.

Tang, J., Dietzel, M., Böhm, F., Köhler, S. J., & Eisenhauer, A. (2008b). Sr2+/Ca2+ and 44Ca/40Ca fractionation during inorganic calcite formation: II. Ca isotopes. *Geochimica et Cosmochimica Acta*, *72*(15), 3733-3745.

Tang, J., Niedermayr, A., Köhler, S. J., Böhm, F., Kısakürek, B., Eisenhauer, A., & Dietzel, M. (2012). Sr2+/Ca2+ and 44Ca/40Ca fractionation during inorganic calcite formation: III. Impact of salinity/ionic strength. *Geochimica et cosmochimica acta*, *77*, 432-443.

Turchyn, A. V., & DePaolo, D. J. (2011). Calcium isotope evidence for suppression of carbonate dissolution in carbonate-bearing organic-rich sediments. *Geochimica et Cosmochimica Acta*, *75*(22), 7081-7098.

Wasylenki L. E., Dove P. M. and De Yoreo J. J. (2005b) Effects of temperature and transport conditions on calcite growth in the presence of Mg^{2+}: implications for paleothermometry. Geochim. Cosmochim. Acta 69, 4227–4236.

Watkins, J. M., Hunt, J. D., Ryerson, F. J., & DePaolo, D. J. (2014). The influence of temperature, pH, and growth rate on the δ 18 O composition of inorganically precipitated calcite. *Earth and Planetary Science Letters*, *404*, 332-343.

Watkins, J. M., DePaolo, D. J., & Watson, E. B. (2017). Kinetic fractionation of non-traditional stable isotopes by diffusion and crystal growth reactions. *Reviews in Mineralogy and Geochemistry*, *82*(1), 85-125.

Wefer G., Berger W. H. and Richter C. (1998) Proceedings of the Ocean Drilling Program, Initial Reports. Ocean Drilling Program, College Station, Tex.

Zhang, Y., & Dawe, R. A. (2000). Influence of Mg2+ on the kinetics of calcite precipitation and calcite crystal morphology. *Chemical Geology*, *163*(1-4), 129-138.

Zuddas, P., & Mucci, A. (1994). Kinetics of calcite precipitation from seawater: I. A classical chemical kinetics description for strong electrolyte solutions. *Geochimica et Cosmochimica Acta*, *58*(20), 4353-4362.

Zuddas, P., & Mucci, A. (1998). Kinetics of calcite precipitation from seawater: II. The influence of the ionic strength. *Geochimica et Cosmochimica Acta*, *62*(5), 757-766.

Zhu P, Macdougall JD (1998) Calcium isotopes in the marine environment and the oceanic calcium cycle. Geochim Cosmochim Acta 62:1691-1698

Conclusions

The three projects of this dissertation span great spatial and temporal scales, from global to laboratory, and correspondingly over millions to hundreds of years down to minutes and hours. Regardless of the scale of the particular study, however, the reactions occurring during carbonate growth and alteration occur at the molecular level, often taking much less than a fraction of a second to proceed. The fact that this scale serves as the fundamental "building block" of larger-scale systems allows isotopes and trace elements to be applied in addressing an enormous variety of scientific queries. In this dissertation, I have used these unique geochemical tools as well as the ubiquity of carbonate minerals in natural systems to study fundamentals of calcite growth, complexities of multi-mineral deposits, and global-scale carbon cycling. This work advances our understanding of controls on and effects of carbonate growth, furthering the field of geochemistry towards more accurate interpretation and engineering of natural systems.

Appendix A

Sample preparation and $\delta^{44/40}$Ca measurements with TIMS

These methods detail the preparation and measurement of fluid and solid samples for calcium isotope measurements ($\delta^{44/40}$Ca) via thermal ionization mass spectrometry (TIMS). All measurements of $\delta^{44/40}$Ca in this dissertation were carried out using a Thermo-Finnigan Triton Thermal Ionization Mass Spectrometer and all sample preparation was performed in the Center for Isotope Geochemistry research laboratories at the University of California, Berkeley. These procedures are specific for the materials analyzed in this dissertation.

A.1 Sample Preparation

Sample preparation was carried out in a Class 10,000 clean room while wearing proper personal protective equipment (PPE): long pants, clean room-specific clogs, lab coat, disposable nitrile gloves, hair net, and safety glasses. For beaker cleaning and acid preparation, sleeve caps, face shield, and plastic apron were worn.

Calcium from both solid and fluid samples was (1) separated from matrix elements and ions via column chemistry, (2) spiked, and (3) mounted on rhenium filaments for analyses. Details for solid and fluid samples are outlined below.

A.1.1 Solid sample digestion for carbonates

Solid digestion may be done in either nitric or acetic acid. Acetic is best to use for natural carbonates in multi-phase samples to avoid dissolution of any non-carbonate phases. Solids were weighed on an analytical balance then dissolved in either 1M acetic acid or 3M nitric acid with at least 1 mL acid for every 10 mg of solid. For multi-mineral samples, solids were then centrifuged, and the supernatant transferred via pipette to a clean, pre-weighed Teflon beaker. If digestion was performed in acetic acid, the supernatant was dried down in a fume hood then re-suspended in nitric acid.

A.1.2 Sample spiking procedure

An aliquot of acidified fluid sample (or digested solid) containing 30 µg of Ca was added to a clean, pre-weighed Teflon beaker. Following this addition, the new mass was recorded, then 10 µL of spike per µg Ca added, and then the final mass was recorded. The masses of sample and spike added were used during data reduction to precisely determine the Ca concentration in the sample. The spiked samples were capped and set on a hot plate at 110°C overnight, or alternatively, 500 µL 3M nitric acid was added and sample was set on hotplate for 1 hour. Following this step, samples in Teflon beakers were dried down with nitrogen gas in Teflon drying pots under heating lamps in a laminar flow hood.

A.1.3 Preparation of column resin

DGA resin (50-100µm) was prepared in a clean Teflon bottle. Approximately 1-3 g of dry resin was added to a few mL 3M nitric acid. The bottle was capped and agitated, then additional 3M nitric acid was added and the agitation step repeated. After most of the resin settled to the bottom of the vessel, the supernatant was removed via pipette and the nitric acid wetting steps repeated twice more. Following the nitric acid steps, the rinsing was performed with MilliQ deionized water (DI; 18 Ω). The resin was then stored in DI water. Wetted resin older than one month was discarded.

A.1.4 Column chemistry

In Teflon columns, DGA resin was added with DI water until the column was filled, leaving the upper reservoir free of resin. After all of resin settled within the column and bubbles were eliminated, two reservoirs of DI water were added, followed by one reservoir of 3M nitric acid. Dried samples were re-suspended in nitric acid, then loaded onto the column. The column with added sample was then washed with 3M nitric acid in additions of 200-400-800 µL. After these washing steps, effluent beakers were exchanged with sample collection beakers, and Ca was eluted via 400-400-700 µL additions of DI water. Samples were then dried down again with nitrogen gas in Teflon drying pots under heating lamps, then re-suspended in a few drops of concentrated nitric acid and 40% hydrogen peroxide to break down any organics. Samples were left overnight in the nitric-peroxide solution then dried down once more.

A.1.5 Sample loading

Dried samples were dissolved in 10 µL of 3M nitric acid. On the rhenium filament of each sample post, 3 µg of Ca (1 µL) was added via pipette, then the filament was slowly heated until the sample dried. After the sample dried, 0.7 µL of 40% phosphoric acid was added to the filament, then heated further and dried completely. Each sample post was inserted into the sample wheel, or turret, and partnered with a blank post. Each pair of posts was locked into place with a metal cover, and the turret was loaded into the mass spectrometer. Generally three or more standards (SRM 915A) were measured with every turret. Standards were spiked but did not undergo column chemistry.

A.2 Sample measurements

Once the sample wheel was inserted into the mass spectrometer following our laboratory protocol, current was added to the sample until a signal of >5V was attained on ^{40}Ca, with intermittent lens focusing steps. For each sample, intensities were measured for 100 cycles, divided into five blocks of 20 cycles each, with automated focusing and peak centering in between blocks. Data were reduced following a spike-subtraction method. Quality control checks were performed to rule out any instrument issues or poor functioning of sample posts and rhenium filaments. Unless otherwise specified, δ^{44}Ca values reported were averages of the block measurements, with the standard deviation given based on this grand mean. In nearly all cases, the standard deviation of the grand mean was larger than the average standard deviation for a given block, and therefore we take this as a conservative value of the standard deviation on a given measurement.

Appendix B:
Supplemental material for Chapter 2

B.1 Modeling methodology for interpretation of pore fluid Sr and Ca concentration data

B.1.1 Site Type I methodology

To derive the equation we use to estimate rates of AC formation for Type I sites, we start with the conservation equation. The change in pore fluid Ca at a given depth as a function of time reflects: (1) diffusion of dissolved pore fluid Ca in and out of that depth interval, (2) advection of fluid upward through the sediment column due to compaction, (3) any net precipitation or dissolution of calcite, (4) the addition of exchangeable Ca due to cation exchange during the equilibration of detrital clay minerals with surrounding pore fluids. In the following formulae, the net precipitation rate recorded from Ca pore fluid concentrations, R_{net}^{Ca}, is the difference between the rates of precipitation and dissolution (R_p - R_d).

The change in pore fluid Ca concentration ([Ca]) can be expressed as:

$$\frac{\partial [Ca]}{\partial t} = D_{Ca}\frac{\partial^2 [Ca]}{\partial z^2} - v\frac{\partial [Ca]}{\partial z} - R_{Net}^{Ca} \qquad \text{[B-1]}$$

We assume that this system is at steady-state, and so equation S-1 simplifies to:

$$R_{Net}^{Ca} = D_{Ca}\frac{\partial^2 [Ca]}{\partial z^2} - v\frac{\partial [Ca]}{\partial z} \qquad \text{[B-2]}$$

D_{Ca} is the diffusion coefficient for Ca^{2+} in marine sediments, accounting for seawater viscosity and sediment tortuosity (Yuan-Hui and Gregory, 1974; Sun and Turchyn, 2014), and v is the pore fluid velocity. Equation B-2 gives the net rate of AC formation per unit volume of sediment at a given depth at each site.

The spatial derivatives in the diffusion terms and advection terms are calculated according to Eq. B-3 and B-4, where M represents the concentration of Ca, and dz is the vertical distance between adjacent concentration data points. The concentration profile is fit with a smoothing spline so that depth-dependent terms for each site are calculated at identical depths in the sediment column.

$$\frac{\partial^2 M}{\partial z^2} = \frac{M(x+1)-2M(x)+M(x-1)}{\partial z^2} \qquad [S\text{-}3]$$

$$\frac{\partial M}{\partial z} = \frac{M(x+1)-M(x)}{\partial z} \qquad [S\text{-}4]$$

B.1.2 Site Type II methodology

At the Type II sites we assume that calcite dissolution rate and precipitation rate are almost equal ($R_p = R_d$), so a “recrystallization rate” R is defined as $R = R_p = R_d$. In such cases, Ca concentration cannot be used to calculate the recrystallization rate since the Ca concentration is affected by the net precipitation rate, which is close to zero in these cases. Trace elements or isotopes, however, are not necessarily in equilibrium between the pore fluid and the solid. Their concentrations can therefore provide information on the exchange rate of calcite dissolution and precipitation. In this section we use Sr concentrations to calculate recrystallization rates, a method used successfully by Fantle and DePaolo (2007). Sr is an ideal element to use to track recrystallization because incorporation into recrystallized carbonates is a main sink in the upper 200 m of marine sediments, and Sr is involved in no other reactions that would affect pore fluid [Sr] (Baker et al., 1982). The formation of celestite, a Sr-bearing sulfate mineral, was determined to have negligible effect on pore fluid [Sr] (Richter, 1996) in sediments with very high carbonate contents (~>85%). Although Mg can also be a useful tracer of recrystallization, the potential of pore fluid [Mg] to be affected by other reactions, including sorption and clay formation, makes it a less effective element to use in estimating rates of recrystallization (Baker et al., 1982).

Sr concentration in the fluid generally increases with depth in sea sediments due to its higher concentration in the solid phase than in seawater. As calcite dissolves, Sr is released from the solid phase to pore fluid in sediments, and this is balanced by the incorporation of Sr in the solid phase during calcite precipitation, diffusion and advection at steady state. The evolution of Sr concentration in the pore fluid (C_f) can be described by the equation:

$$\frac{\partial C_f}{\partial t} = D\frac{\partial^2 C_f}{\partial z^2} - v\frac{\partial C_f}{\partial z} + f_c RM\left(C_s - KC_f\right) \qquad [B\text{-}5]$$

where $M = \rho_s(1-\phi)/(\rho_f\phi)$, ρ is density (f referring to fluid and s referring to solid), K is the equilibrium distribution coefficient of Sr between the solid and the fluid, and f_c is the fraction of calcite in the solid. $z = 0$ is defined as the interface between sea water and the sediment, and z is positive in the downward direction.

We assume that porosity, fluid density, solid density, the distribution coefficient K, Sr concentration in the solid C_s, and R are all constants with depth. The value of M is close to 1.1. K is close to 20, and D is close to 7500 $\mathrm{m^2\ Myr^{-1}}$ (Fantle and DePaolo 2007). We further assume that the Sr concentration is at steady state, so the term $\frac{\partial \mathrm{C_f}}{\partial \mathrm{t}}$ is zero. The Sr concentration in pore fluid at the upper boundary is fixed at the modern seawater concentration (91 μM). Under these conditions, the solution for C_f is

$$C_f = \frac{C_s}{K} + \left(C_w - \frac{C_s}{K}\right) e^{-\frac{z}{L}} \qquad \text{[B-6]}$$

where $\mathrm{C_w = 91uM}$. The exponential factor is:

$$L^{-1} = \left(\frac{v^2}{4D^2} + \frac{f_c RMK}{D}\right)^{1/2} - \frac{v}{2D} \qquad \text{[B-7]}$$

For each site, the value of L can be obtained by fitting the Sr concentration profile with depth with two tunable parameters, L and $\mathrm{C_s/K}$. The best value for L is then used in calculating recrystallization rate of calcite based on the following equation:

$$R = \left(\frac{1}{L^2} + \frac{V}{LD}\right)\frac{D}{f_c MK} \qquad \text{[B-8]}$$

where $M = 1.1, K = 20,$ and $D = 7500\ \mathrm{m^2Myr^{-1}}$.

f_c is calculated using the average calcite fraction in the top 200 meters of the sediments. V is calculated using the average sedimentation rate for the sediments that are younger than 10 Myr. Compaction is not considered. Depth is fitted with age using a linear relationship. Although diffusivity varies considerably with temperature, Fantle and DePaolo (2006) pointed out that the change in tortuosity due to decreasing porosity with depth offsets the downhole temperature increase, and so we use a constant *D*.

Age data for Site 1092, 1238 and 1258 are not available. The sedimentation rates for these sites are estimated as follows: Site 1238 has an approximate rate of ~ 70m Myr^{-1}. Site 1258 has early Eocene sediments at the top so the sedimentation rate ~ 0. Site 1092 has a variable sedimentation rate, but averages about 15m Myr^{-1}. down to about 180m depth.

B.2 Tabulated results and model parameters

B.2.1 Type I Sites

Site	S	*Xcc*	ϕ	**AC Flux (net)**	**OC Flux**	**BC Flux**	**Total C Flux**	f_{AC}	f_{OC}	f_{BC}
M0027	1.46E-05	0.02	0.40	0	8.39E-03	5.00E-03	1.34E-02	0.000	0.627	0.373
M0059	2.58E-06	0.17	0.74	0	5.14E-03	3.00E-03	8.14E-03	0.000	0.631	0.369
381	8.39E-05	0.17	0.68	0	6.12E-02	1.25E-01	1.86E-01	0.000	0.329	0.671
688	1.35E-04	0.11	0.73	8.76E-04	2.37E-01	1.03E-01	3.41E-01	0.003	0.695	0.302
693	1.20E-05	0.02	0.58	4.57E-05	1.72E-03	2.95E-03	4.72E-03	0.010	0.364	0.626
725	1.13E-04	0.54	0.48	0	9.02E-02	8.48E-01	9.38E-01	0.000	0.096	0.904

819	5.00E-05	0.52	0.54	3.03E-04	1.96E-02	3.23E-01	3.43E-01	0.001	0.057	0.942
855	2.88E-04	0.06	0.67	0	9.83E-02	1.41E-01	2.39E-01	0.000	0.411	0.589
860	3.39E-05	0.02	0.51	0	2.11E-02	1.10E-02	3.21E-02	0.000	0.657	0.343
863	7.35E-04	0.01	0.46	0	3.52E-01	1.13E-01	4.65E-01	0.000	0.757	0.243
950	4.60E-05	0.58	0.72	2.62E-04	2.85E-02	2.00E-01	2.29E-01	0.001	0.125	0.874
951	3.51E-05	0.49	0.67	2.62E-04	2.11E-02	1.53E-01	1.74E-01	0.002	0.121	0.877
984	1.33E-04	0.16	0.73	1.28E-03	2.28E-02	1.49E-01	1.73E-01	0.007	0.132	0.861
999	3.40E-05	0.50	0.69	2.97E-04	3.05E-03	1.43E-01	1.46E-01	0.002	0.021	0.977
1033	7.00E-03	0.02	0.63	2.24E-03	7.49E+00	1.16E+00	8.66E+00	0.000	0.865	0.135
1034	1.10E-02	0.01	0.63	9.02E-04	1.38E+01	1.52E+00	1.53E+01	0.000	0.901	0.099
1082	8.56E-05	0.48	0.74	2.43E-03	2.57E-01	2.91E-01	5.50E-01	0.004	0.467	0.528
1084	1.67E-04	0.36	0.77	1.86E-03	7.30E-01	3.70E-01	1.10E+00	0.002	0.662	0.336
1119	1.50E-04	0.09	0.49	1.35E-03	5.85E-02	1.87E-01	2.47E-01	0.005	0.237	0.757
1232	4.75E-04	0.02	0.58	0	8.07E-02	8.60E-02	1.67E-01	0.000	0.484	0.516
1234	7.88E-04	0.40	0.61	1.40E-03	8.70E-01	3.33E+00	4.21E+00	0.000	0.207	0.793
1245	2.00E-04	0.10	0.58	1.48E-03	1.70E-01	2.38E-01	4.09E-01	0.004	0.416	0.581
1319	1.00E-03	0.15	0.66	1.82E-03	5.81E-01	1.39E+00	1.98E+00	0.001	0.294	0.705

Table B1: Calculated sedimentary carbon fractions (f_{OC} = fraction of organic carbon; f_{AC} = fraction of authigenic carbonate; f_{BC} = fraction of biogenic carbonate) and total carbon sedimentary fluxes in mol m^{-2} yr^{-1} based on an 80-m integration depth. S = sedimentation rate (m yr^{-1}), X_{cc} = fraction carbonate, and ϕ = porosity.

The selected sites also have the necessary data available: core recovery to at least 80 meters, pore fluid Ca, Sr, and SO_4 concentrations, age-depth information over the top 80 meters, mass fraction of $CaCO_3$, weight percent organic carbon, and porosity. Although sulfate concentrations are not needed for our model, these data are required to evaluate both the mechanism of AC formation, and the isotopic compositions of the authigenic precipitate. In sites where there are Sr isotope data there is evidence that AC formation persists at a slow rate throughout the section down to hundreds of meters depth (eg. Fantle and DePaolo, 2006).

B.2.2 Type II Sites

Site	L (m)	**S**	X_{cc}	**R**	**AC Flux**	**OC flux**	**BC flux**	**Total C flux**	f_{AC}	f_{OC}	f_{BC}
803	74.33	1.63E-05	0.89	8.04E-02	4.65E-02	1.98E-03	7.15E-02	1.20E-01	0.39	0.02	0.60
805	44.72	2.34E-05	0.91	2.13E-01	1.26E-01	1.58E-03	4.66E-02	1.74E-01	0.72	0.01	0.27
806	85.37	2.76E-05	0.91	6.75E-02	3.98E-02	3.92E-03	1.64E-01	2.08E-01	0.19	0.02	0.79
807	65.18	2.32E-05	0.92	1.05E-01	6.25E-02	1.88E-03	1.10E-01	1.74E-01	0.36	0.01	0.63
998	67.99	1.54E-05	0.72	1.17E-01	5.45E-02	1.04E-04	3.50E-02	8.96E-02	0.61	0.00	0.39

1088	115.70	1.28E-05	0.91	3.35E-02	1.98E-02	8.62E-04	7.46E-02	9.52E-02	0.21	0.01	0.78
1092	226.03	1.50E-05	0.80	1.21E-02	6.28E-03	1.62E-03	9.11E-02	9.90E-02	0.06	0.02	0.92
1120	125.04	7.95E-06	0.95	2.61E-02	1.60E-02	9.65E-04	4.49E-02	6.19E-02	0.26	0.02	0.73
1169	182.61	1.42E-05	0.85	1.62E-02	8.92E-03	3.17E-03	8.89E-02	1.01E-01	0.09	0.03	0.88
1194	84.72	1.06E-05	0.79	6.72E-02	3.44E-02	2.57E-03	3.33E-02	7.03E-02	0.49	0.04	0.47

Table B2. S = sedimentation rate (m yr^{-1}); R = recrystallization rate (Myr^{-1}); Fluxes given in mol m^{-2} yr^{-1}.

The calculated diffusive-reaction length, sedimentation rate, calcite fraction, and recrystallization rate for each site are listed in Table B-2. The values of recrystallization rates are mostly between 0 to 0.2 My^{-1}. The fitting of Sr concentration for all sites are plotted in Figure S-1.

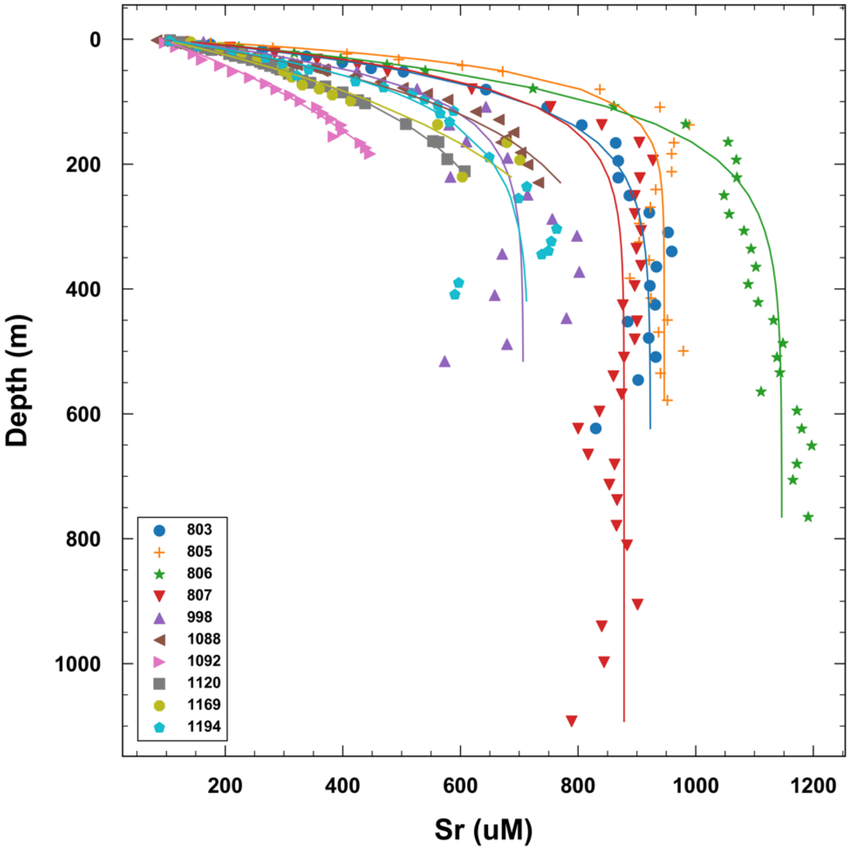

Figure B1: Model fits to pore fluid concentrations in Type II sites.

B.3 Limitations and uncertainty in the model

The net rates of AC formation estimated for Type I sites fluctuate to both positive and negative values with depth for most sites, reflecting the measured pore fluid trends in dissolved Ca. For some sites, this results in an integrated negative AC flux. A negative AC flux means that there is net dissolution of biogenic carbonate. For sites where the calculated AC flux is negative we set the value at zero. The authigenic fraction is such a small percentage relative to the contribution from biogenic carbonate for these mixed-mineralogy sites that this correction does not change the conclusions.

We also assume that all changes in porewater Ca concentration are due to carbonate dissolution and precipitation, but other reactions could affect the Ca concentration, such as alteration of detrital materials in the core, including volcanic material, alteration of seafloor basalt that underlies the sediment, and sorption-desorption reactions in response to re-equilibration of clay surface sites to pore fluid chemistry of sediments. In addition, carbonate fluorapatite (CFA) was shown by Reimers et al. (1996) to precede authigenic calcite formation and dominate authigenic phases in the upper few centimeters. This phase contains Ca, which means our estimates of net AC precipitation rates close to the sediment-water interface may be larger due to Ca drawdown from CFA precipitation.

Given that we are looking only at the top 80 meters of sediments, the effect of alteration reactions in basalt, which is generally hundreds of meter below the sediment-water interface, are expected to negligible. Dissolution of silicate materials within the section, however, may be significant. As shown by Maher et al. (2006) for Site 984, increases in pore fluid Ca at depths below the Ca minimum, could be due to dissolution of plagioclase. The Maher et al. study concluded that the net precipitation of calcite and consequently the removal of Ca from pore fluids is the dominant mechanism responsible for dissolution of Ca-bearing silicates. However, silicate dissolution rates are generally low and are unlikely to significantly affect the calculated rates of AC formation.

Sorption-desorption reactions could affect the pore fluid Ca budget because clays trade exchangeable Ca ions for Na, potentially resulting in the net addition of Ca to pore waters (Sayles and Mangelsdorf, 1977). Furthermore, as ammonium (NH_4^+) is liberated from oxidized organic matter, ammonium ions can displace Ca from exchangeable clay sites. The exchange reactions that release Ca into pore waters could cause elevation of pore fluid Ca concentrations and hence could lead us to underestimate the rate of removal of Ca and the rate of AC formation. Furthermore, the addition of carbonate alkalinity from organic matter remineralization plus the release of Ca into solution serves to increase the saturation index of pore waters with respect to carbonate minerals more so than the addition of carbonate alkalinity alone.

To account for this buffering effect from cation exchange, we incorporated into our model ion-exchange reactions that release Ca ions into solution based on pore fluid concentrations of Ca^{2+}, Mg^{2+}, Na^+, K^+, and NH_4^+. The exchange reactions are outlined in detail in B.4. When these equations are included, the result is a change in depth-dependent rates of AC formation of less than 1%, which is negligible.

Dolomite is found in many of the sites (e.g., Wefer et al. 1998), and in some cases is thought to be authigenic in origin, although it has only been observed in significant quantities at depths below ~100 mbsf. In our formulations, we assume that the AC precipitate is $CaCO_3$. Dolomite may precipitate according to either of the following reactions:

$$Ca^{2+} + Mg^{2+} + 2CO_3^{2-} \rightarrow CaMg(CO_3)_2 \qquad [B-8]$$

$$Mg^{2+} + 2CaCO_3(s) \rightarrow CaMg(CO_3)_2\,(s) + Ca^{2+} \qquad [B-9]$$

The precipitation of dolomite from pore fluids by Eq. S-8 removes twice as much carbon per Ca removed. Hence to the extent that dolomite is an important fraction of AC in Category II sections, and Eq. B-8 applies, our modeling would underestimate the flux of AC carbon. As noted, dolomite does not appear to be the dominant authigenic phase in most marine sediment sections, but to the extent it is, the AC formation rate we calculate may need to be increased. The likely magnitude of this correction might increase the AC formation rate as much as a factor of two.

B.4 Considering effects of cation exchange between detrital clay and pore waters

Each of the exchange reactions (Eq. B-10 to B-13) can be written following the law of mass action such as to determine an exchange constant, K, relating the ratio of activities of the products to reactants at equilibrium.

$$0.5Ca^{2+} + Na \cdot Clay = Na^{+} + 0.5Ca \cdot Clay \qquad [B-10]$$

$$0.5Mg^{2+} + Na \cdot Clay = Na^{+} + 0.5Mg \cdot Clay \qquad [B-11]$$

$$K^{+} + Na \cdot Clay = Na^{+} + K \cdot Clay \qquad [B-12]$$

$$NH_4^{+} + Na \cdot Clay = Na^{+} + NH_4 \cdot Clay \qquad [B-13]$$

For example, Eq. B-10 can be rewritten:

$$\frac{\gamma_{Na} c_{Na} (cCa{\cdot}Clay)^{0.5}}{(\gamma_{Ca} c_{Ca})^{0.5}\, cNa{\cdot}Clay} = K^{Ca/Na} \qquad [B-14]$$

Where γ_i is the activity coefficient of species *i*, c_i is the concentration of species *i* in units of mol/L, and *c•Xclay* is the concentration of the sorbed species *X*. We assume ideality for the behavior of the sorbed species such that their corresponding activity coefficients are set to one. Exchange constants for each of the above equations (Table B3) were determined based on exchange studies performed by Sayles and Mangelsdorf (1977) and Von Breymann and Suess (1988), who equilibrated natural clays and marine sediments with modern seawater to determine the concentration of all sorbed and aqueous species. Our model solves for changes in concentrations of sorbed Ca at every depth point based on pore fluid concentrations of Ca, Mg, Na, K, and NH_4 and the experimentally determined exchange constants, assuming a constant cation exchange capacity (CEC) of the non-carbonate solid fraction equal to 0.25 eq/kg, which is a reasonable average value suggested by Sayles and Mangelsdorf (1977). The addition or removal of Ca along the sediment column (*dCa/dz*) is included as another term in Eq S-2.

Exchange Constant	Value
$K^{Ca/Na}$	5.6
$K^{Mg/Na}$	3.6
$K^{K/Na}$	4.9
$K^{NH4/Na}$	2.8

Table B3. Exchange constants for exchange reactions given by Eq. B-10 to B-13.

B.5 Site Locations and links

Link to IODP online data repository: http://iodp.tamu.edu/janusweb/links/links_all.shtml
Interactive ODP Site Map: https://iodp.tamu.edu/scienceops/maps/odpmap_int/

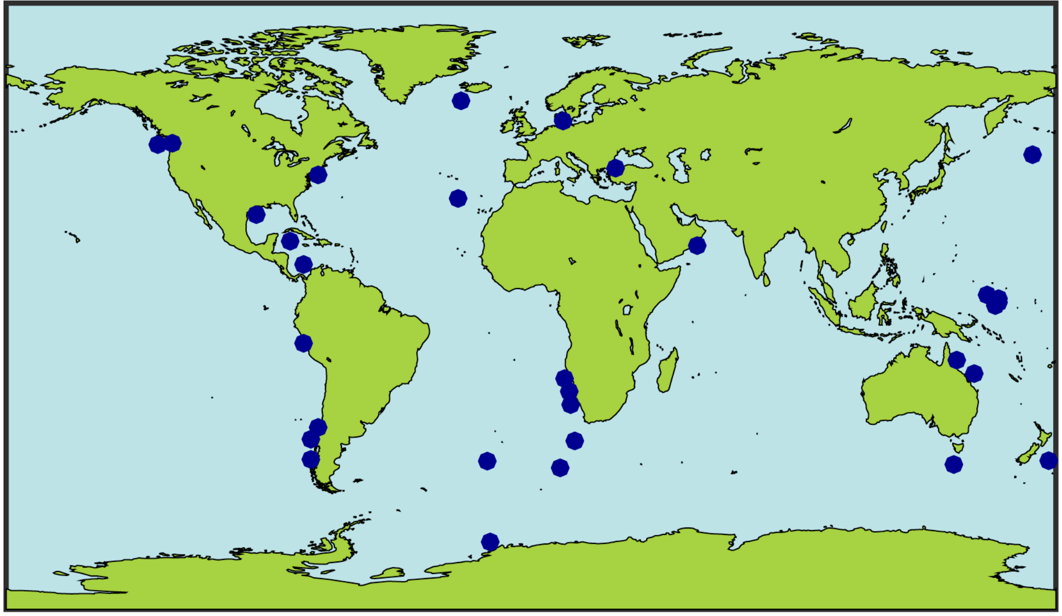

Figure B2. Map of site distribution.

Site	Location
803	2°25.98'N, 160°32.40'E
805	1°13.68'N, 160°31.76'E
806	0°19.11'N, 159°21.68'E
807	3°36.42'N, 156°37.49'E
998	19°29.377'N, 82°56.166'W

1085	29°22.4665´S, 13°59.4064´E
1088	~40°S, 15°E
1092	~48S, 10E
1120	~45S, 180E
1169	47°3.9159′S 145°14.2089′E
1194	~20 S, 152 E
M0027	39°38.046067’N 73°37.301460’W
M0059	55°0.295′N 10°6.491′E
381	41°40.25'N, 29°24.96'E
688	11°32.26'S, 78°56.57'W
693	70°49.888'S, 14°34.461'W
725	18°29.200'N, 57°42.030'E
819	16°37.439'S, 146°19.486'E
855	48°26.563'N, 128°38.271'W
860	45°51.972'S, 75°45.101'W
863	46°14.210'S, 15°46.311W
950	31°9.011'N, 25°36.004'W
951	32°1.896'N, 24°52.232'W
984	61°25.507'N, 24°04.939'W
999	12°44.639'N, 78°44.360'W
1033	48°35.437′N, 123°30.205′W
1034	48°38.000′N, 123°30.000′W
1082	21°5.6373′S, 11°49.2361′E
1084	25°30.8345′S, 13°1.6668′E
1119	~45 N, 172 E
1232	39°53.45´, 75°54.08´W
1234	36°13.153´S, 73°40.902´W
1245	~125 W, 44.6 N
1319	27°15.9751′N, 94°24.1908′W

Table B4. Site locations.

B.6 IODP/ODP/DSDP site references

Site Number	Reference	DOI (where available)
803	Kroenke, L. W., Berger, W. H., Janecek, T. R., et al., 1991 Proceedings of the Ocean Drilling Program, Initial Reports, Vol. 130	doi:10.2973/odp.proc.ir.130.105.1991
805	Kroenke, L. W., Berger, W. H., Janecek, T. R., et al., 1991 Proceedings of the Ocean Drilling Program, Initial Reports, Vol. 130	doi:10.2973/odp.proc.ir.130.107.1991

806	Kroenke, L. W., Berger, W. H., Janecek, T. R., et al., 1991 Proceedings of the Ocean Drilling Program, Initial Reports, Vol. 130	doi:10.2973/odp.proc.ir.130.108.1991
807	Kroenke, L. W., Berger, W. H., Janecek, T. R., et al., 1991 Proceedings of the Ocean Drilling Program, Initial Reports, Vol. 130	doi:10.2973/odp.proc.ir.130.109.1991
998	Sigurdsson, H., Leckie, R.M., Acton, G.D., et al., 1997 Proceedings of the Ocean Drilling Program, Initial Reports, Vol. 165	doi:10.2973/odp.proc.ir.165.103.1997
1088	Shipboard Scientific Party, 1999. Site 1088. *In* Gersonde, R., Hodell, D.A., Blum, P., et al., *Proc. ODP, Init. Repts.,* 177: College Station, TX (Ocean Drilling Program), 1–66.	doi:10.2973/odp.proc.ir.177.103.1999
1092	Shipboard Scientific Party, 1999. Site 1092. *In* Gersonde, R., Hodell, D.A., Blum, P., et al., *Proc. ODP, Init. Repts.,* 177: College Station, TX (Ocean Drilling Program), 1–82.	doi:10.2973/odp.proc.ir.177.107.1999
1120	Carter, R.M., McCave, I.N., Richter, C., Carter, L., et al., 1999 Proceedings of the Ocean Drilling Program, Initial Reports Volume 181	doi:10.2973/odp.proc.ir.181.104.2000
1169	Exon, N.F., Kennett, J.P., Malone, M.J., et al., 2001 Proceedings of the Ocean Drilling Program, Initial Reports Volume 189	NA
1194	Isern, A.R., Anselmetti, F.S., Blum, P., et al., 2002 Proceedings of the Ocean Drilling Program, Initial Reports Volume 194	NA
M0027	Expedition 313 Scientists, 2010. New Jersey Shallow Shelf: shallow-water drilling of the New Jersey continental shelf: global sea level and architecture of passive margin sediments. IODP Prel. Rept., 313.	doi:10.2204/iodp.pr.313.2010
M0059	Expedition 347 Scientists, 2014. Baltic Sea Basin Paleoenvironment: paleoenvironmental evolution of the Baltic Sea Basin through the last glacial cycle. *IODP Prel. Rept.,* 347	doi:10.2204/iodp.pr.347.2014
381	Ross, D. A., Neprochnov, Y. P., et al., 1978. Initial Reports of the Deep Sea Drilling Project, Volume 42, Part 2: Washington (U.S. Government Printing Office).	doi:10.2973/dsdp.proc.42-2.105.1978
688	Shipboard Scientific Party, 1988. Site 688. *In* Suess, E., von Huene, R., et al., *Proc. ODP, Init. Repts.,* 112:	doi:10.2973/odp.proc.ir.112.119.198

	College Station, TX (Ocean Drilling Program), 873–1004	8
693	Barker, P. E, Kennett, J. P., et al., 1988. Proc. ODP, Init. Repts. 113: College Station, TX (Ocean Drilling Program).	doi:10.2973/odp.proc.ir.113.109.1988
725	Prell, W. L., Niitsuma, N., et al., 1989. Proc. ODP, Init. Repts., 117: College Station, TX (Ocean Drilling Program).	doi:10.2973/odp.proc.ir.117.112.1989
819	Shipboard Scientific Party, 1991. Site 819. *In* Davies, P.J., McKenzie, J.A., Palmer-Julson, A., et al., *Proc. ODP, Init. Repts.,* 133: College Station, TX (Ocean Drilling Program), 451–508	doi:10.2973/odp.proc.ir.133.112.1991
855	Shipboard Scientific Party, 1992. Site 855. *In* Davis, E.E., Mottl, M.J., Fisher, A.T., et al., *Proc. ODP, Init. Repts.,* 139: College Station, TX (Ocean Drilling Program), 101–160.	doi:10.2973/odp.proc.ir.139.105.1992
860	Behrmann, J.H., Lewis, S.D., Musgrave, R.J., et al., 1992 Proceedings of the Ocean Drilling Program, Initial Reports, no. 141	doi:10.2973/odp.proc.ir.141.107.1992
863	Behrmann, J.H., Lewis, S.D., Musgrave, R.J., et al., 1992 Proceedings of the Ocean Drilling Program, Initial Reports,No. 141	doi:10.2973/odp.proc.ir.141.110.1992
950	Shipboard Scientific Party, 1995. Site 950. *In* Schmincke, H.-U., Weaver, P.P.E., Firth, J.V., et al., *Proc. ODP, Init. Repts.,* 157: College Station, TX (Ocean Drilling Program), 51–104.	doi:10.2973/odp.proc.ir.157.104.1995
951	Shipboard Scientific Party, 1995. Site 951. *In* Schmincke, H.-U., Weaver, P.P.E., Firth, J.V., et al., *Proc. ODP, Init. Repts.,* 157: College Station, TX (Ocean Drilling Program), 105–134.	doi:10.2973/odp.proc.ir.157.105.1995
984	Jansen, E., Raymo, M.E., Blum, P., et al., 1996 Proceedings of the Ocean Drilling Program, Initial Reports, Vol. 162	doi:10.2973/odp.proc.ir.162.106.1996
999	Sigurdsson, H., Leckie, R.M., Acton, G.D., et al., 1997 Proceedings of the Ocean Drilling Program, Initial Reports, Vol. 165	doi:10.2973/odp.proc.ir.165.104.1997
1033	Shipboard Scientific Party, 1998. Sites 1033 and 1034. *In* Bornhold, B., Firth, J.V., et al., *Proc. ODP, Init. Repts.,* 169S: College Station, TX (Ocean Drilling Program), 11–61	doi:10.2973/odp.proc.ir.169s.102.1998
1034	Shipboard Scientific Party, 1998. Sites 1033 and 1034. *In* Bornhold, B., Firth, J.V., et al., *Proc. ODP, Init. Repts.,* 169S: College Station, TX (Ocean Drilling Program), 11–61	doi:10.2973/odp.proc.ir.169s.102.1998

1082	Wefer, G., Berger, W.H., Richter, C., et al., 1998. *Proc. ODP, Init. Repts.,* 175: College Station, TX (Ocean Drilling Program)	doi:10.2973/odp.proc.ir.175.1998
1084	Wefer, G., Berger, W.H., Richter, C., et al., 1998. *Proc. ODP, Init. Repts.,* 175: College Station, TX (Ocean Drilling Program)	doi:10.2973/odp.proc.ir.175.1998
1119	Carter, R.M., McCave, I.N., Richter, C., Carter, L., et al., 1999 Proceedings of the Ocean Drilling Program, Initial Reports Volume 181	doi:10.2973/odp.proc.ir.181.103.2000
1232	Shipboard Scientific Party, 2003. Site 1232. *In* Mix, A.C., Tiedemann, R., Blum, P., et al., *Proc. ODP, Init. Repts.,* 202: College Station, TX (Ocean Drilling Program), 1–54.	doi:10.2973/odp.proc.ir.202.103.2003
1234	Shipboard Scientific Party, 2003. Site 1234. *In* Mix, A.C., Tiedemann, R., Blum, P., et al., *Proc. ODP, Init. Repts.,* 202: College Station, TX (Ocean Drilling Program), 1–64.	doi:10.2973/odp.proc.ir.202.105.2003
1245	Shipboard Scientific Party, 2003. Site 1245. *In* Tréhu, A.M, Bohrmann, G., Rack, F.R., Torres, M.E., et al., *Proc. ODP, Init. Repts.,* 204: College Station, TX (Ocean Drilling Program), 1–131.	doi:10.2973/odp.proc.ir.204.104.2003
U1319	Expedition 308 Scientists, 2005. Overpressure and fluid flow processes in the deepwater Gulf of Mexico: slope stability, seeps, and shallow-water flow. *IODP Prel. Rept.,* 308.	doi:10:2204/iodp.pr.308.2005

Table B5. Site references

Supplemental Reference List

1. Baker, P. A., Gieskes, J. M. and Elderfield, H., 1982. Diagenesis of Carbonates in Deep-Sea Sediments--Evidence From SR/CA Ratios and Interstitial Dissolved SR2+ Data. *Journal of Sedimentary Research*, *52*(1).
2. Holland, H.D., 1978. *The Chemistry of the Atmospheres and Oceans*, New York: Wiley, c1978.
3. Horita, J., Zimmermann, H. and Holland, H.D., 2002. Chemical evolution of seawater during the Phanerozoic: Implications from the record of marine evaporites. *Geochimica et Cosmochimica Acta*, *66*(21), pp.3733-3756.
4. Maher, K., Steefel, C.I., DePaolo, D.J. and Viani, B.E., 2006. The mineral dissolution rate conundrum: Insights from reactive transport modeling of U isotopes and pore fluid chemistry in marine sediments. *Geochimica et Cosmochimica Acta, 70*(2), pp.337-363.

5. Reimers, C.E., Ruttenberg, K.C., Canfield, D.E., Christiansen, M.B. and Martin, J.B., 1996. Porewater pH and authigenic phases formed in the uppermost sediments of the Santa Barbara Basin. *Geochimica et Cosmochimica Acta, 60*(21), pp.4037-4057.
6. Richter, F.M., 1996. Models for the coupled Sr-sulfate budget in deep-sea carbonates. *Earth Planetary Science Letters, 141*(1–4), pp.199–211.
7. Sayles, F.L. and Mangelsdorf, P.C., 1977. The equilibration of clay minerals with sea water: exchange reactions. *Geochimica et Cosmochimica Acta, 41*(7), 951-960.
8. Von Breymann, M.T. and Suess, E., 1988. Magnesium in the marine sedimentary environment: Mg- NH4 ion exchange. *Chemical geology*, *70*(4), pp.359-371.
9. Yuan-Hui, L. and Gregory, S., 1974. Diffusion of ions in sea water and in deep-sea sediments. *Geochimica et cosmochimica acta*, *38*(5), pp.703-714.